

MEASURING THE SCATTER IN THE CLUSTER OPTICAL RICHNESS-MASS
RELATION WITH MACHINE LEARNING

A Dissertation

by

STEVEN ALVARO BOADA

Submitted to the Office of Graduate and Professional Studies of
Texas A&M University
in partial fulfillment of the requirements for the degree of

DOCTOR OF PHILOSOPHY

Chair of Committee, Casey J. Papovich
Committee Members, Wolfgang Bangerth
 Louis Strigari
 Nicholas Suntzeff
Head of Department, Lewis Ford

August 2016

Major Subject: Physics and Astronomy

Copyright 2016 Steven Alvaro Boada

ABSTRACT

The distribution of massive clusters of galaxies depends strongly on the total cosmic mass density, the mass variance, and the dark energy equation of state. As such, measures of galaxy clusters can provide constraints on these parameters and even test models of gravity, but only if observations of clusters can lead to accurate estimates of their total masses. Here, we carry out a study to investigate the ability of a blind spectroscopic survey to recover accurate galaxy cluster masses through their line-of-sight velocity dispersions (LOSVD) using probability based and machine learning methods. We focus on the Hobby Eberly Telescope Dark Energy Experiment (HETDEX), which will employ new Visible Integral-Field Replicable Unit Spectrographs (VIRUS), over 420 degree² on the sky with a 1/4.5 fill factor. VIRUS covers the blue/optical portion of the spectrum (3500 – 5500 Å), allowing surveys to measure redshifts for a large sample of galaxies out to $z < 0.5$ based on their absorption or emission (e.g., [O II], Mg II, Ne V) features. We use a detailed mock galaxy catalog from a semi-analytic model to simulate surveys observed with VIRUS, including: (1) Survey, a blind, HETDEX-like survey with an incomplete but uniform spectroscopic selection function; and (2) Targeted, a survey which targets clusters directly, obtaining spectra of all galaxies in a VIRUS-sized field. For both surveys, we include realistic uncertainties from galaxy magnitude and line-flux limits. We benchmark both surveys against spectroscopic observations with “perfect” knowledge of galaxy line-of-sight velocities. With Survey observations, we can recover cluster masses to ~ 0.1 dex which can be further improved to < 0.1 dex with Targeted observations. This level of cluster mass recovery provides important measurements of the intrinsic scatter in the optical richness-cluster mass relation, and enables constraints on the

key cosmological parameter, σ_8 , to to $< 20\%$.

As a demonstration of the methods developed previously, we present a pilot survey with integral field spectroscopy of ten galaxy clusters optically selected from the Sloan Digital Sky Survey’s DR8 at $z = 0.2 - 0.3$. Eight of the clusters are rich ($\lambda > 60$) systems with total inferred masses $(1.58 - 17.37) \times 10^{14} M_{\odot}$ (M_{200c}), and two are poor ($\lambda < 15$) systems with inferred total masses $\sim 0.5 \times 10^{14} M_{\odot}$ (M_{200c}). We use the Mitchell Spectrograph, (formerly the VIRUS-P spectrograph, a prototype of the HETDEX VIRUS instrument) located on the McDonald Observatory 2.7m telescope, to measure spectroscopic redshifts and line-of-sight velocities of the galaxies in and around each cluster, determine cluster membership and derive LOSVDs. We test both a LOSVD-cluster mass scaling relation and a machine learning based approach to infer total cluster mass. After comparing the cluster mass estimates to the literature, we use these independent cluster mass measurements to estimate the absolute cluster mass scale, and intrinsic scatter in the optical richness-mass relationship. We measure the intrinsic scatter in richness at fixed cluster mass to be $\sigma_{M|\lambda} = 0.27 \pm 0.07$ dex in excellent agreement with previous estimates of $\sigma_{M|\lambda} \sim 0.2 - 0.3$ dex. We discuss the importance of the data used to train the machine learning methods and suggest various strategies to import the accuracy of the bias (offset) and scatter in the optical richness-cluster mass relation. This demonstrates the power of blind spectroscopic surveys such as HETDEX to provide robust cluster mass estimates which can aid in the the determination of cosmological parameters and help to calibrate the observable-mass relation for future photometric large area-sky surveys.

TABLE OF CONTENTS

	Page
ABSTRACT	ii
TABLE OF CONTENTS	iv
LIST OF FIGURES	vi
LIST OF TABLES	viii
1. INTRODUCTION	1
1.1 Galaxy Clusters	1
1.2 Observations of Galaxy Clusters	4
1.2.1 X-ray	4
1.2.2 Optical	5
1.2.3 The Sunyaev-Zel'dovich Effect	7
1.3 Cluster Formation: Relationship to Cosmological Parameters	8
1.4 Cosmology with Galaxy Clusters	9
1.5 Galaxy Cluster Surveys as a Data Science Challenge	11
1.5.1 Machine Learning	12
1.6 This Work	14
2. SIMULATED PERFORMANCE, MASS RECOVERY, AND LIMITS TO COSMOLOGY	18
2.1 Introduction	18
2.2 Data and Mock Observations	23
2.2.1 The Buzzard Mock Catalogs	23
2.2.2 Conditional [O II] Flux Probability Distribution Functions . .	24
2.2.3 HETDEX	25
2.2.4 Mock Observations	27
2.3 Recovery of Parameters	28
2.3.1 Cluster Redshift	28
2.3.2 Line-of-Sight Velocity Dispersion	29
2.3.3 Estimates of Cluster Mass	30
2.4 Results	35
2.4.1 Recovery of Cluster Members	36
2.4.2 Mass estimates	38

2.4.3	Impact of Training Sample Cosmology	48
2.5	HETDEX as a Galaxy Cluster Survey at $z < 0.5$	52
2.5.1	Constraints on Cosmological Parameters	52
2.5.2	Scale and Scatter of the Richness-Cluster Mass Relation	54
3.	A PILOT SURVEY TO MEASURE CLUSTER DYNAMICS: TARGETED OBSERVATIONS WITH THE VIRUS PROTOTYPE INSTRUMENT	61
3.1	Introduction	61
3.2	Design	64
3.2.1	Target Selection	64
3.2.2	Observations	66
3.3	Data Reduction	68
3.4	Analysis	71
3.4.1	Redshift Catalog	72
3.4.2	Cluster Membership	78
3.4.3	Line-of-Sight Velocity Dispersion	80
3.5	Estimating Cluster Masses	81
3.5.1	PL Estimates of Cluster Mass	81
3.5.2	Supervised Machine Learning	82
3.5.3	ML Based Observations	83
3.5.4	ML Based Cluster Masses	85
3.5.5	The Importance of Training Features	86
3.6	Results and Discussion	89
3.6.1	Cluster Masses	89
3.6.2	Notes for Individual Clusters	94
3.6.3	On the Accuracy of ML based Cluster masses	97
3.6.4	Optical Richness-Mass Relation	98
3.6.5	Calibration of the Richness-Mass Relation	101
4.	SUMMARY AND FUTURE WORK	103
4.1	Summary	103
4.2	Other Potential Investigations	107
4.2.1	Investigation of Cluster Miscentering	107
4.2.2	The Search for Clusters above $z \sim 1$	108
4.2.3	Outstanding Questions	109
	REFERENCES	111
	APPENDIX A. MS OBSERVATIONS	118

LIST OF FIGURES

FIGURE	Page
1.1 Hubble Space Telescope image of galaxy cluster Abell 1689.	3
1.2 The relation between the mean Richness and the mean cluster mass. .	6
1.3 The Sunyaev-Zel'dovich Effect.	8
1.4 An example of a classification tree.	13
2.1 Illustration of the probability based [O II] flux prediction method. .	22
2.2 HETDEX pointing strategy.	26
2.3 Illustration of the probability based cluster mass prediction method. .	33
2.4 Recovery fractions for the Targeted and Survey observations.	36
2.5 Probability based cluster mass predictions.	39
2.6 ML based cluster mass predictions	41
2.7 ML based cluster mass predictions in the Millennium Simulation . .	51
2.8 Optical richness versus corrected cluster mass	59
3.1 Basic properties of the ten galaxy clusters targeted with the MS. . . .	67
3.2 SDSS <i>r</i> image of cluster MSJ133520.1+410004.1 and spectra quality examples	70
3.3 Redshift recovery fractions across all clusters	73
3.4 Quality flag assignments for the 2.7 million Buzzard catalog galaxies .	85
3.5 Corner plot of the <i>training</i> data with features σ and z	87
3.6 PL estimated cluster versus ML predicted cluster mass	90
3.7 Richness versus total cluster mass for the clusters in our sample . .	99

A.1 Montage of remaining nine clusters	119
--	-----

LIST OF TABLES

TABLE	Page
2.1 Mean bias for different bins of predicted cluster mass.	43
2.2 Mean scatter in cluster mass after bias correction for different bins of predicted cluster mass.	46
3.1 Basic properties of the ten galaxy clusters targeted with the MS.	65
3.2 Spectroscopic redshifts for galaxies in MSJ133520.1+410004.1	75
3.3 Summary of derived cluster parameters.	93
A.1 Spectroscopic redshifts for galaxies in MSJ010455.4+000336.3	120
A.2 Spectroscopic redshifts for galaxies in MSJ153656.3+242431.6	121
A.3 Spectroscopic redshifts for galaxies in MSJ164019.8+464241.5	123
A.4 Spectroscopic redshifts for galaxies in MSJ140102.0+025242.6	125
A.5 Spectroscopic redshifts for galaxies in MSJ172227.2+320757.2	127
A.6 Spectroscopic redshifts for galaxies in MSJ211849.1+003337.3	129
A.7 Spectroscopic redshifts for galaxies in MSJ215422.9+003723.5	131
A.8 Spectroscopic redshifts for galaxies in XMMXCSJ124425.9+164758.0.	132
A.9 Spectroscopic redshifts for galaxies in XMMXCSJ125650+254803.2.	133

1. INTRODUCTION

This thesis focuses on how we may use upcoming large-area sky surveys to better understand galaxy clusters in a cosmological context. It covers a broad range of topics from galaxy clusters, to planning and observing, cosmology, probability and statistics, numerical simulations, data reduction, and machine learning. As such, the work presented here stands at the emerging intersection of astronomy and data science.

To begin, we introduce many of the basic concepts needed to understand the relevance of this thesis. While this overview is certainly not comprehensive, it should provide the basic knowledge to follow the remaining discussion. The following two chapters constitute the bulk of our analysis, and can be thought of as a theoretical study and a practical test of the theory. We conclude with a look to the future and how this thesis might be extended to other pressing issues in astronomy today.

But first, we begin by discussing what clusters of galaxies are, how they are deeply related to the cosmological parameters of the Universe, and how we go about studying them. We provide a brief introduction, through example, to some of the key concepts of machine learning, and conclude with a discussion of the importance of this work to set the stage for this thesis.

1.1 Galaxy Clusters

Clusters of galaxies are large gravitationally bound, highly over-dense, systems of galaxies. A collection of galaxies (now known to be the Virgo Cluster) was first documented by Charles Messier in 1781 after entry 91 in his catalog. The place of galaxy clusters in the canon was solidified when Edwin Hubble proved their constituent nebulae were not bound to the Milky Way ([Hubble, 1926](#)), but were

collections of stars similar to the Milky Way. Work to understand their nature and origin began in earnest when [Hubble & Humason \(1931\)](#) used the virial theorem and the galaxy velocities in the centers of the Virgo ([Smith, 1936](#)) and Coma ([Zwicky, 1933](#)) clusters to derive their masses. Fritz Zwicky measured the average velocity of the Coma Cluster galaxies to be 977 km s^{-1} , leading to a virial mass estimate of $3.3 \times 10^{15} \text{ M}_\odot$. After comparing this mass estimate to the total luminosity from the cluster member galaxies, he found a mass-to-light ratio of approximately 660:1. This led Zwicky to theorize the existence of large amounts of non-luminous matter and coin the term “dark matter” (DM), which we still use today.

Some controversy surrounds what exactly constitutes a “galaxy cluster,” as small associations of galaxies are often referred to as “groups”. [Abell \(1958\)](#) define a “richness” parameter as the number of cluster member galaxies with brightnesses between the magnitude of the third brightest member, m_3 , and $m_3 + 2$. Galaxy associations with a richness of 30 or more are routinely referred to as rich clusters and those structures with richness between three and 30 are classified as poor groups. Because this definition is far from universal, we will not make a distinction in this thesis, any bound system of galaxies we refer to as a cluster, and we will use the richness as a parameter that correlates with total cluster mass.

Modern astronomy catalogues the composition of galaxy clusters in three main parts. In optical and near-infrared wavelengths, the galaxies themselves comprise the most obvious feature, and contain a large portion (but not the entirety) of the luminous matter (stars) in the cluster. The stellar mass associated with the galaxies contributes only a small fraction of the total baryonic matter content. Furthermore, the fraction of baryons located in stars decreases significantly with increasing cluster mass ([Gonzalez et al., 2007](#)). For rich clusters, the vast majority of the baryons reside in a low-density, hot gas between the cluster galaxies known as the intracluster

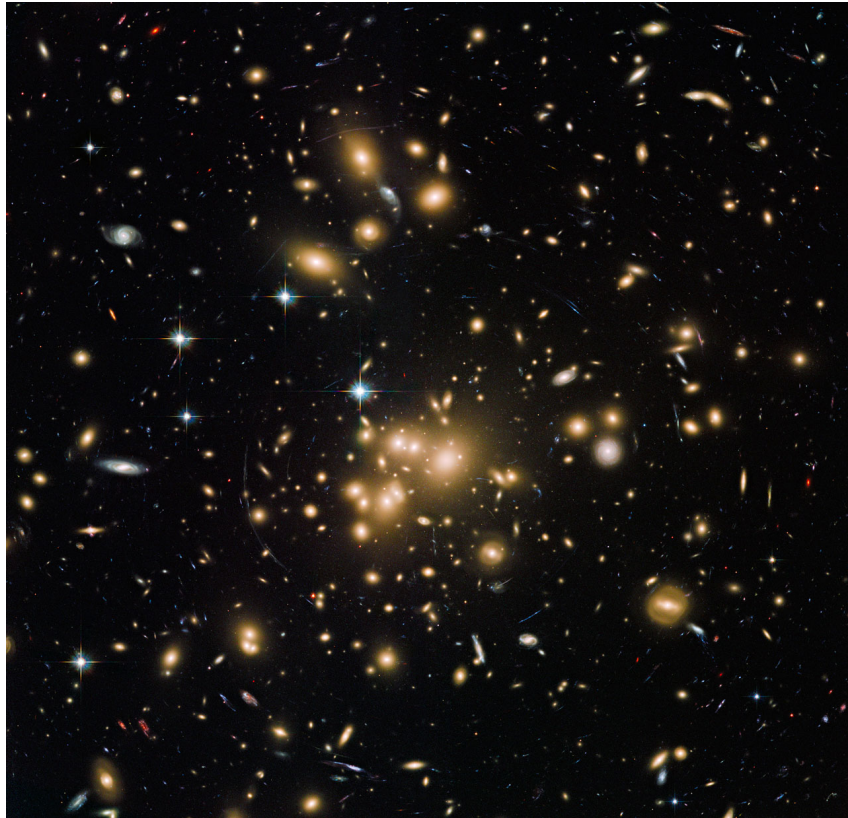


Figure 1.1: Hubble Space Telescope image of galaxy cluster Abell 1689. Many of the galaxies visible are associated with the cluster. Not visible is the ICM or the larger DM halo which constitutes the majority of the cluster mass. Credit: ESA/Hubble [CC BY 3.0]

medium (ICM). While the ICM is very hot, often heated to tens of thousands of kelvin, the typical density is only 10^{-3} particles per cubic centimeter. The ICM gas has two effects: X-ray emission and the Sunyaev-Zel'dovich effect, both discussed further below. The majority of the cluster's mass is located in the DM halo surrounding the cluster (e.g., [Voit 2005](#)).

Figure 1.1 shows a *Hubble Space Telescope* Advanced Camera for Surveys image of galaxy cluster Abell 1689. Many of the cluster member galaxies have a similar yellow color indicating they have similar formation histories (e.g., [Stanford et al.](#)

1998; Eisenhardt et al. 2008), a result substantiated by the analysis of the zeropoint and scatter about the cluster “red sequence” (e.g., Papovich et al. 2011). While the DM halo is not directly imaged, evidence for it can be seen by the very faint gravitational arcs of distant galaxies located behind the cluster.

1.2 Observations of Galaxy Clusters

Observations of galaxy clusters span almost the entire electromagnetic spectrum, from the X-ray to the radio. For our purposes, we focus on three observations which are most useful for estimating cluster mass, and discuss them in order of increasing wavelength.

1.2.1 X-ray

The majority of a galaxy cluster’s baryonic matter is located in the hot ICM (Voit, 2005). The gas which makes up the ICM is falling into the gravitational potential well of the cluster and is heated to tens of megakelvins. Such high temperatures cause the gas to emit X-rays through the bremsstrahlung process. The X-ray luminosity (L_X) of a galaxy cluster correlates with the depth of the gravitational potential well, which leads to an estimate of the cluster’s mass (e.g., Finoguenov et al. 2001).

The L_X of a cluster is a relatively easy measurement, requiring only a few photons to measure. However, for a fixed cluster mass L_X decreases quickly with increasing redshift (e.g., Ettori et al. 2003; Papovich 2008), which limits X-ray selected samples of galaxy clusters to redshifts < 1 . Up until today, X-ray identified clusters have mostly been observed purposefully through targeted *Chandra* or *XMM-Newton* observations. That is soon to change with the *eROSITA* (Pillepich et al., 2012) telescope onboard the Spektrum-Roentgen-Gamma Mission, which will perform an all-sky survey during its four year mission and detect an estimated 50,000 or more clusters.

1.2.2 Optical

Clusters of galaxies have been historically identified as over-densities of galaxies detected in their optical light (e.g., [Abell 1958](#)), and the dynamics of their constituent galaxies can be used to estimate their virial masses. Much like the X-ray observations, the motions of the individual member galaxies (referred to as velocity dispersion) provide an estimate of the depth of the cluster’s gravitational potential well, which is an estimate of the total cluster mass. The constituent cluster galaxies act as tracer particles through the cluster’s potential well. This can be modeled in simulations and has been the focus of many recent studies (e.g., [Evrard et al. 2008](#); [Munari et al. 2013](#); [Saro et al. 2013](#); [Sifón et al. 2013](#); [van der Burg et al. 2014](#)). This type of measurement is important because it is independent of the physics of the ICM, which are always not fully understood. However, these measurements require spectroscopy, which is expensive to obtain.

It is possible to estimate both cluster membership and mass through photometric observations alone, using modern cluster finding algorithms such as the red-sequence Matched-Filter Probabilistic Percolation (redMaPPer; [Rykoff et al. 2014](#)) method which measures a galaxy cluster’s richness, λ . The richness measurement, in the case of redMaPPer, is a probability weighted cluster membership, where the probability is whether or not an individual galaxy belongs to the cluster in question. Figure 1.2 shows the richness correlates strongly with cluster mass on average (e.g., [Rozo et al. 2010](#)), but the absolute mass scale of the optical richness mass estimator and the scatter in cluster mass at fixed optical richness are imprecisely known ([Rykoff et al., 2012](#)).

The Dark Energy Survey (DES; [The Dark Energy Survey Collaboration 2005](#)) will survey 5000 degree² of the southern sky and is expected to detect 100,000 clusters at

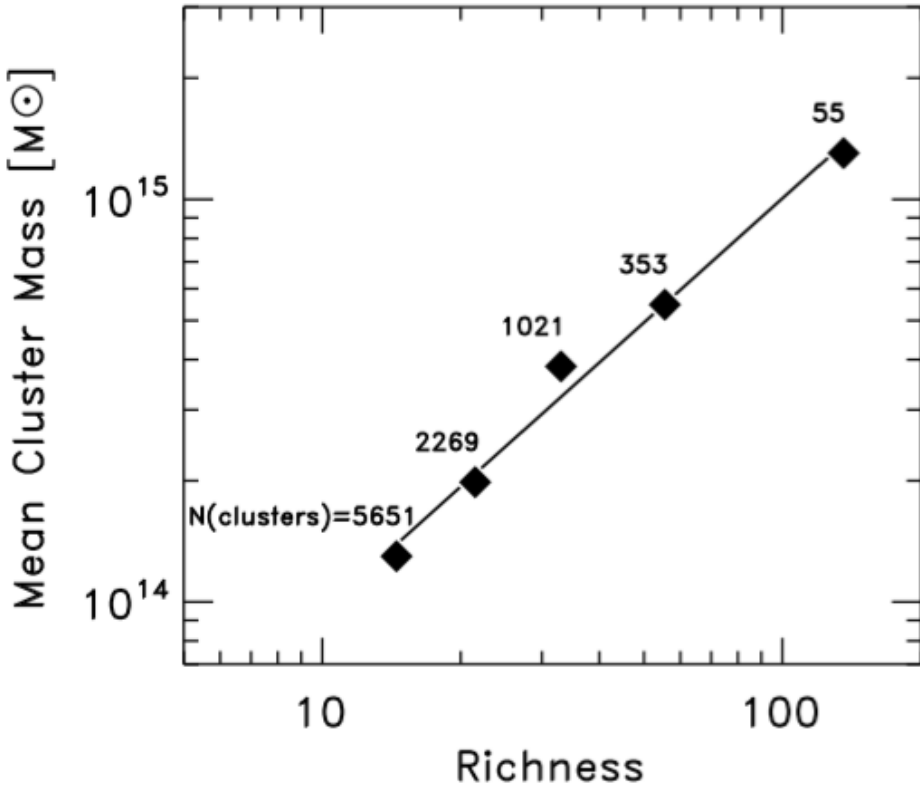


Figure 1.2: The relation between the mean Richness and the mean cluster mass. Derived from stacked weak lensing measurements and adapted from [Rozo et al. 2010](#), the number of clusters in each stack are given above each data point. There is a strong correlation between richness and cluster mass, however, because the data are stacked, the absolute mass scale and scatter in mass at fixed richness are imprecisely known.

$z < 1$ ([Dark Energy Survey Collaboration et al., 2016](#)). The Large Synoptic Survey Telescope (LSST; [LSST Dark Energy Science Collaboration 2012](#)) will also survey an enormous portion of the southern sky, extremely deeply and will identify vast numbers of clusters using optical selection methods (e.g., [Rykoff et al. 2014](#); [Rozo & Rykoff 2014](#)). However, these surveys will be photometric, and any spectral information will be obtained from preexisting datasets. While it is possible to estimate cluster masses using photometric observations, primarily through the richness-mass

relation. Because the primary goal is to have reliable cluster mass estimates, multiple mass-checking observations are required. The spectroscopic calibration of the optical richness-mass relation provided by HETDEX is required to both better calibrate the relation and to obtain the level of precision needed to compete with other mass estimators.

1.2.3 *The Sunyaev-Zel'dovich Effect*

Millimeterwave observations of the Cosmic Microwave Background radiation (CMB) can show the presence of galaxy clusters (e.g., Pipino & Pierpaoli 2010; Vanderlinde et al. 2010; Sehgal et al. 2011; Planck Collaboration 2013; Ruel et al. 2014; Sifón et al. 2016; de Haan et al. 2016). Their existence is detected through an effect called the (thermal) Sunyaev-Zel'dovich effect (SZE; Sunyaev & Zeldovich 1972) caused by inverse Compton scattering, where the CMB photons receive an energy boost when they collide with the high energy electrons of the ICM. This energy boost leads to a shift to higher-frequencies of the CMB spectrum, which is illustrated in Figure 1.3. High resolution images of the CMB can detect a “hole” in the CMB at frequencies below 218 GHz, and a bright spot at higher frequencies due to the shift in the CMB black body spectrum. The temperature of the ICM effects the shift in the CMB frequency. Therefore the shift depends on cluster mass and therefore SZE cluster studies provide a means to test cosmological parameters (e.g., Bocquet et al. 2015; de Haan et al. 2016).

At their completion, the South Pole Telescope (SPT; Carlstrom et al. 2011) and the Atacama Cosmology Telescope (ACT; Swetz et al. 2011) are expected to find approximately one thousand clusters using observations in the millimeter combined with the SZE. Attempts are already underway to calibrate these observations using subsamples of clusters (approximately 100 cluster candidates and 60 clusters

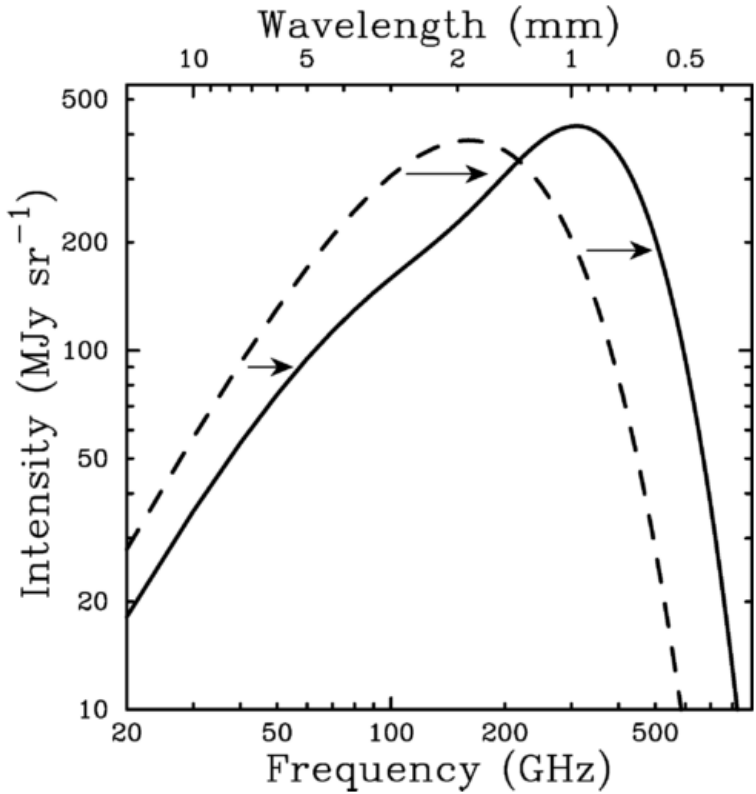


Figure 1.3: Adapted from [Carlstrom et al. \(2002\)](#), the undistorted CMB spectrum (dashed line) is shifted to a higher energy (solid line) by the SZE. Note: this shift is for illustration purposes only, the SZE distortion shown is for a fictional cluster 1000 times more massive than a typical massive galaxy cluster.

respectively) and other observables such as optically-based, virial estimates or X-ray temperature measurements (e.g., [Sifón et al. 2013; Bocquet et al. 2015](#)).

1.3 Cluster Formation: Relationship to Cosmological Parameters

Thought to form out of the primordial density fluctuations in the very early Universe, galaxy cluster formation and growth investigations began in the 1960s (e.g., [van Albada 1960, 1961](#)). Soon thereafter, the hierarchical model of structure formation ([Press & Schechter, 1974; Gott & Rees, 1975; White & Rees, 1978](#)) was

introduced. It suggests the first stars and stellar clumps formed then subsequently merged together with DM and other gas clumps to form the first galaxies which then continued to merge and grow into the clusters and large scale structures we see today. In this model, structures grow through the accretion of smaller systems through the gravity of the DM associated with the cluster. Of course, many complicated astrophysical processes are at work during cluster growth and similarly complicated theoretical models seek to explain these processes. For a detailed review of cluster formation see [Kravtsov & Borgani \(2012\)](#).

Because their initial seeds were planted in the very early Universe, the number and distribution of galaxy clusters across the sky are the fingerprints of the cosmology imprinted on the Universe at its birth. To uncover the underlying cosmology, a detailed understanding of the astrophysical processes that describe the motion of constituent galaxies and their impact on the ICM is required. Therefore, galaxy clusters stand at the intersection of cosmology and astrophysics.

1.4 Cosmology with Galaxy Clusters

The current concordance cosmology is a parametrization of the Big Bang cosmological model where the Universe contains a cosmological constant (Λ ; often referred to as dark energy) and cold dark matter (CDM). It is often characterized by six parameters; the Hubble Constant (H_0), the baryonic matter density (Ω_b), the DM density (Ω_c), the dark energy density (Ω_Λ); the normalization of the power spectrum (σ_8); and the spectral index of the power spectrum (n_s).

Galaxy clusters are sensitive probes of Ω_m , the total mass ($\Omega_b + \Omega_c$) density in the Universe and σ_8 . Galaxy clusters trace the peaks in the universal matter density, often referred to as the power spectrum of matter density fluctuations or the matter power spectrum, much in the same way islands (mountain peaks) trace land masses

through the earth’s oceans. We can constrain the values of Ω_m and σ_8 by comparing the number density of the observed galaxy clusters to that predicted by cosmological models.

The determination of cosmological parameters is done by comparing the number of galaxy clusters per unit mass per unit comoving volume ($n(M, z)$) to models. See [Allen et al. \(2011\)](#) for a comprehensive review or [Murray et al. \(2013\)](#) for a more practical approach. $n(M, z)$, referred to as the halo mass function (HMF) captures the number evolution through a function which defines the particular model used (e.g., [Tinker et al. 2008](#)). Early work by [Press & Schechter \(1974\)](#) and [Bond et al. \(1991\)](#) which assumed spherically symmetric halos, has largely been replaced by more modern fitting functions which, at the expense of an analytical solution, provide more accurate results when fit to simulation data. See [Murray et al. \(2013\)](#) for a review of the most common fitting functions used. Through this approach, the two parameters which clusters are most sensitive to, Ω_m and σ_8 , are in reality measured as $\sigma_8\Omega_m^\alpha$, where the value of α depends on the masses of the halos considered. The degeneracy is broken through the evolution of the HMF as a function of redshift.

The accuracy of the estimates of Ω_m and σ_8 depends on how well the observed HMF can be measured. The correctness of the HMF depends directly on the number of galaxy clusters observed and the accuracy to which the mass of each of the clusters can be estimated. As we discuss below, the identification of large numbers of clusters is not a considerable contributing factor to the uncertainty; the total number of clusters known is only increasing. The accurate recovery of galaxy cluster mass for both very rich clusters (those with high mass) and, importantly, the poor clusters (those with low mass) remains the dominate source of uncertainty (e.g., [Sehgal et al. 2011](#); [Planck Collaboration 2013](#); [Bocquet et al. 2015](#)).

1.5 Galaxy Cluster Surveys as a Data Science Challenge

Astronomy and astrophysics are undergoing a data revolution. Advances in telescope design, detectors, and computing resources have provided more astronomical data than any previous time in the history of the field. Beginning in the early 2000s, astronomical surveys have generated many hundreds of terabytes of data for many millions of sources. In the coming years, this data excess will grow beyond the terabyte regime with observations of billions of astronomical objects.

50,000 or more X-ray identified clusters will be found by the upcoming eROSITA telescope onboard the *Spektrum-Roentgen-Gamma* Mission. SPT and ACT are discovering many thousands of clusters through the SZE. DES and LSST will optically identify many tens of thousands of clusters with much lower masses than are possible with SZE measurements. Taken together, these surveys will produce data products which are both immense and heterogeneous. The multi-wavelength observations ensure there will be many observational parameters associated with each cluster. However, different observation wavelengths probe different cluster physics making them more or less sensitive probes of a specific galaxy cluster's total mass. Varying angular resolutions will also play a role as the instruments used to collect the data will observe in a wide range of wavelength and be both ground and space based. Therefore, the combination of datasets will be a significant challenge.

The ability to associate individual or combinations of observations with the cluster property in question will be a powerful statistical tool. Combining redshift with velocity dispersion measurements could potentially produce more accurate estimates of cluster mass with smaller scatter. However, the process by which the observations are combined is not a trivial exercise. Machine learning offers a promising approach.

1.5.1 Machine Learning

Machine learning (ML) is a branch of computer science focused on the study and construction of computational tools which can learn from and make predictions based on data. In 1959, Arthur Samuel (December 5, 1901 – July 29, 1990), an early computer gaming pioneer, described ML as a “field of study that gives computers the ability to learn without being explicitly programmed” ([Simon, 2013](#)). While, a great deal of programming is often required (discussed further below), such algorithms work by comparing data to a set of models allowing them to make predictions based on the data rather than preprogrammed commands.

ML can be broken into two large categories, unsupervised or supervised learning. “Unsupervised learning” is where the ML algorithm is tasked to make qualitative statements about the structure from unlabeled data. An example would be finding clusters of data inside a large dataset, where the number and location of the clusters are not known *a priori* (e.g., locating galaxy clusters in observations of galaxy positions; see [Section 4.2](#)). “Supervised learning” (e.g., [Mohri et al. 2012](#)) asks the computer to make predictive statements about one variable based on labeled observations of another or combination of other variables. An example could be photometric redshift prediction; given a large number of color and magnitude measurements for a galaxy, predict the most probable redshift.

In this thesis, we are concerned with supervised learning, where we know a relationship exists between two sets of data, and we use a computer algorithm to infer the relationship for us. The algorithm uses a decision tree to learn which works by mapping a set of observations (“features”) of a source to a set of conclusions (“targets”) about that source. If the set of conclusions is finite, then the method becomes a classification tree; if the conclusions are infinite then it becomes a regression tree.

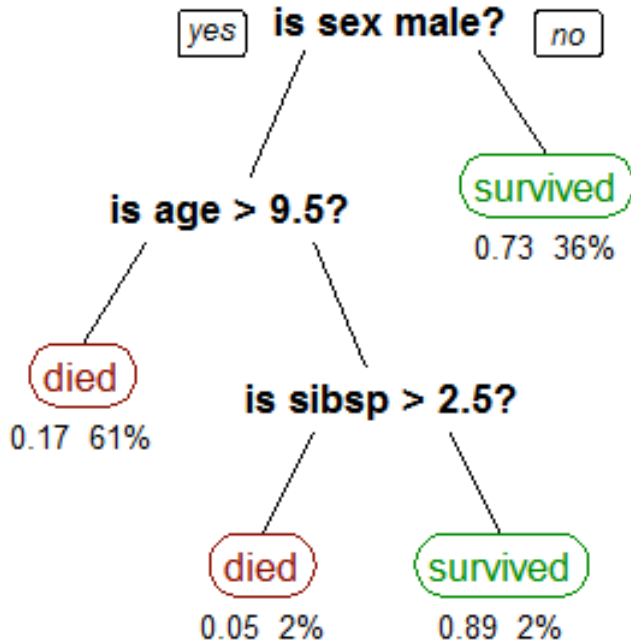


Figure 1.4: Decision tree classifying the survival of passengers on the RMS Titanic. “sibsp” represents the number siblings or spouses aboard, and the numbers below each class represents the probability of survival and fraction of passengers which are classified into each leaf. Credit: Stephen Milborrow (Own work) [CC BY-SA 3.0 or GFDL]

Figure 1.4 shows a simple example of a classification tree for the survivability of passengers on the RMS Titanic. The bolded text is referred to as interior nodes which correspond to a single feature of each passenger in the example, sex, age and number of siblings or spouses. The ending points are called leaves which represent the value of the target variable given the value of the features input into the tree. For this example, there are two possible ending leaves, “died” or “survived.” Using this simple tree we are able to classify all passengers into the two possible classes.

The ML algorithm “learns” this tree by choosing a feature from all available features which best separates the input data into two or more subsets. In the case of the example, this is the sex of the passenger. This becomes the root node. All subsequent nodes are created by repeating this process on each subset associated with the previous node. In such manner, it will split the male passengers by age and then by number of siblings for the males older than 9.5 years. This process is known as a top-down induction of decision trees and is the most common method for creating decision trees from data.

Once the decision tree has been learned, it can be used to classify data not seen before. For example, a 30 year-old, male passenger of the RMS Titanic has a probability of survival of 17% and so will most likely be classified as “died” by the ML algorithm. However, imagine for a moment, with the benefit of hindsight that we know this male passenger survives. Only 17% of the time will the ML method classify the passenger as “survived” based on this decision tree. We can boost the predictive power of the tree by generating many trees and then combining the final predictions at the end. Methods that construct more than one tree are called ensemble methods. For this thesis, we use an ensemble method known as a forest of randomized trees and discuss them further in Section 2.3.3.4 and Section 3.5.4.

1.6 This Work

The goal of this thesis is to understand how a survey such as the Hobby Eberly Dark Energy Experiment (HETDEX; Hill et al. 2008b) can reduce the associated systematic uncertainties of galaxy cluster mass scaling relations, specifically the scatter in the optical richness-cluster mass scaling relation. The relationship between cluster observable and the cluster mass is often noisy and includes large systematic uncertainties (e.g., Rozo et al. 2013; Sereno & Ettori 2015). It is because of these

reasons that the dominant source of uncertainty in deriving cosmological constraints from galaxy clusters is the systematic uncertainty associated with the cluster mass estimates (e.g., Vikhlinin et al. 2009; Rozo et al. 2010; Mantz et al. 2015).

There are two systematic uncertainties present in the optical richness-cluster mass scaling relation: the absolute mass scale is the predicted cluster mass for a given richness, and the scatter (σ) of observed cluster masses (M) at fixed optical richness (λ), $\sigma_{M|\lambda}$. The absolute mass scale can be well calibrated with studies utilizing stacked cluster data (e.g., Baxter et al. 2016; Farahi et al. 2016; Simet et al. 2016) where many cluster measurements are combined to decrease the uncertainty associated with the mass measurement. However, such studies cannot well constrain $\sigma_{M|\lambda}$ because any mass scatter is lost during the stacking process. Understanding, constraining, and ultimately reducing $\sigma_{M|\lambda}$ is paramount to the accurate estimates of cosmological parameters, and an accurate measure of this scatter can lead to a decrease on the error bar on cosmological measures sensitive to cluster abundances (σ_8 and Ω_m) by as much as 50% (Rozo et al., 2010).

At present, few studies have attempted to characterize $\sigma_{M|\lambda}$ (Rozo & Rykoff, 2014; Rozo et al., 2015; Saro et al., 2015; Rykoff et al., 2016). This is due, in large part, to the lack of availability of large-area sky surveys capable of providing the accurate cluster mass estimates for single galaxy clusters required to measure $\sigma_{M|\lambda}$. As we discussed previously, this is quickly changing as new large-area sky surveys across a multitude of wavelengths are detecting many thousands of galaxy clusters.

This thesis seeks to investigate the ability of HETDEX to better constrain $\sigma_{M|\lambda}$. HETDEX is a forthcoming large-area blind spectroscopic sky survey with a primary science mission of measuring the dark energy equation of state at $z \sim 2$. As such, the applicability to galaxy cluster science has not yet been investigated. In addition, because the survey is blind, it will detect nearly as many galaxies at $z < 0.5$

as it will at $z > 2$. Therefore, HETDEX is an enormous, potentially useful dataset for cosmology science using galaxy clusters, but this has not yet been explored. This is a primary goal of this thesis. We discuss HETDEX further in Section 2.2.3.

In Chapter 2, we first use a set of state-of-the-art simulations where we replicate the observing strategy of HETDEX to determine the number and nature of clusters that might be observed. This is accomplished in two ways; in each part we measure the cluster properties, such as redshift, velocity dispersion, and mass of the clusters. First we use targeted observations and perfect knowledge of the observed galaxy clusters, which includes center, membership, and number to recover the desired properties. Secondly, we assume that we know the location, but not the center, membership, or number of constituent galaxies. Then we will employ the HETDEX observing strategy, including realistic pointing pattern, observational magnitude constraints, and spectral sensitivity limits to generate a set of realistic observations.

For the two sets of observations, we use three methods to estimate each galaxy cluster's mass; a traditional power law scaling relation between the observed line-of-sight velocity dispersion and the cluster mass, a probability based method which attempts to combine additional observables with the line-of-sight velocity dispersion, and a ML based approach which also uses multiple observables. Then, using those cluster mass estimates, we attempt to characterize the optical richness-cluster mass relation to better understand the amount of intrinsic scatter when using HETDEX like observations. This enables us to more fully understand and constrain the HMF which, in turn, allows us to make more accurate measurements of σ_8 and Ω_m .

In Chapter 3 of this thesis, we describe a practical test of the approaches we develop in the simulation-based portion of this thesis, we use targeted integral field unit spectroscopic observations of ten intermediate redshift clusters with the Mitchell

Spectrograph (formerly known as VIRUS-P; Hill et al. 2008a), the prototype instrument for HETDEX. Using the spectra obtained for the galaxies associated with each cluster, we determine the cluster membership, determine the cluster mass using the line-of-sight velocity dispersion-cluster mass scaling relation from before, and also combine cluster observables through ML to predict the cluster masses. We again estimate $\sigma_{M|\lambda}$ for the observed clusters.

Finally, in Chapter 4 of this thesis we summarize the main results of this work. In addition, we outline some prospects for future investigations with the HETDEX dataset, and discuss outstanding questions that remain.

2. SIMULATED PERFORMANCE, MASS RECOVERY, AND LIMITS TO COSMOLOGY

2.1 Introduction

Our ability to perform precision cosmology with clusters of galaxies has reached a critical point. The widely accepted Λ CDM model of cosmology makes explicit predictions about the mass function of galaxy clusters in the universe. Measuring this mass function across many redshifts, in turn, provides constraints on the cosmology. Today, large-area sky surveys are providing observations of large numbers of clusters, but systematics in deriving cluster masses dominate the error budget (e.g., [Sehgal et al. 2011](#); [Planck Collaboration 2013](#); [Bocquet et al. 2015](#)). To place further constraints on the Λ CDM model of cosmology, we must decrease these systematics.

As mass is not a direct observable, a lot of work is underway to characterize galaxy cluster masses with an observable feature of galaxy clusters. The goal is to constrain $P(M|z, \vec{x})$ the probability density (P) that a galaxy cluster of given mass (M), located at redshift (z) determined using an observable parameter or parameters (\vec{x}). Generally, cluster mass calibrations are done in one of two ways, through simulations or direct or statistical calibration.

One could use various simulations to attempt to calibrate this observable-mass relation (e.g., [Vanderlinde et al. 2010](#); [Sehgal et al. 2011](#)). However, the primary challenge to this method is the incomplete understanding of the baryonic physics which take place in galaxy cluster environments. While there have been (and continue to be) many improvements in the accuracy and power of simulations it is doubtful that in the coming years they will reach the accuracy level required where the observable-mass relation is dominated only by statistics ([Weinberg et al., 2013](#)).

The second broad method is the direct calibration of cluster masses. This recipe has two distinct but not always independent tracks. The “direct” method uses observations of a relatively small set of clusters and then uses known mass estimators, including X-ray temperatures and luminosities (e.g., Mantz et al. 2010; Rykoff et al. 2014), microwave observations (e.g., Vanderlinde et al. 2010; Sehgal et al. 2011), optical richness (e.g., Abell 1958; Rykoff et al. 2012) or weak lensing (WL; e.g. Rozo et al. 2010) as examples, which provide a “true” mass. This directly calibrates the observable-mass relation which is then applied to a much larger sample. The complications lie in that the “true” masses are, in fact, estimations, and the methods used to recover these cluster masses are subject to their own limitations. X-ray based cluster masses assume hydrostatic equilibrium (e.g., Mantz et al. 2015) which may only be valid for a very small number and range of cluster masses. The Sunyaev-Zel’dovich Effect (SZE; Sunyaev & Zeldovich 1972), which uses the up-scattering of cosmic microwave background (CMB) photons to estimate cluster masses, provides accurate estimations of mass, but the ability to detect low mass galaxy clusters is currently limited by technology (e.g., Carlstrom et al. 2002) and can also be effected by the properties of the intracluster medium (e.g., Pipino & Pierpaoli 2010). WL estimates are, in principle, correct in the mean, but they suffer from signal-to-noise requirements, limiting their usefulness in low mass clusters (where the lensing signal is particularly weak), and potentially suffer from line-of-sight effects as WL is sensitive to all mass along the line-of-sight. Virial mass estimators which determine the cluster mass based on the motions of the member galaxies (e.g., Ruel et al. 2014; Sifón et al. 2015) are promising in that it is a direct measurement of the depth of clusters potential well, but suffer from systematics due to cluster formation physics which disrupts the velocity field.

The statistical method of determining galaxy cluster mass relies not on direct

measurements of individual clusters but the calibration of observables for the entire sample which correlate with cluster mass. One example is the spatial clustering of the galaxy clusters themselves (e.g., [Baxter et al. 2016](#)). See [Weinberg et al. \(2013\)](#) for a comprehensive review. In practice, it will be a combination of the three methods touched on that will provide the most reliable determination of cluster masses.

Large-area sky surveys, both on going and planned, are revolutionizing cluster cosmology using a large range of wavelengths. The South Pole Telescope (SPT; [Carlstrom et al. 2011](#)) and the Atacama Cosmology Telescope (ACT; [Swetz et al. 2011](#)) are discovering many clusters through the SZE. Optically, the on going Dark Energy Survey (DES; [The Dark Energy Survey Collaboration 2005](#)) and planned Large Synoptic Survey Telescope (LSST; [LSST Dark Energy Science Collaboration 2012](#)) will identify many thousands of clusters to much lower masses than is possible with SZE measurements. However, regardless of the discovery method used, spectroscopic follow-up is needed to further constrain $P(M|z, X)$. This follow-up becomes increasing important to help constrain the scatter in the mass estimates of other methods, and provides an additional, independent check of the observable-mass relationship used. But as the cluster dataset grows to many tens of thousands of clusters individual follow-up becomes increasingly impractical. Therefore, large spectroscopic surveys are needed to more fully understand the observable-mass relation of clusters.

The Hobby Eberly Telescope Dark Energy eXperiment (HETDEX; [Hill et al. 2008b](#)) is a trailblazing effort to observe high-redshift large scale structures using cutting edge wide-field integral field unit (IFU) spectrographs. Designed to probe the evolution of the dark energy equation of state etched onto high redshift ($z > 2$) galaxies by the Baryon Acoustic Oscillations (BAO) ([Eisenstein et al., 2005](#)) in the first moments of the universe, the survey will observe two fields for a total of 420 degree² (300 degree², Spring field and 120 degree², Fall field). Tuned to find Ly α

emitting (LAE) galaxies at $1.9 < z < 3.5$, HETDEX expects to find 800,000 LAEs, and more than one million [O II] emitting galaxies at $z < 0.5$ masquerading as high-redshift galaxies ([Acquaviva et al., 2014](#)).

While a large portion of the $\sim 10^6$ interloping lower redshift galaxies will be field (not associated with a bound structure) galaxies, the large area covered by HETDEX is expected to contain as many as 50 Virgo-sized (halo mass $> 10^{15} M_\odot$) clusters at $z < 0.5$. The near-complete spectroscopic coverage allows an unprecedentedly detailed look at a very large number of clusters ranging from group scales to the very massive. In addition to the recovery of accurate dynamical masses, detailed investigations of the of dynamical state of the clusters is possible.

It is unclear how a blind spectroscopic survey with an IFU will effect the recovery of galaxy cluster dynamical properties. Unlike many previous large cluster surveys (e.g., [Milvang-Jensen et al. 2008](#); [Robotham et al. 2011](#); [Sifón et al. 2015](#)) which use multi-object spectrographs, the Visible Integral-Field Replicable Unit Spectrograph (VIRUS; [Hill et al. 2012](#)) used by HETDEX samples the sky in a uniform but sparse way which could excluded member galaxies which would otherwise be included. Secondly, it is not straightforward to use spectroscopic redshifts predominately from emission-line galaxies to interpret the kinematic and dynamical states of the clusters.

This work plans to address these concerns in the following ways. We create and evaluate a HETDEX like selection “function” of galaxies over a similarly large portion of the sky and use well adopted techniques to recover the dynamical properties, such as velocity dispersion and cluster mass. In addition to standard techniques of cluster mass estimation, we investigate probability based and machine learning based approaches of cluster mass prediction. We compare these results to a series of targeted galaxy cluster observations, where each member galaxy is assumed to be

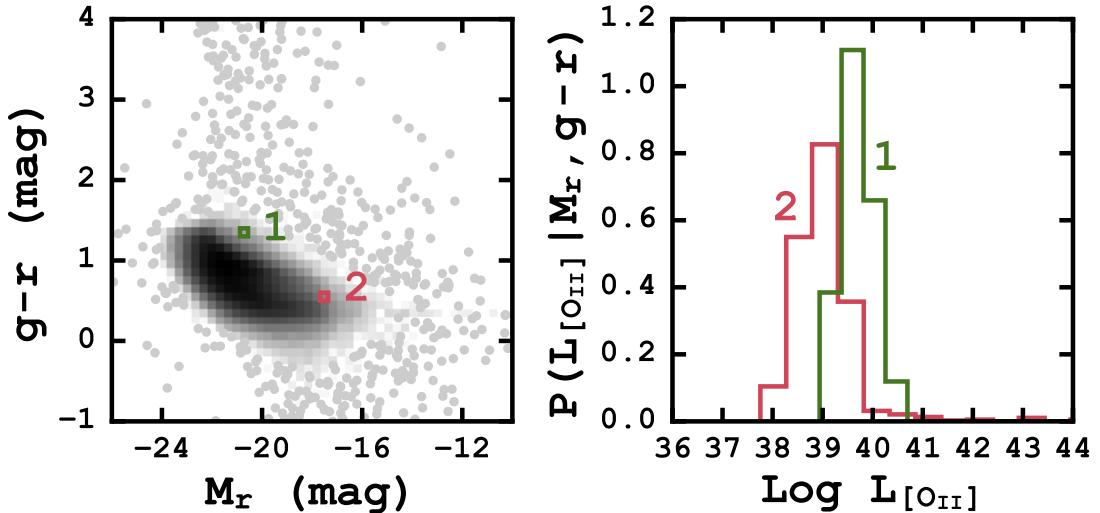


Figure 2.1: *Left:* CMD of 503,113 $z < 0.2$ galaxies take from the SDSS DR12 where the shading scales with the density of points. The two colored boxes show regions containing potential catalog galaxies. *Right:* Probability histograms of the Log [O II] luminosity for the SDSS galaxies located in the two highlighted regions on the right. The [O II] luminosities are assigned to catalog galaxies from slice sampling the probability histogram and converted to fluxes using the redshift of each galaxy.

observed. Each of these observations use realistic uncertainties from galaxy magnitude and line-flux limits. These strategies will better allow future work to predict the number and types of galaxy clusters which should be observed with VIRUS during both the HETDEX survey portion and through targeted follow up observations.

We begin in Section 2.2 by giving an overview of what data is used, how it is created, and how we make our “observations.” Details about the determination of cluster parameters, velocity dispersion, total mass, etc., are discussed in Section 2.3. Next, we present the results of our study in Section 2.4 and discuss their implications in Section 2.5. Finally we summarize our findings in Section 4.1. A follow-up to this work Chapter 3 will investigate how the techniques developed here will work in practice.

Throughout this chapter, we adopt the following cosmological model: $\Omega_\Lambda = 0.714$, $\Omega_M = 0.286$, $\sigma_8 = 0.82$ and $H_0 = 70 \text{ km s}^{-1}\text{Mpc}^{-1}$ (taken from the Buzzard catalogs; see below), assume a Chabrier initial mass function (IMF; [Chabrier 2003](#)), and use AB magnitudes ([Oke, 1974](#)).

2.2 Data and Mock Observations

In this section, we describe the data products and the techniques used to replicate the HETDEX survey. We use the information from a large mock galaxy catalog enhanced by the emission line properties of galaxies in the SDSS to create a realistic “sky” and “observe” it with a HETDEX-like observing strategy.

2.2.1 The Buzzard Mock Catalogs

The Buzzard mock galaxy catalogs cover 398.49 degree² between $4^h < RA < 6^h$ and $-61^\circ < DEC < -41^\circ$ and are derived from a combination of Sub-halo Abundance Matching (ShAM) and ADDSEDs (Adding Density Dependent Spectral Energy Distributions) tied to an in house n-body cosmological simulation. A brief description of the catalog creation is described as follows. The initial conditions are generated with a second-order Lagrangian perturbation theory using 2LPTIC ([Crocce et al., 2006](#)). Dark matter (DM) n-body simulations are run using LGADGET-2 (a version of GADGET-2; [Springel 2005](#)). The Buzzard catalogs adopt the following cosmological parameters: $\Omega_m = 0.286$, $\Omega_\Lambda = 0.714$, $H_0 = 70 \text{ km s}^{-1}\text{Mpc}^{-1}$, $\sigma_8 = 0.82$, and $n_s = 0.96$. The DM halos are identified using the ROCKSTAR halo finder ([Behroozi et al., 2013](#)) which also calculates halo masses.

Galaxy M_r luminosities are added to the velocity peaks using ShAM ([Reddick et al., 2013](#)), and ADDSEDs assign luminosities in the other bands. A M_r -density-SED relation is created using a SDSS training set, and for each mock galaxy the SED of a randomly selected training set galaxy which has a similar M_r and density

is assigned. The result is a mock catalog containing 238 million galaxies with $r < 29$ mag and $z \leq 8.7$.

The catalog information, used in this study, is broken into two large portions. The “truth” files contain the characteristics of each individual galaxy, such as right ascension (RA), declination (DEC), redshift (z), observed and rest-frame magnitudes, and many others. The “halo” files contain information for individual halos, to which many individual galaxies may belong. This includes five estimations of dynamical mass, RA, DEC, z , three dimensional velocity dispersion, and many others. However, the catalogs do not include information for emission lines. We supplement the catalogs by generating this information; the process is described in Section 2.2.2.

We investigate the accuracy of the halo mass distribution by comparing the cumulative number density of halos above a mass (M_{200c}) threshold to the halo mass function (HMF) of Tinker et al. (2008). We calculate the HMF at central redshifts of 0.1, 0.2, and 0.4 using HMFCALC (Murray et al., 2013) and compare it galaxies in a redshift window of $\Delta z \pm 0.01$. We find a very good agreement between the predicted HMF and the observed distribution of clusters.

2.2.2 Conditional [O II] Flux Probability Distribution Functions

We use the SDSS DR12 (Alam et al., 2015) catalogs to assign [O II] emission line strengths to the galaxies in the Buzzard catalog. We use 503,113 objects classified as galaxies selected over $z = 0.02 - 0.2$ with $ZWARNING = 0$ and a measured [O II] line flux signal-to-noise of five. Figure 2.1 shows the color-magnitude diagram (CMD) of M_r and $g - r$ for these galaxies.

To assign an [O II] luminosity to each galaxy in our catalog, we place the catalog galaxies on the same CMD and select all SDSS galaxies in a small 2D ($M_r, g - r$) bin around the galaxy. We extract all of the SDSS galaxies inside that bin and create

a histogram of their [O II] luminosities, the right panel of Figure 2.1. Using a slice sampling technique (Neal, 1997) we assign the catalog galaxy an [O II] luminosity based on the distribution of SDSS galaxies in that bin. In very few cases (1.3% of galaxies) do the $g - r$ and M_r magnitudes of the galaxies in the Buzzard catalog not overlap with the distributions in SDSS. For these objects, we assign them zero [O II] flux, but this has no impact on our analysis. For catalog galaxies with have very few ($1 \leq N < 10$) SDSS galaxies in their respective bin, we assign it the mean [O II] flux.

Figure 2.1 illustrates this process. The numbered boxes in the left panel show the bins corresponding to two example Buzzard galaxies ($M_r, g - r = -17.7, 0.49$ and $M_r, g - r = -21.4, 1.24$). The right panel shows the Log [O II] luminosity distribution functions, $P([O\text{ II}]|M_r, g - r)$, which we use to assign [O II] luminosity to each object. The luminosity is then converted into an [O II] flux through

$$F = \frac{L}{4\pi D_L} \quad (2.1)$$

where D_L is the luminosity distance (e.g., Hogg 1999).

2.2.3 HETDEX

We designed the results of this study to be used in conjunction with HETDEX, a large, blind, spectroscopic survey. HETDEX will measure the redshifts of 8×10^5 LAE galaxies between $1.9 < z < 3.5$ using a collection of 78 wide-field IFU spectrographs covering the wavelength region $3500 - 5500 \text{ \AA}$ at $R \sim 750$ (Hill et al., 2008b). The primary science goal of these observations is to provide $< 1\%$ accuracy measurements of the Hubble expansion parameter and the angular diameter distance at $z \sim 2$. This result will provide significant constraints on the evolution of the dark energy equation of state which is both competitive with, and independent of, constraints derived from

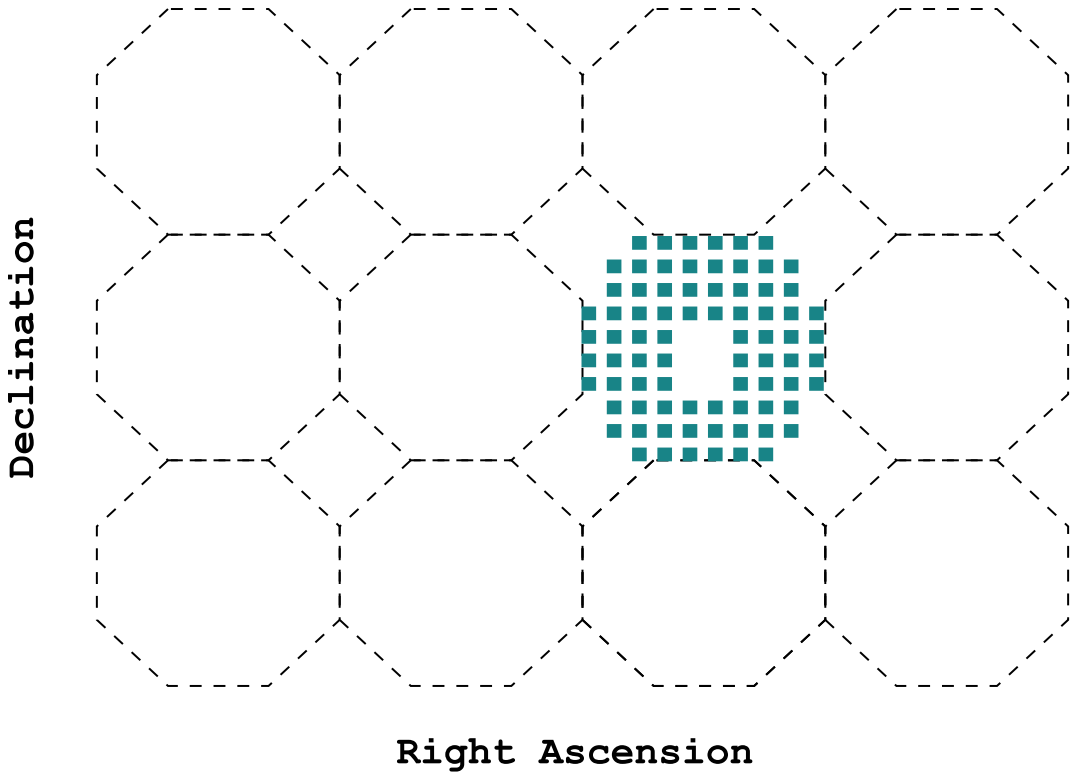


Figure 2.2: Representative observation tiling scheme for the HETDEX $16' \times 16'$ pointings. Each turquoise square represents the position of a single VIRUS IFU, and the dashed octagons approximate the size of a single observation. Inside each IFU HETDEX will achieve near complete coverage through three dithers. See the text for more details.

observations of the Ly α forest.

The entire HETDEX survey will cover 420 degree 2 with a 1/4.5 filling factor over two fields: a ~ 300 degree 2 northern field, and a ~ 140 degree 2 equatorial region. The spectral coverage allows for the detection of [O II] ($\lambda\lambda 3727, 3729$) emitters to $z \sim 0.5$ and Ca H ($\lambda 3968.5$) and K ($\lambda 3933.7$) absorption features to $z \sim 0.4$. The 10σ detection threshold for spectral features will be 3.5×10^{-17} erg s $^{-1}$ cm $^{-2}$ at 5000 Å, or equivalently, $g = 21.9$ mag for continuum objects.

The HETDEX IFU pattern is illustrated in Figure 2.2 by the turquoise squares. Each of the 78 IFUs, are comprised of 448 optical fibers subtending a $50'' \times 50''$ region on the sky (Kelz et al., 2014). The inter-IFU spacing is also $50''$, spanning a total area of $16' \times 16'$ on the sky. The individual IFUs have a fill-factor of $1/3$, which will be completely filled with three dithers of the telescope at each pointing.

2.2.4 Mock Observations

When selecting galaxies from the Buzzard catalog we assume an observation for all galaxies laying within a turquoise, IFU square in Figure 2.2. In practice, this is achieved by three dither positions at each pointing. Galaxies which lie between the IFUs are missed, as well as the galaxies which lie between the pointings, as there is no overlap between one pointing and the next. To cover the 398.49 degree 2 field of the Buzzard catalog we require 5370 pointings where 0.015 degree 2 of each pointing is covered by an IFU. The total area of the sky covered by an IFU is 80.80 degree 2 which gives a filling factor of $1/4.65$, slightly decreased from the expected filling factor of $1/4.5$.

In this chapter we consider two separate observing strategies, Targeted and Survey. The Targeted observations use “direct” observations where each cluster is targeted individually, and every cluster member galaxy is assumed to be observed. The Survey observations mimic the HETDEX observation pattern across the sky, where no cluster is directly targeted and not all cluster member galaxies are observed. Both of these observations have HETDEX-like galaxy detection thresholds (described in the previous subsection), so while a galaxy may be observed, a redshift will only be measured if the galaxy satisfies the continuum brightness or emission line flux limits for the HETDEX survey. For comparison we also include a set of Targeted observations with “perfect” knowledge which assume no detection threshold, if a cluster

member galaxy is observed, it is also detected. This provides an important best-case scenario, and differs from the true cluster properties between we are still calculating the cluster mass from the observed member galaxy velocity dispersions, and represent the best possible mass estimates using velocity dispersion as the observable. These observations provide three levels of quality with “Perfect knowledge” being the highest and Survey being the lowest.

2.3 Recovery of Parameters

In the following subsections, we outline the methods we use to derive the dynamical properties of the galaxy clusters in our sample. The following is, in many cases, a subset of the available methods to derive any single parameter. The specific choice of method may improve or diminish the accuracy of the recovered parameter, but the methods chosen were to facilitate comparison with other observational studies (e.g., Kirk et al. 2015).

2.3.1 Cluster Redshift

The accurate determination of the cluster redshift (z_c) is crucial to the reliability of all following measurements. An incorrect cluster redshift introduces error into the measured line-of-sight velocity (LOSV) and corresponding dispersion, which, in turn, contributes to errors associated with dynamical mass and radius.

In simple terms, the cluster redshift is the mean of the redshifts of all galaxies associated with the cluster, where the mean is the first moment of the velocity (redshift) distribution function $P(z)$. In practice, the first moment is strongly subject to outliers, so we rely instead on the biweight location estimator (Beers et al., 1990) through^{*}:

$$C_{BI} = M + \frac{\sum_{|u_i|<1}(z_i - M)(1 - u_i^2)^2}{\sum_{|u_i|<1}(1 - u_i^2)^2} \quad (2.2)$$

^{*}Implemented as part of the ASTLIB Python library. See <http://astlib.sourceforge.net>

where z_i are the individual redshifts, M is the median redshift and u_i is given by:

$$u_i = \frac{(z_i - M)}{C \text{MAD}}. \quad (2.3)$$

MAD is the median absolute deviation, also defined in Beers et al. (1990), and C is the a tuning constant. We choose $C = 6$ (the suggested value) which balances computational speed and location accuracy.

Although this work assumes that we know each galaxy's redshift to infinite precision, in practice, we find a simple weighted mean provides a reliable estimate of z_c when there are uncertainties on the individual galaxy redshifts.

2.3.2 Line-of-Sight Velocity Dispersion

We calculate the LOSV to each galaxy, where

$$\text{LOSV} = c \frac{z - z_c}{1 + z_c} \quad (2.4)$$

and c is the speed of light, z is the redshift of the individual galaxy, and z_c is the overall cluster redshift described in the previous subsection.

We follow the maximum likelihood method of Walker et al. (2006) to estimate the line-of-sight velocity dispersion (LOSVD). We maximize the probability function

$$P(\{v_1, \dots, v_N\}) = \prod_{i=1}^N \frac{1}{\sqrt{2\pi(\sigma_i^2 + \sigma_{1D}^2)}} \exp\left[-\frac{1}{2} \frac{(v_i - \langle u \rangle)^2}{(\sigma_i^2 + \sigma_{1D}^2)}\right] \quad (2.5)$$

where σ_{1D} , $\langle \mu \rangle$, and σ_i is the LOSVD, the average radial velocity and the error on the individual LOSVs (which we have assumed to be normally distributed) respectively, using a Monte Carlo Markov Chain (MCMC) sampler (emcee[†]; Foreman-Mackey

[†]<http://dan.iel.fm/emcee/current/>

et al. 2013) which is based on affine-invariant ensemble sampler (see Goodman & Weare 2010 for details on affine-invariant samplers). We draw twenty thousand samples from the posterior probability distribution using simple priors, $\langle \mu \rangle$ lies between the maximum and minimum LOSV and $0 < \sigma_{1D} < 1400 \text{ km s}^{-1}$. We set the upper limit on the LOSVD as the LOSVD corresponding to a 10^{16} M_\odot cluster at $z \sim 0.0$, higher mass than any expected cluster in Buzzard. When the full distribution of LOSVDs is not used, the final LOSVD is quoted as the median value of the posterior probability distribution with 68% error bars defined as the square root of second moment of the same distribution, the standard deviation.

In principle, a single statistic such as the biweight scale estimator or the gapper estimator (both from Beers et al. 1990) with many bootstrap resamplings could be used to construct a distribution of σ_{1D} . In simple tests where the values of both σ_{1D} and $\langle \mu \rangle$ are known, the 68% error bars derived from the MCMC method give slightly better results with the true LOSVD value bracketed by the error bars in $\sim 68\%$ of the cases versus $\sim 57\%$ with bootstrapping and a single statistic. In addition, we prefer the maximum likelihood method for its straight forward treatment of the errors in the LOSV measurements, which will become important in the practical application to real data (e.g., Chapter 3).

2.3.3 Estimates of Cluster Mass

2.3.3.1 Power Law Based Method

The relationship between the LOSVD and cluster dynamical mass has been the focus of several many (e.g., Evrard et al. 2008; Saro et al. 2013; Sifón et al. 2013; van der Burg et al. 2014), where the relationship for the mass enclosed by r_{200c} takes the form

$$M_{200c} = \frac{10^{15}}{h(z)} \left(\frac{\sigma_{1D}}{A_{1D}} \right)^{1/\alpha} \text{M}_\odot \quad (2.6)$$

with $A_{1D} = 1177 \pm 4.2$ km s $^{-1}$ (Munari et al. 2013; referred to as σ_{15} in Evrard et al. 2008 and other works), $\alpha = 1/3$, $h(z) = H(z)/100$, and σ_{1D} is the LOSVD of the velocity tracers (dark matter particles, subhalos or galaxies). $H(z) = H_0 E(z)$ and $E(z) = \sqrt{\Omega_m(1+z^3) + \Omega_\Lambda}$.

A growing body of work suggests that there is a significant difference in the observed LOSVD depending on the velocity tracers used. Specifically, while there is little difference between using galaxies and their host DM subhalos, there is a significant over estimation of the LOSVD when using galaxies/subhalos compared to DM particles (Munari et al., 2013). We follow other works (e.g., Kirk et al. 2015; Sifón et al. 2016) using the scaling relation, given in Equation 2.6 to facilitate comparisons with other observational studies, which rely on galaxies as tracers.

2.3.3.2 Other Estimates of Dynamical Mass – Introduction

In the following subsections we use two methods to predict the mass of a cluster based on other observables. Often the cluster mass is estimated based on a single observable, X-ray temperature, LOSVD, richness and others (see Section 2.1 for referenced examples). Here we combine many observables to attempt to correct the mass inferred solely from the velocity dispersion. The first method is traditional “probability based” where we marginalize over a series of observables to find the most probable cluster mass. The second is based on a machine learning (ML) algorithm which attempts to infer the relationship between the observables and the desired output, the cluster mass. Both of these methods are examples of supervised learning algorithms where the relationship between the observable parameters and the target parameter (the cluster mass) are both known.

As with any predictive analysis it is important to test the model on data that the model has not seen before. This prevents over-fitting. In the following subsections

we take all of the observed clusters, our full sample, split them, and generate a *training* and *testing* set (e.g., Ripley 2007; Xu et al. 2013; Ntampaka et al. 2015a,b; Acquaviva 2016). Traditionally, the training set is a set of data used to infer possibly predictive relationships. The test set of data is then used to assess the correctness of the predictive relationship. Our data is randomly split into 70% training and 30% testing. We follow the ML convention and refer to the individual clusters in each set as a “sample”, and the parameters associated with the cluster (z , LOSVD, mass, etc.) as “features”.

2.3.3.3 Probability Based

For internal consistency between this and the ML based method we use 70% of the clusters to establish a conditional probability density of $P(M_{200c}|\vec{x})$ which we then use as the cluster mass probability density for the remaining clusters with similar features. In this way we, “train” the probability density using the existing simulated data, and apply it to the “test” sample (the remaining 30% of the data not used as the training set).

In this method, the cluster masses are predicted using the method illustrated in Figure 2.3. The left panel shows the two dimensional (joint probability) projections of the posterior probability distributions of the feature training data. The conditional probability of the cluster mass $P(M_{200c}|\vec{x} = \{x_1, x_2, \dots\})$ (shown in the right panel) is determined by selecting a region in the joint probability distribution. For example, using the LOSVD and redshift features we create $P(M_{200c}|\vec{x})$ for two test galaxies, shown by the green and pink boxes in the left panel of Figure 2.3. These example galaxies have features $\vec{x} = \{\sigma = 200 \text{ km s}^{-1}, z = 0.16\}$ and $\vec{x} = \{\sigma = 400 \text{ km s}^{-1}, z = 0.36\}$. We select all galaxies in our training sample with similar features and create the conditional probability distributions shown in the right panel.

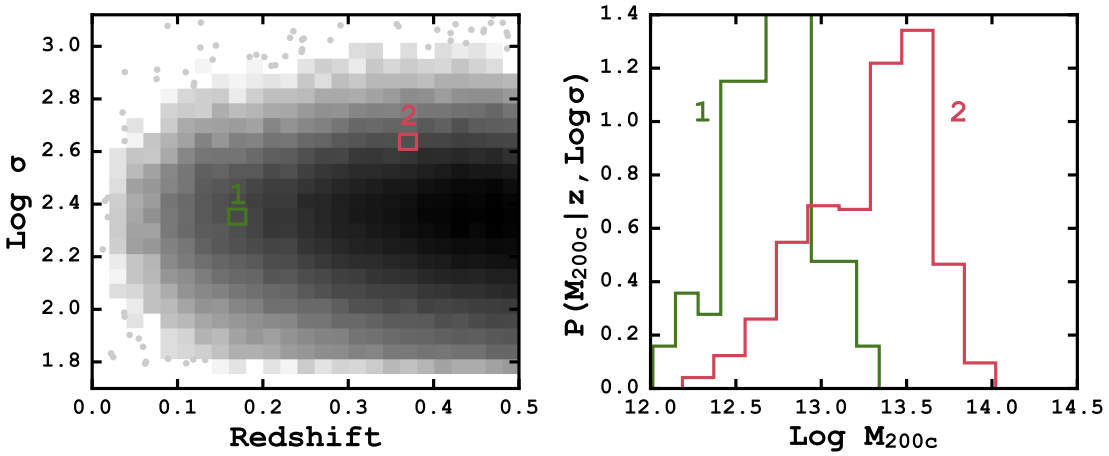


Figure 2.3: Illustration of the probability based cluster mass prediction method. *Left:* The two dimensional posterior probability distribution of LOSVD and redshift used to determine the correct cluster mass. The pink and green rectangles show the locations of two example galaxies used to create the conditional probability distribution of the mass, $P(M_{200c}|\vec{x})$. *Right:* The conditional probability distribution of the cluster mass for the two example galaxies. See text for a complete description.

For the clusters making up the *test* sample the mass is unknown (it is what we are trying to predict) but the other features are known. To determine the mass probability distribution of a test cluster, $P(M_{200c})$, we combine the conditional probability distribution, $P(M_{200c}|\vec{x})$, created previously with the probability distribution of σ , the LOSVD, through Equation 2.7.

$$P(M_{200c}) = \int P(M_{200c}|\vec{x}) P(\sigma) d\sigma P(z) dz \quad (2.7)$$

The expected mass is determined by calculating the first moment of the probability density. This becomes our “predicted” cluster mass, M_{pred} .

$$M_{pred} = \int M_{200c} P(M_{200c}) dM_{200c} \quad (2.8)$$

The confidence interval associated with this prediction can be estimated two ways. First, by calculating the second moment of the probability density through

$$\text{Var} = \int (M_{200c} - M_{pred})^2 P(M_{200c}) dM_{200c} \quad (2.9)$$

or by drawing many samples from $P(M_{200c})$ and calculating the values at the 16th and 84th percentile. In practice we find that both methods produce similar results for a large number of trials. Therefore, we quote predicted masses as the most probable mass given by Equation 2.8 and associated 68% error estimated through the square root of Equation 2.9.

2.3.3.4 Machine Learning Based

The cluster mass estimation in this section relies on a ML technique known as an ensemble method, where many estimators are created by a single learning method with the goal of improved generalization and robustness compared to a single estimation. Ensemble methods (e.g., [Caruana & Niculescu-Mizil 2006](#)) come in two general flavors. Averaging methods average (hence the name) the estimators to produce a single prediction. Boosting estimators build estimates sequentially by attempting to address poor performing estimators in each previous step, hence “boosting” the predictive power.

Here we use an averaging ensemble learning method known as a forest of randomized decision trees, often shorten to just random forest ([RF](#); [Tin Kam Ho 1995, 1998](#)). Decision trees can be visualized a flow chart where forks are the branches of the tree. The path along the tree is decided by the values of the feature(s) at each branch. RF estimators use a random subset of the training set at each fork to decide which path should be followed. The final prediction is then the mean of all the final predictions from the trees. We use RF regression methods as implemented

in SCIKIT-LEARN ([Pedregosa et al., 2012](#)).

The ML method generates “prediction intervals” between observed and derived quantities (rather than “confidence intervals”). A prediction interval is an estimate of the interval encompassing future observations, with a certain probability. And, unlike confidence intervals, which describe uncertainties on the different moments of a population, a prediction interval is unique to each prediction. In many regression analyses, such as linear fitting, the prediction intervals are based on underlying assumptions of normally distributed residuals. However, RF estimators do not have any such assumptions and require special treatment.

The prediction intervals here are based on the general method of quantile regression forests ([Meinshausen, 2006](#)). The general idea is that all response variables are recorded, not just the mean. Then the prediction can be returned as the full conditional probability distribution of all responses, which allows us to generate the prediction intervals. We report the 68% prediction interval as the square root of the second moment of the full conditional probability distribution.

2.4 Results

Here we explore the cluster member recovery rate and mass estimates for the two observing strategies, Targeted, and Survey. Targeted observations are direct observations of a cluster where each cluster member galaxy, above the detection thresholds (see Section [2.2.4](#)), is observed. Survey observations mimic the HETDEX observation strategy such that no cluster is directly observed, and only the cluster member galaxies above the detection threshold and within an IFU (see Figure [2.2](#)) are observed. We discuss the accuracy of cluster dynamical mass derived from both the power law scaling relation (see Equation [2.6](#)) and through the probability and ML methods. We also compare the results from the Targeted and Survey observing

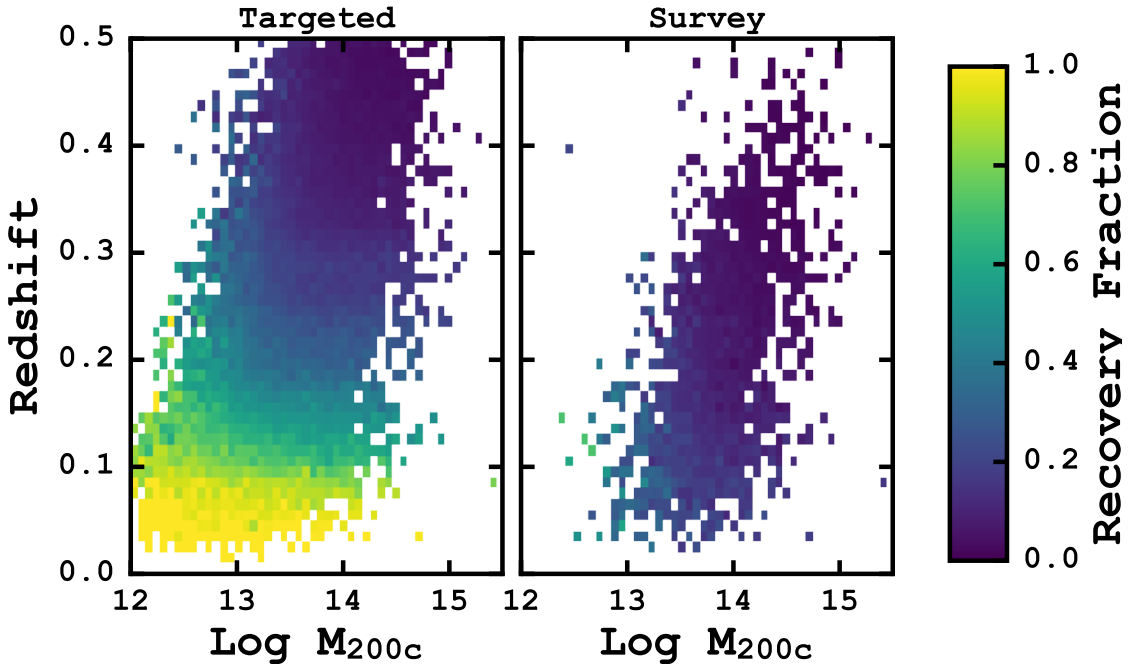


Figure 2.4: Recovery fractions (N_{obs}/N_{True}) of cluster member galaxies as a function of redshift and true cluster mass for the Targeted and Survey observing strategies. We have applied HETDEX-like observational limits on the cluster galaxy detection, and require at least five galaxies to be detected for a cluster to be recovered. The shading indicates the mean recovery fraction for clusters within each small bin of redshift and cluster mass. We find a significant decrease in the recovery of galaxies with increasing redshift. This leads to lower recovery fractions of high mass clusters as many only exist at larger redshifts. The significant decline in the number of galaxies observed with the Survey strategy is due to gaps in the VIRUS IFU, where the galaxies are missed.

strategies to the results of a “Perfect” survey, where the redshift of each galaxy, regardless of observational limits, in the cluster is known perfectly.

2.4.1 Recovery of Cluster Members

As discussed in Section 2.2.4, the observational constraints place limits on the total number of clusters member galaxies expected to be recovered. Knowing these

limits will provide important information for potential future follow up or Targeted observations. We recover 14,189 clusters with Targeted observations and 1,760 clusters with Survey observations, where we require a detection of $N_{obs} \geq 5$ galaxies for a cluster to be detected. Figure 2.4 shows the recovery fraction of member galaxies, the number of observed galaxies divided by the number of actual galaxies (N_{obs}/N_{True}), as a function of both redshift and cluster mass. As expected, the Targeted observing strategy where the individual clusters are targeted through several dithers to ensure near complete coverage, performs significantly better than the Survey observing strategy across all redshifts and cluster masses. With Perfect knowledge, recovery fraction would be unity across all redshifts and cluster masses where clusters exist.

For the Targeted observations, shown in the left panel of Figure 2.4, the pattern of decreasing recovery fraction as a function of redshift (y-direction) is due to the observational limits imposed. Because HETDEX is limited in apparent magnitude, we expect to recover fewer galaxies at higher redshift, where the galaxies are often below our 5σ detection threshold. For example, we tested this by constructing an artificial HETDEX-like survey, limited by volume for all galaxies with $M_g < -11$. In this case, our recovery fraction increases to $> 70\%$, which shows that the flux limit is dominating the (lower) recovery of our flux-limited survey.

For the recovery fraction as a function of true cluster mass (x-direction), we find a general decrease in the recovery fraction of member galaxies with increasing cluster mass. This is entirely a result of the flux limited survey (see previous paragraph). Because there are few high mass ($M_{200c} > 5 \times 10^{14} M_\odot$) clusters, many of which are at moderately high redshift, the higher redshift cluster members suffer from the limiting apparent magnitude and suppress the recovery fraction at fixed mass. If we were to limit the Survey to $z < 0.2$ we find the recovery fraction of clusters, across

all masses, increases substantially, and we find a much more consistent detection fraction across all masses.

For the Survey observations, the right panel of Figure 2.4, all of the same effects are at work. In addition we find that the fill factor, due to the gaps between the VIRUS IFUs, further reduces the number of cluster members detected. The median recovery fraction in Survey observations is almost exactly 4.5 times less than the Targeted median recovery fraction. As the total filling factor of the Survey observations increases the two lines will converge.

The recovery fractions in Figure 2.4 are an outcome of the magnitude limit and [O II] line-flux limit of the survey. For Perfect observations, we would detect all members across all cluster masses and redshifts. Recovery fractions of clusters located at the low end of the redshift distribution will improve the most by follow-up targeted observations. But generally, the number of members observed (and subsequently more accurate cluster mass estimates) will benefit from follow-up observations regardless of the redshift. So follow-up observations should be tailored to the specific science goal.

2.4.2 Mass estimates

In this section we discuss the accuracy of the recovered masses compared to the true cluster mass from a set of observations. We report on three methods, the power law based approach (Eq. 2.6), the probability based approach (Section 2.3.3.3) and the ML based method (Section 2.3.3.4). For each method we consider observations with Perfect knowledge, Targeted observations and Survey observations. The cluster masses presented here are recovered using the best possible conditions, where we have perfect knowledge of the cluster membership. In reality, the mass recovery levels presented in this section represent an upper bound (the best) on the accuracy

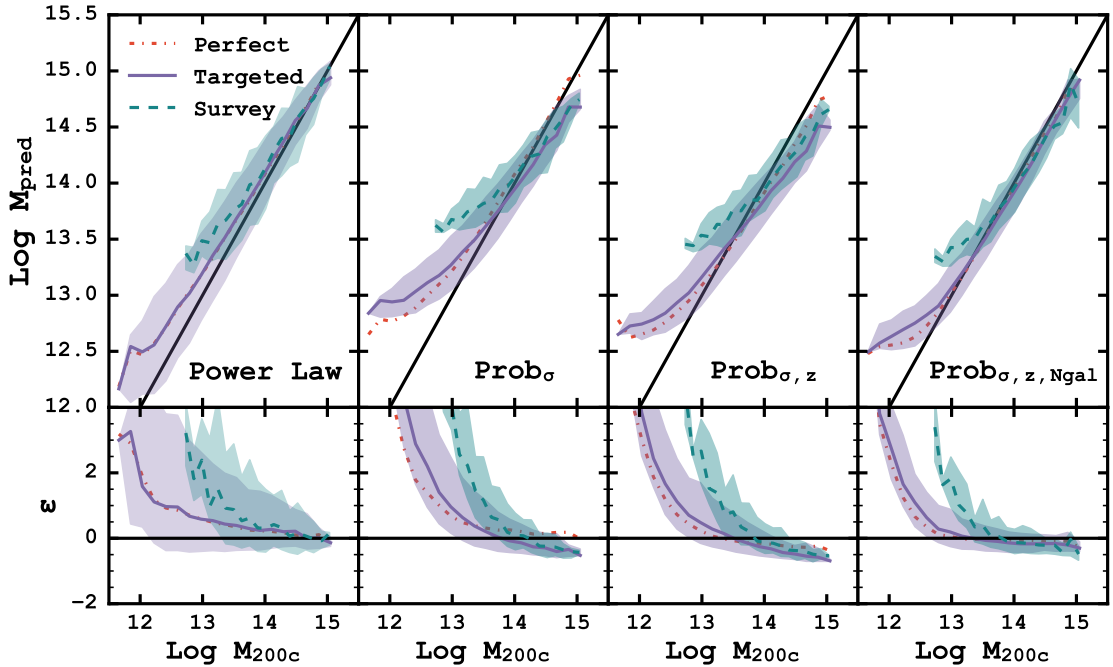


Figure 2.5: Mass predictions for the power law scaling relation (Equation 2.6) and the probability based technique with different input features as a function of true cluster mass. The bottom row of panels shows the fractional error (Equation 2.12) also as a function of true cluster mass. The solid black line shows the 1:1 relation, in both panels, between M_{200c} and M_{pred} . The orange, dash-dotted line is the median predicted mass for perfect observations. The solid, purple line is the median predicted mass for the Targeted observing, and the green, dashed line is the median recovered mass for the HETDEX-like observations. The shaded regions represent the 68% scatter around the median values.

achievable through this method.

Because it represents the best possible scenario, the Perfect knowledge observations should serve as a baseline to compare the power law based, probability based and ML cluster mass recovery methods. And, while there are many possible metrics

to evaluate performance, we compute two: the average bias (given in Table 2.1)

$$\mu_{bias}(y, y_{pred}) = \frac{1}{N} \sum_{i=1}^N (y_{pred,i} - y_i). \quad (2.10)$$

where y are the true values and y_{pred} are the predicted values, and the scatter about the bias (given in Table 2.2)

$$\sigma_{bias}(y, y_{pred}, \mu_{bias}) = \left[\frac{1}{N-1} \sum_{i=1}^N (y_{pred,i} - y_i - \mu_{bias})^2 \right]^{1/2} \quad (2.11)$$

with N clusters in a given bin. Both metrics evaluate how closely the ensemble of predicted cluster masses are to the true cluster masses.

We begin with the Perfect knowledge observations. These observations are of the same clusters as the Targeted observations but without any observational limits. The cluster masses predicted by Equation 2.6 gives the following results. For clusters with masses between $\text{Log M/M}_\odot = 13 - 15.5$, we find $\mu_{bias} = 0.148 \pm 0.008$ dex and $\sigma_{bias} = 0.193 \pm 0.001$. The scatter in recovered masses can be attributed to both physical and numerical effects. The presence of any in-falling matter onto lower mass clusters can introduce a significant amount of substructure, leading to artificial biasing of the measured LOSVD to higher values, increasing the predicted mass (e.g., Ntampaka et al. 2015a). Also, as the number of cluster galaxies decreases the LOSVD PDF is poorly sampled leading to poorly recovered cluster masses due to numerical effects.

For the Targeted and Survey observations the power law predicted cluster masses give $\mu_{bias} = 0.135 \pm 0.003$ dex, $\sigma_{bias} = 0.370 \pm 0.002$ and $\mu_{bias} = 0.148 \pm 0.008$ dex, $\sigma_{bias} = 0.324 \pm 0.006$, respectively. So for the clusters that we detect with Survey observations, we obtain similar levels of accuracy as to the Targeted observations, on

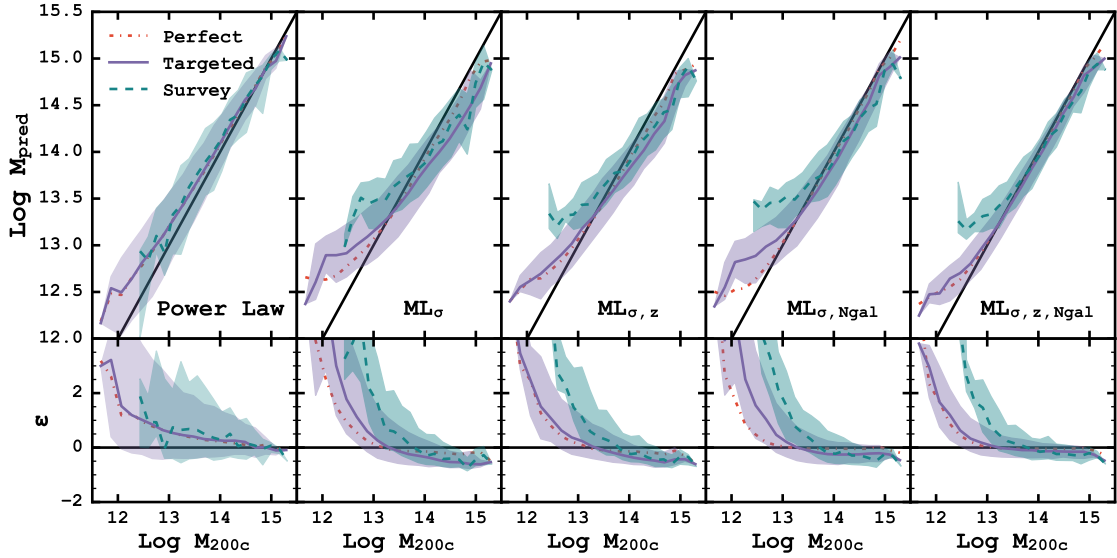


Figure 2.6: Mass predictions for the power law scaling relation (Equation 2.6) and the ML based technique with different input features as a function of true cluster mass. The bottom row of panels shows the fractional error (Equation 2.12) also as a function of true cluster mass. The solid black line shows the 1:1 relation. The orange, dash-dotted line is the median predicted mass for perfect observations. The solid, purple line is the median predicted mass for the Targeted observing, and the green, dashed line is the median recovered mass for the HETDEX-like observations. The shaded regions represent the 68% scatter around the median values.

the average. This does not mean that the Survey observations cannot be improved by Targeted observations. In fact, when comparing only the galaxies which overlap between the two samples the bias and scatter of the Targeted observations is significantly decreased as more cluster member galaxies are detected, better sampling the LOSVD PDF. The Targeted observations performs similarly on the average because many lower mass clusters are included in the sample, increasing the bias of the overall sample.

In both Figures 2.5 and 2.6, we show the predicted (M_{pred}) versus true (M_{200c}) cluster masses for each of the two observing strategies. The lower panels show the

fractional cluster mass error defined as:

$$\epsilon = (M_{pred} - M_{200c})/M_{200c} \quad (2.12)$$

where M_{pred} is the predicted cluster mass and M_{200c} is the true cluster mass. Higher values of ϵ indicate the predicted cluster mass exceeds the true cluster mass.

Qualitatively, the top panels of Figures 2.5 and 2.6 show that both the probability based and ML based methods out perform (closer to the black 1:1 relation) the power law method when taking advantage of other cluster observables (z , N_{gal} , etc.). Generally, we find that the single parameter probability and ML methods perform significantly poorer than the power law method, especially at low cluster masses. When combined with the cluster redshift, the predicted cluster masses are improved, because the range of cluster masses decrease with increasing redshift (see Figure 2.4). The final addition of the number of observed galaxies, N_{gal} acts as a type of richness estimate, and significantly improves both the bias and the amount of scatter in the predicted masses.

Table 2.1: Mean bias (Eqn. 2.10) for different bins of predicted cluster mass. This table shows the bias in the predicted cluster mass for the perfect (top section), Targeted (middle section), and Survey (bottom section) observations in different predicted mass bins. The different mass recovery strategies are given in the leftmost column. It can be used to understand how the predicted cluster mass differs from the true cluster masses. Positive numbers indicate the predicted cluster mass over estimates when compared to the true cluster mass.

Method	Bins – Log M_{pred}					
	12.5 – 13	13 – 13.5	13.5 – 14	14 – 14.5	14.5 – 15	15 – 15.5
Perfect Observations						
Power Law	0.23 ± 0.007	0.16 ± 0.003	0.11 ± 0.002	0.07 ± 0.004	0.02 ± 0.011	-0.07 ± 0.045
Prob	0.32 ± 0.005	0.16 ± 0.003	0.10 ± 0.002	0.07 ± 0.004	0.05 ± 0.012	-0.18 ± 0.078
	0.17 ± 0.005	0.01 ± 0.003	-0.06 ± 0.002	-0.11 ± 0.015	-0.14 ± 0.012	-0.38 ± 0.159
ML	0.04 ± 0.009	-0.02 ± 0.002	-0.02 ± 0.002	-0.05 ± 0.014	-0.22 ± 0.126	...
	0.14 ± 0.006	-0.01 ± 0.003	-0.07 ± 0.003	-0.09 ± 0.005	-0.11 ± 0.014	-0.17 ± 0.090
Prob	0.12 ± 0.005	-0.01 ± 0.003	-0.06 ± 0.003	-0.08 ± 0.004	-0.11 ± 0.012	-0.24 ± 0.076
	0.04 ± 0.004	-0.02 ± 0.002	-0.02 ± 0.002	-0.02 ± 0.002	-0.02 ± 0.006	-0.08 ± 0.041
ML	0.04 ± 0.003	-0.02 ± 0.002	-0.02 ± 0.001	-0.02 ± 0.002	-0.02 ± 0.005	-0.08 ± 0.043
Targeted Observations						
Power Law	0.20 ± 0.008	0.13 ± 0.005	0.10 ± 0.005	0.09 ± 0.007	0.02 ± 0.014	-0.08 ± 0.043
Prob	0.40 ± 0.005	0.17 ± 0.003	0.02 ± 0.004	-0.08 ± 0.006	-0.19 ± 0.015	-0.35 ± 0.122
	0.25 ± 0.005	0.08 ± 0.003	-0.06 ± 0.003	-0.21 ± 0.015	-0.35 ± 0.016	-0.59 ± 0.145
ML	0.13 ± 0.004	0.01 ± 0.003	-0.05 ± 0.003	-0.12 ± 0.018	-0.44 ± 0.177	...
	0.26 ± 0.006	0.02 ± 0.004	-0.13 ± 0.005	-0.24 ± 0.008	-0.35 ± 0.022	-0.39 ± 0.054
Prob	0.18 ± 0.005	0.03 ± 0.003	-0.10 ± 0.004	-0.21 ± 0.006	-0.31 ± 0.021	-0.33 ± 0.063
	0.22 ± 0.005	0.00 ± 0.004	-0.13 ± 0.004	-0.16 ± 0.007	-0.13 ± 0.014	-0.19 ± 0.059
ML	0.09 ± 0.004	-0.01 ± 0.002	-0.05 ± 0.002	-0.08 ± 0.004	-0.08 ± 0.010	-0.19 ± 0.060

Table 2.1 Continued

Method	Bins – Log M_{pred}					
	12.5 – 13	13 – 13.5	13.5 – 14	14 – 14.5	14.5 – 15	15 – 15.5
	Survey Observations					
Power Law	0.17 ± 0.068	0.17 ± 0.023	0.13 ± 0.014	0.07 ± 0.014	0.01 ± 0.022	-0.09 ± 0.062
Prob	σ	0.77 ± 0.030	0.42 ± 0.011	0.18 ± 0.008	-0.03 ± 0.009	-0.18 ± 0.017
	σ, z	0.61 ± 0.036	0.29 ± 0.012	0.08 ± 0.008	-0.11 ± 0.009	-0.38 ± 0.118
Prob	σ, z, N_{gal}	0.48 ± 0.038	0.18 ± 0.011	0.02 ± 0.007	-0.08 ± 0.008	-0.50 ± 0.203
	σ	0.57 ± 0.046	0.24 ± 0.015	0.02 ± 0.012	-0.17 ± 0.013	-0.28 ± 0.027
ML	σ, z	0.48 ± 0.034	0.20 ± 0.013	0.03 ± 0.009	-0.13 ± 0.011	-0.26 ± 0.021
	σ, N_{gal}	0.55 ± 0.043	0.22 ± 0.013	0.00 ± 0.010	-0.14 ± 0.011	-0.22 ± 0.025
ML	σ, z, N_{gal}	0.42 ± 0.029	0.13 ± 0.011	-0.00 ± 0.007	-0.08 ± 0.008	-0.14 ± 0.016
						...
						-0.19 ± 0.079
						-0.19 ± 0.079

We quantify the bias and scatter for all of the different cluster mass recovery strategies and observing methods in Table 2.1 and Table 2.2. It serves as a type of look up table for future cluster observations with HETDEX. The columns represent bins of predicted galaxy cluster mass and the individual values show the bias and scatter of the true cluster mass. The three horizontal sections represent Perfect, Targeted and Survey observations respectively. So, for example, if a cluster mass is predicted using the $\text{ML}_{\sigma,z}$ method and Targeted observations to be $\text{Log M/M}_\odot = 13 - 13.5$, it is biased upward by 0.03 ± 0.003 dex and has a scatter of 0.24 ± 0.009 dex.

Table 2.2: Mean scatter (Eqn. 2.11) in cluster mass after bias correction for different bins of predicted cluster mass. This table shows the scatter in the predicted cluster mass for the perfect (top section), Targeted (middle section), and Survey (bottom section) observations in different predicted mass bins. The different mass recovery strategies are given in the leftmost column. It can be used to understand how the predicted cluster mass differs from the true cluster masses.

		Bins – Log M_{pred}					
Method		12.5 – 13	13 – 13.5	13.5 – 14	14 – 14.5	14.5 – 15	15 – 15.5
Perfect Observations							
Power Law		0.34 ± 0.005	0.22 ± 0.002	0.16 ± 0.002	0.14 ± 0.003	0.14 ± 0.008	0.11 ± 0.040
Prob	σ	0.26 ± 0.004	0.20 ± 0.002	0.16 ± 0.002	0.14 ± 0.003	0.16 ± 0.009	0.19 ± 0.071
	σ, z	0.23 ± 0.003	0.19 ± 0.002	0.16 ± 0.002	0.55 ± 0.010	0.16 ± 0.009	0.39 ± 0.143
	σ, z, N_{gal}	0.47 ± 0.007	0.14 ± 0.001	0.10 ± 0.001	0.54 ± 0.010
	σ	0.29 ± 0.004	0.24 ± 0.002	0.21 ± 0.002	0.19 ± 0.004	0.18 ± 0.010	0.22 ± 0.081
ML	σ, z	0.24 ± 0.003	0.20 ± 0.002	0.18 ± 0.002	0.16 ± 0.003	0.16 ± 0.009	0.19 ± 0.068
	σ, N_{gal}	0.19 ± 0.003	0.14 ± 0.001	0.10 ± 0.001	0.08 ± 0.002	0.07 ± 0.004	0.10 ± 0.037
	σ, z, N_{gal}	0.17 ± 0.002	0.13 ± 0.001	0.10 ± 0.001	0.07 ± 0.001	0.07 ± 0.004	0.11 ± 0.039
Targeted Observations							
Power Law		0.43 ± 0.006	0.39 ± 0.004	0.33 ± 0.004	0.27 ± 0.005	0.18 ± 0.010	0.11 ± 0.039
Prob	σ	0.24 ± 0.003	0.25 ± 0.002	0.25 ± 0.003	0.22 ± 0.004	0.19 ± 0.011	0.30 ± 0.110
	σ, z	0.24 ± 0.003	0.24 ± 0.002	0.23 ± 0.002	0.56 ± 0.011	0.21 ± 0.012	0.36 ± 0.131
	σ, z, N_{gal}	0.20 ± 0.003	0.19 ± 0.002	0.17 ± 0.002	0.67 ± 0.013
	σ	0.30 ± 0.004	0.32 ± 0.003	0.32 ± 0.003	0.30 ± 0.006	0.29 ± 0.016	0.13 ± 0.049
ML	σ, z	0.26 ± 0.004	0.25 ± 0.002	0.24 ± 0.003	0.23 ± 0.004	0.27 ± 0.015	0.16 ± 0.057
	σ, N_{gal}	0.27 ± 0.004	0.27 ± 0.003	0.27 ± 0.003	0.25 ± 0.005	0.18 ± 0.010	0.15 ± 0.053
	σ, z, N_{gal}	0.21 ± 0.003	0.18 ± 0.002	0.16 ± 0.002	0.14 ± 0.003	0.12 ± 0.007	0.15 ± 0.054

Table 2.2 Continued

Method	Bins – Log M_{pred}					
	12.5 – 13	13 – 13.5	13.5 – 14	14 – 14.5	14.5 – 15	15 – 15.5
Survey Observations						
Power Law	0.40 ± 0.050	0.41 ± 0.016	0.38 ± 0.010	0.32 ± 0.010	0.25 ± 0.016	0.15 ± 0.056
Prob	σ	0.11 ± 0.024	0.18 ± 0.008	0.22 ± 0.006	0.22 ± 0.007	0.19 ± 0.012
	σ, z	0.13 ± 0.028	0.19 ± 0.008	0.22 ± 0.006	0.21 ± 0.007	1.31 ± 0.084
	σ, z, N_{gal}	0.14 ± 0.030	0.18 ± 0.008	0.19 ± 0.005	0.19 ± 0.006	...
ML	σ	0.27 ± 0.034	0.27 ± 0.011	0.31 ± 0.008	0.30 ± 0.009	0.30 ± 0.019
	σ, z	0.20 ± 0.025	0.24 ± 0.009	0.24 ± 0.006	0.25 ± 0.008	0.24 ± 0.015
	σ, N_{gal}	0.25 ± 0.032	0.23 ± 0.009	0.27 ± 0.007	0.26 ± 0.008	0.27 ± 0.018
	σ, z, N_{gal}	0.17 ± 0.021	0.21 ± 0.008	0.20 ± 0.005	0.19 ± 0.006	0.17 ± 0.011
						0.20 ± 0.071

A few caveats apply to the numbers given in Table 2.1 and Table 2.2. While we provide corrections for cluster masses above $10^{15} M_{\odot}$, they are estimated from only a handful of objects, and do not constitute a representative sample of clusters. This becomes particularly apparent for the probability methods with many features. As the number of observed features increases, the number of training clusters in any particular bin decreases. This leads to highly skewed biases and scatters for the high mass clusters and probability methods. We do not report any bin where such small number statistics dominate in Tables 2.1 and 2.2. On the opposite end of the cluster mass spectrum, there are very few, if any, clusters detected with Targeted or Survey observations below $5 \times 10^{12} M_{\odot}$. Therefore, while we show these points in Figures 2.5 and 2.6, we exclude their biases and scatters from Tables 2.1 and 2.2 for the same reasons.

The method which produce the lowest scatter and bias depends on the mass of the cluster in question and the type of observations used. For the Targeted observations, the power law method outperforms all other methods, in terms of bias and scatter, for the highest mass clusters. But outside of the two highest mass bins, the $ML_{\sigma,z,N_{gal}}$ method shows the smallest amount of scatter and bias most consistently. With Survey observations, the power law again provides the lowest bias in the highest cluster mass bins, but is outperformed in terms of scatter by the other two methods. The $ML_{\sigma,z,N_{gal}}$ method shows the smallest amount of scatter and bias most consistently across the cluster mass range in question.

2.4.3 Impact of Training Sample Cosmology

All simulations (including that used for Buzzard) use specific values for cosmological parameters. When using simulation data to train ML methods, we incorporate all of those assumptions into the learned feature associations. One could imagine that

the specific values of the cosmological parameters in the training sample could bias the ML results when applied to data (real or simulated) created from an unknown true set of cosmological parameters.

To test for this, we used the Millennium simulation as an alternative data set. The Millennium simulation uses a set of cosmological parameters that are substantially different from Buzzard. The Millennium simulation adopts a flat cosmological model based of the values derived from the Two-degree Field Galaxy Redshift Survey (Colless et al., 2001) and the first year data of the *Wilkinson Microwave Anisotropy Probe* (WMAP; Spergel et al. 2003): $\Omega_\Lambda = 0.75$, $\Omega_M = 0.25$, $\sigma_8 = 0.9$, $n_s = 1$ and $H_0 = 73 \text{ km s}^{-1}\text{Mpc}^{-1}$. The clusters in Millennium provide a testing sample to understand how a training sample derived from Buzzard will impact the mass recovery on a wholly new dataset.

We repeat our analysis using cluster halo and galaxy catalogs from the Millennium simulation (Springel et al., 2005) obtained via querying the Millennium online database[‡] (Lemson & The Virgo Consortium, 2006). The Millennium simulation tracks 2160^3 dark matter particles of $8.6 \times 10^8 h^{-1} M_\odot$ inside a comoving $500 (h^{-1}\text{Mpc})^3$ box from $z = 127$ to 0. The following SQL query selects the cluster halos:

```
SELECT *
FROM mfield..fof
WHERE snapnum IN (SELECT snapnum
    FROM snapshots..mr
    WHERE z BETWEEN 0.01 AND 0.5)
    AND m_crit200 > 100
    AND random BETWEEN 0 AND 10000
```

To select the corresponding galaxies, we use:

```
SELECT sh.fofid ,
    sh.subhaloid ,
```

[‡]<http://gavo.mpa-garching.mpg.de/Millennium/>

```

g . galaxyid ,
g . x ,
g . y ,
g . z ,
g . redshift ,
g . velx ,
g . vely ,
g . velz ,
sdss . g_sdss ,
sdss . r_sdss ,
sdss . i_sdss
FROM mfield .. fofsubhalo AS sh
INNER JOIN mpagalaxies .. delucia2006a AS g
    ON sh . subhaloid = g . subhaloid
INNER JOIN mpagalaxies .. delucia2006a_sdss2mass AS sdss
    ON g . galaxyid = sdss . galaxyid
WHERE sh . fofid IN (SELECT fofid
    FROM mfield .. fof
    WHERE snapnum IN (SELECT snapnum
        FROM snapshots .. mr
        WHERE z BETWEEN 0.01 AND 0.5)
    AND m_crit200 > 1000
    AND random BETWEEN 0 AND 10000)

```

We select 4,806 clusters, comprised of 623,663 galaxies, at $0.02 < z < 0.5$ and $M > 10^{13} \text{ M}_\odot$, and apply the same data processing as with the Buzzard galaxies. We begin by assigning each galaxy an [O II] flux value (see Section 2.2.2), and “observe” each galaxy using realistic (see Section 2.2.4) observational limits. After recovering 3750 clusters which have at least five galaxies observed, we calculate the LOSVD of each cluster as in Section 2.3.2.

We conduct our test in two ways. Both use the ML methods (see Section 2.3.3.4) to predict the cluster masses of the Millennium clusters, but each test uses a different training set. First, we use the full set of clusters detected in the Buzzard catalogs (14,000 clusters with $M > 10^{11} \text{ M}_\odot$) to train the ML. Second, the Millennium clusters are split into training-testing samples. This provides a test case where we have

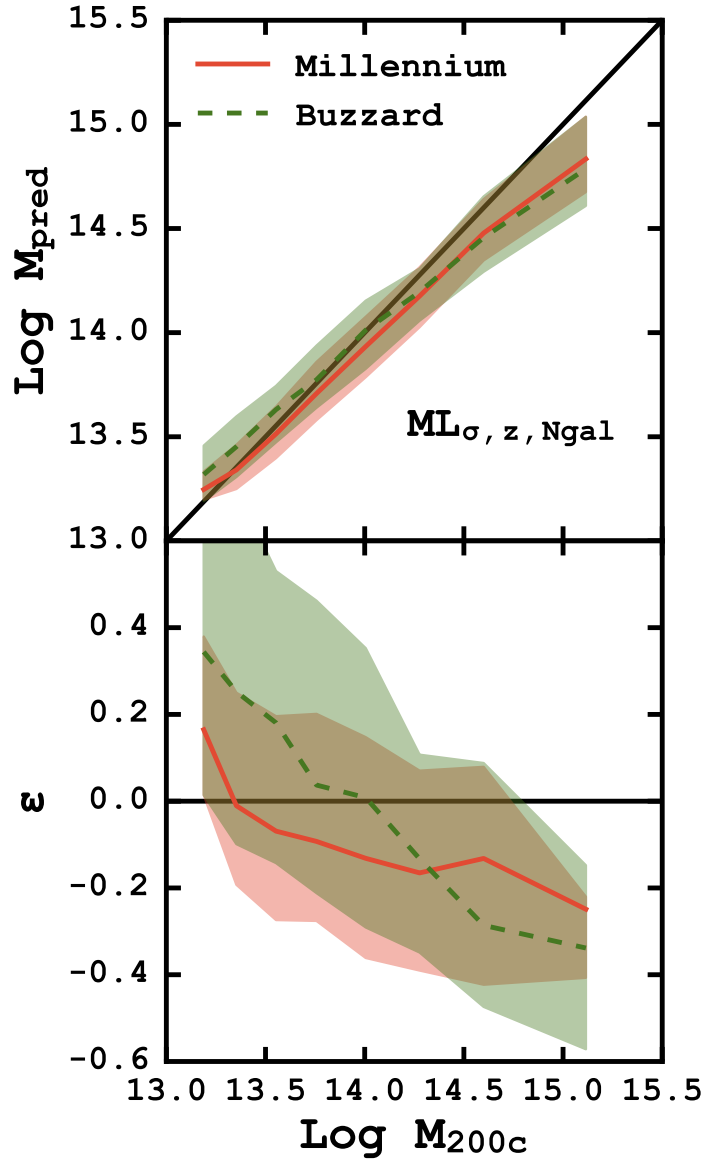


Figure 2.7: *Top:* ML based cluster mass predictions for the Millennium simulation clusters where the ML method has been trained with either a subset of the Millennium clusters (solid line) or the Buzzard catalog (dashed line). The shaded areas show the 68% scatter around the median. The solid black line shows the 1:1 relation. *Bottom:* The fractional error (Equation 2.12) also as a function of true cluster mass. The similarity of the predictions with the different training sets demonstrates how the ML method is not sensitive to the underlying cosmological assumptions.

different cosmological choices between the training and testing samples, and the same cosmological assumptions in both samples.

The top panel of Figure 2.7 shows the ML predicted cluster masses for the ~ 4000 Millennium clusters as a function of true cluster mass. The orange (Millennium) and green (Buzzard) colors indicate the two different training samples. The median (solid and dashed lines) predicted cluster masses show similar trends regardless of the training data set used. The bottom panel of Figure 2.7 shows the fraction error (Equation 2.12) also as a function of true cluster mass. The large amount of scatter (the shaded area) in the fractional error for the Buzzard-trained predictions is due to the training set including clusters with masses below the $M = 10^{13} \text{ M}_\odot$ threshold for the Millennium clusters. This allows the ML method to predict masses which can be significantly different, whereas the Millennium training set does not include $M < 10^{13} \text{ M}_\odot$ clusters, which reduces the scatter of the predicted masses.

Based on these tests, we do not find a significant cause for concern with using trained ML methods to predict our galaxy cluster masses when the underlying cosmological choices are different. This highlights the versatility of our chosen ML method. The ML method could be further diversified by including cluster measurements from a wide range of cosmological simulations (or observations) which, in affect, marginalizes over all the cosmological assumptions further reducing the dependence.

2.5 HETDEX as a Galaxy Cluster Survey at $z < 0.5$

2.5.1 Constraints on Cosmological Parameters

Galaxy clusters trace the peaks in the universal matter density, often referred to as the power spectrum of matter density fluctuations or the matter power spectrum. This enables them to be sensitive probes of Ω_m , the total mass ($\Omega_b + \Omega_c$) density,

and $\sigma_8 h^{-1}$, the normalization of the power spectrum. We constrain these parameters by the comparison of the number density of observed clusters to that predicted in cosmological models. Although, in reality, one measures $\sigma_8 h^{-1} \Omega_m^q$, where the value of q depends on the masses and redshifts of the halos considered.

To get a sense of how well HETDEX will be able to constrain cosmological parameters we follow the discussion of [Weinberg et al. \(2013\)](#) (hereafter [W13](#)), and begin with a few simplifying assumptions. While sensitive to Ω_m , the number density of clusters does not necessarily provide the strongest constraint, but combined with other data sets (e.g., CMB, BAO, supernovae, WL, etc.) it will constrain Ω_m to higher precision.

To estimate the error associated with a measurement of $\sigma_8 h^{-1}$ (which [W13](#) refer to as $\sigma_{11,abs}$), [W13](#) consider two sources of uncertainty, the systematic uncertainties in cluster mass calibration and the statistical uncertainty in the observed number density of clusters. The authors combine these two uncertainties though (their Eq. 141):

$$\Delta \ln \sigma_8 h^{-1}(z) \approx q(z) \times \max [\Delta \ln M, \alpha(z)^{-1} \Delta \ln N]. \quad (2.13)$$

where q is the degeneracy exponent between $\sigma_8 h^{-1}$ and Ω_m , $\Delta \ln M$ is the mass scale uncertainty, $\Delta \ln N$ is the cluster statistical uncertainty, and α is slope of the cumulative HMF. Using the [Tinker et al. \(2008\)](#) HMF at $z \sim 0.2$ and a limiting cluster mass of $10^{14} M_\odot$, [W13](#) estimate $q \sim 0.4$, $\alpha \sim 3$, and find that any cluster survey with more than 10-20 clusters is dominated by the uncertainty in the overall mass scale.

For a survey such as HETDEX, we can estimate the constraints on $\sigma_8 h^{-1}$ using Equation 2.13. If we consider clusters with masses above $10^{14} M_\odot$ and with Perfect knowledge observations, the lowest mass scale uncertainty (given in Table 2.2) is

$\Delta_{\log_{10}} M \sim 0.075$ dex or about 20%. This gives a uncertainty on $\sigma_8 h^{-1}$ of 7%. For clusters above $10^{14} M_\odot$, Survey observations constrain the masses to about 51% which, in turn, constrains $\sigma_8 h^{-1}$ to 20%.

Because of the simplifying assumptions, and the superior quality of the data (no contamination, signal-to-noise issues, etc.), realistic expectations for HETDEX is to directly constrain $\sigma_8 h^{-1}$ is not yet competitive with other methods (e.g., CMB, WL, X-ray). For example, [de Haan et al. \(2016\)](#) constrain $\sigma_8 h^{-1}$ to $\sim 5\%$ using a sample of 337 SZE detected clusters from the SPT-SZE survey. For the ~ 1500 clusters detected with Survey observations to constrain $\sigma_8 h^{-1}$ and to be dominated by cluster statistics alone ($\Delta \ln N \sim N^{-1/2}$), the absolute cluster calibration would need to be better than 2.5%. For a fully Targeted survey, about 14,000 clusters, this cluster mass calibration uncertainty reduces to $> 1\%$. So while, the constraints produced by HETDEX will be larger than some other studies, the type of data provided by HETDEX will enable an independent calibration from other cluster mass measurements. This will provide important systematics checks on other studies and will ultimately improve the measurements of $\sigma_8 h^{-1}$.

2.5.2 Scale and Scatter of the Richness-Cluster Mass Relation

Large-scale optical surveys (e.g., DES and LSST) expect to detect hundreds of thousands of galaxy clusters at $z < 1$. Because they produce photometry only, a major challenge for these surveys is relating a cluster observable to the total DM mass. One promising cluster mass estimator is the optical richness (e.g., [Abell 1958](#)). Specifically, here, we use λ , the weighted number of galaxies within a scale aperture (e.g., [Rozo et al. 2011](#)) as calculated by the redMaPPer algorithm ([Rykoff et al., 2012](#)). Previous works (e.g., [Rozo et al. 2010](#)) show that the richness correlates strongly with cluster mass on the average, but the absolute mass scale of the optical

richness mass estimator and the scatter in cluster mass at fixed optical richness are imprecisely known (Rykoff et al., 2012). These systematics remain the major source of uncertainty in deriving cosmological constraints from cluster abundances and must be measured using independent methods to realize the full potential of these types of surveys.

One of the main goals of this study is to understand how well HETDEX will be able to measure the scatter in the richness-mass relationship. To this end, we choose to impose a richness-mass relation onto the clusters in the Buzzard catalogs. The true richness-mass relation could depend strongly on the number and types of environmental effects, because such effects have a strong impact on the number and types of galaxies observed in clusters (e.g., Gunn & Gott, J. Richard 1972; Balogh et al. 2000; White et al. 2010). Any environmental effects included in Buzzard could potentially impact our observed richness. The imposition of an empirical richness-mass relation ensures the richness values correspond correctly to the clusters in our sample, could provide direct observational tests in the future.

We generate richnesses based on the true cluster masses, and for testing, we assume two versions of the richness-mass relationship. Farahi et al. (2016) base the relation on stacked velocity dispersions, and Simet et al. (2016) use weak lensing measurements to construct their relation. Because we are investigating HETDEX’s ability to recover the overall cluster mass scale and underlying scatter in the mass-richness relationship, we use the true cluster masses perturbed by a known amount to estimate the observed richness.

To confirm that measuring the underlying scatter is possible, after generating richness values we calculate the scatter of the cluster masses at fixed λ , $\sigma_{M|\lambda}$, by comparing the true, unperturbed cluster masses against the richness. We do recover the expected scatter, often, to well within 0.01 dex. We repeat the process with

both assumed richness-mass relationships and recover the expected scatter in both instances.

We use the lambda values generated above in combination with the $M_{\sigma,z,N_{gal}}$ predicted cluster mass which have been bias corrected using the values in Table 2.1 and denoted $M_{\text{pred,corr}}$. The use of biased cluster mass predictions inhibits our ability to accurately recover any scatter in richness-mass relationship, and is discussed further below.

Primarily, we are interested in the intrinsic scatter of the richness-mass relationship. This is because HETDEX is uniquely situated to estimate the scatter, whereas studies relying on stacked data (e.g., Farahi et al. 2016; Simet et al. 2016) lose that information. We begin by attempting to constrain the absolute mass scale, and as part of our fitting process, we estimate the overall scatter in the relationship. In order to understand how HETDEX will constrain the absolute mass scale, we find the best fitting relation to our richness-mass data. To generate the best fitting lines, we follow the general procedure of Hogg et al. (2010), by defining an objective function and then minimizing the loss. Our objective function is

$$P(y_i|x_i, \sigma_{y_i}, m, b, \sigma) = \frac{1}{\sqrt{2\pi(\sigma_{y_i}^2 + \sigma^2)}} \exp\left(-\frac{[y_i - m x_i - b]^2}{2(\sigma_{y_i}^2 + \sigma^2)}\right) \quad (2.14)$$

where y_i is the observed cluster mass, x_i is the observed richness, σ_{y_i} is the uncertainty in observed cluster mass, m is the power law slope, b is the overall cluster mass scale, and σ is the intrinsic scatter between richness and cluster mass. We assume that the intrinsic scatter is constant from point to point and that all of the measurement errors are Gaussian. We convert this objective function into a likelihood by taking

the product of all the individual probabilities:

$$\mathcal{L} = \prod_{i=1}^N P(y_i|x_i, \sigma_{y_i}, m, b, \sigma). \quad (2.15)$$

We again rely on MCMC samples to sample the posterior probability distribution and thus maximize the likelihood. The best fitting slope and intercept are quoted as the median value of the posterior probability distribution with 68% error bars defined as the square root of the second moment of the same distribution.

We limit our clusters to those with $10 \leq \lambda < 130$ in our fitting analysis because above $\lambda = 130$ there are too few clusters and number-counting errors dominate. Other observational studies (e.g., [Saro et al. 2015](#)) which have lower limits on λ , so we exclude anything less than $\lambda = 10$. For a richness-mass relation with an intrinsic scatter of $\langle \sigma_{M|\lambda} \rangle = 0.25$ dex, we find a best-fitting relation for the Targeted observations as

$$\text{Log } M_{200c}/\text{M}_\odot = 12.46 \pm 0.02 + 1.07 \pm 0.02 \text{ Log } \lambda \quad (2.16)$$

and the Survey observations as

$$\text{Log } M_{200c}/\text{M}_\odot = 12.64 \pm 0.05 + 0.98 \pm 0.03 \text{ Log } \lambda \quad (2.17)$$

This gives $M_{200c} = (1.45 \pm 0.12) \times 10^{14}$ M_\odot and $M_{200c} = (1.59 \pm 0.27) \times 10^{14}$ M_\odot at $\lambda = 40$ for the Targeted and Survey observations respectively. In both cases, this normalization differs significantly from the $M_{200c} \approx 2.1 \times 10^{14} h^{-1}$ M_\odot found in recent work [Li et al. \(2016\)](#); [Simet et al. \(2016\)](#). If the intrinsic scatter is reduced to ~ 0.05 dex we recover an overall normalization of $M_{200c} = (2.14 \pm 0.12) \times 10^{14}$ M_\odot and $M_{200c} = (2.10 \pm 0.26) \times 10^{14}$ for the Targeted and Survey observations at $\lambda = 40$.

We also estimate the intrinsic scatter. For observations with a richness-mass relation intrinsic scatter of $\langle \sigma_{M|\lambda} \rangle = 0.25$ dex, we recover $\langle \sigma_{M|\lambda} \rangle = 0.236 \pm 0.003$ dex and $\langle \sigma_{M|\lambda} \rangle = 0.257 \pm 0.007$ dex for the Targeted and Survey observations respectively.

Figure 2.8 summarizes the main results of this investigation. The top panel shows the generated optical richness, λ , versus the predicted cluster mass. The cluster masses are the $ML_{\sigma,z,N_{gal}}$ based and correspond to the Targeted and Survey observation strategies. The bottom panel of Figure 2.8 shows the scatter in the predicted cluster masses at fixed richness, $\sigma_{M|\lambda}$. The solid line represents the intrinsic amount of scatter added to the masses. The cluster masses are binned in increasing ten richness intervals (10 – 20, 20 – 30, etc.). The inset upper panel shows the intrinsic scatter versus the recovered average scatter at fixed richness, $\langle \sigma_{M|\lambda} \rangle$ and illustrates how well the two observation strategies recover the intrinsic scatter.

We find that we are able to accurately recover an average intrinsic scatter of $0.2 < \langle \sigma_{M|\lambda} \rangle < 0.3$ dex, finding $\langle \sigma_{M|\lambda} \rangle = 0.257 \pm 0.007$ at $\sigma_{true} = 0.25$ with Survey observations. This is very promising as other observational studies have estimated the intrinsic scatter of real clusters to be ~ 0.25 dex (e.g., Rozo & Rykoff 2014; Rozo et al. 2015). As the intrinsic scatter increases or decreases, we fail to recover the scatter as accurately.

For the richness range $10 \leq \lambda < 130$ the intrinsic scatter in between the $M_{pred,corr}$ predicted cluster masses and the true cluster mass (the basis of our richnesses) is ~ 0.15 dex for Targeted observations and ~ 0.20 dex for Survey observations. This forms an effective floor on the amount of scatter we are able to recover from our fitting process. As we reduce the overall scatter in our cluster mass recovery, this floor will lower. We underestimate the scatter in high intrinsic scatter relations because any residual bias remaining in the predicted clusters masses after correction reduces the observed scatter. Because the bias subtraction when creating $M_{pred,corr}$ subtracts the

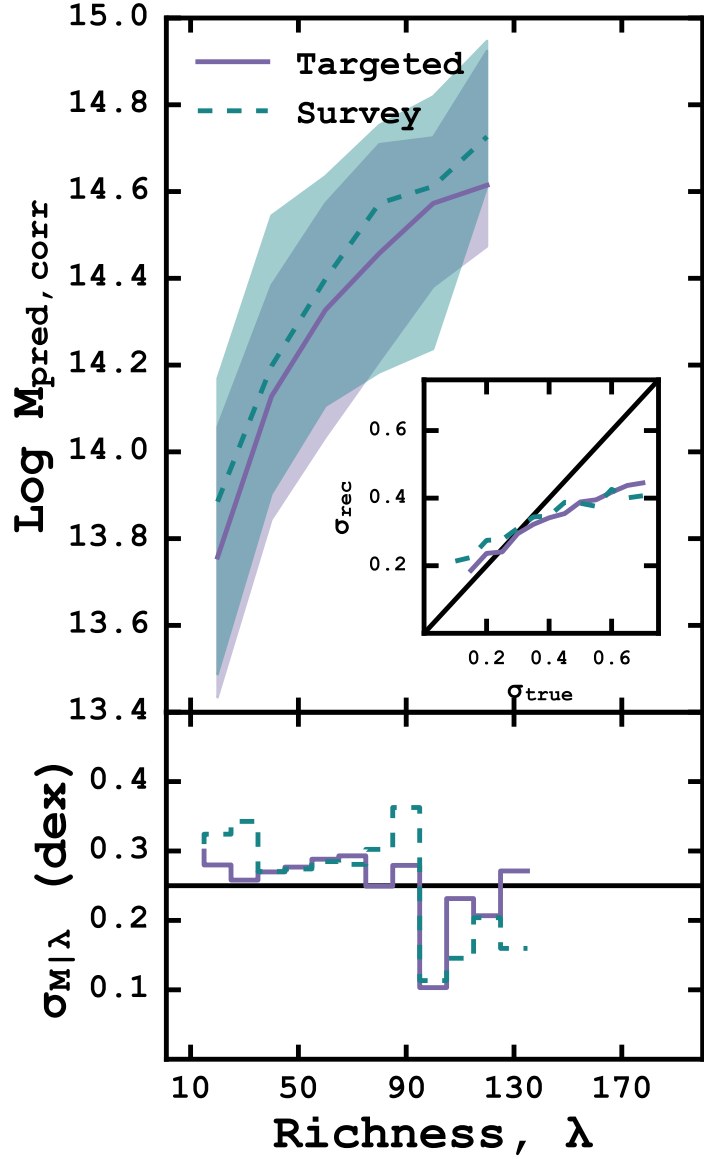


Figure 2.8: *Top:* The optical richness, λ , versus the corrected predicted cluster mass. The solid, purple line is the median predicted mass for the Targeted observing, and the turquoise, dashed line is the median recovered mass for the HETDEX-like observations. The shaded regions represent the 68% scatter around the median values. *Bottom:* The scatter in the relation at fixed richness. The solid black line shows the intrinsic scatter of $\sigma_{true} = 0.25$ dex. Color coding is the same as the top panel. *Inset:* The evolution of the intrinsic scatter versus the average recovered scatter, σ_{rec} .

mean bias, we are left with a small amount of residual bias, lowering the measured scatter for high scatter relationships.

3. A PILOT SURVEY TO MEASURE CLUSTER DYNAMICS: TARGETED OBSERVATIONS WITH THE VIRUS PROTOTYPE INSTRUMENT

3.1 Introduction

Many large area-sky surveys both currently underway and upcoming are prioritizing the identification of clusters for both detailed studies of cosmology and for fundamental physical examinations of galaxy properties in rich environments. At present, the greatest number of clusters are being identified using large millimeter wave surveys with the South Pole Telescope (SPT; [Carlstrom et al. 2011](#)) or the Atacama Cosmology Telescope (ACT; [Swetz et al. 2011](#)). These observations rely on the Sunyaev-Zel'dovich effect (SZE; [Sunyaev & Zeldovich 1972](#)) which uses the up-scattering of cosmic microwave background (CMB) photons to both identify the cluster and to estimate its mass. X-ray surveys of cluster (e.g., [Mehrtens et al. 2012](#)) continue to play an important role, which will continue to increase as future large-area X-ray surveys (e.g., *EROSITA* [Merloni et al. 2012](#)) become available. However, deep, wide field optical surveys, such as the Dark Energy Survey (DES; [The Dark Energy Survey Collaboration 2005](#)) and planned Large Synoptic Survey Telescope (LSST; [LSST Dark Energy Science Collaboration 2012](#)) will discover many more clusters at increasing lower mass in the near future; at its completion, DES is expected to identify approximately 100,000 clusters at $z < 1$ ([Dark Energy Survey Collaboration et al., 2016](#)), of which about 1000 clusters with SZE and X-ray observations currently overlap with DES identified clusters. Such surveys will employ the richness of the individual clusters as a cluster mass proxy, and as such, will rely on follow-up observations to better constrain the absolute scale and the scatter in the richness-mass relation. But, as the number of clusters grows to many tens of

thousands, individual spectroscopic confirmation becomes unfeasible. Therefore, we rely on well calibrated observable-mass relationships to estimate the masses of the observed clusters.

Unfortunately, mass is not directly observable, so we must estimate it through another discernible cluster property. Observed X-ray temperatures and luminosities correlate tightly with a cluster’s dynamical mass (e.g., Mantz et al. 2010; Rykoff et al. 2014), especially for dynamically relaxed clusters (e.g., Mantz et al. 2015). Observations of the SZE provide accurate estimations of mass (e.g., Vanderlinde et al. 2010; Sehgal et al. 2011), but can be effected by the physics of the intracluster medium (e.g., Pipino & Pierpaoli 2010) and the ability to detect low mass galaxy clusters is currently limited by technology (e.g., Carlstrom et al. 2002). The richness (e.g., Abell 1958; Rykoff et al. 2012) is, at present, defined to be the weighted number of cluster member galaxies with a scale aperture. It has been shown to correlate strongly with cluster mass in the mean (e.g., Rozo et al. 2010), providing a powerful cluster mass estimate based on photometry alone.

The richness is already being used in many optical studies (e.g., Ruel et al. 2014; Sifón et al. 2015), but the absolute mass scale and more importantly the intrinsic scatter in the relation are currently under active investigation (e.g., Rozo et al. 2015; Saro et al. 2015; Baxter et al. 2016; Farahi et al. 2016; Simet et al. 2016). These systematics remain the major source of uncertainty in deriving cosmological constraints from cluster abundances and testing structure growth in a Λ CDM universe. To realize fully the promise of the large samples from DES and LSST, we must measure both the absolute mass scale and scatter in the optical-richness mass estimator using independent methods.

The Hobby Eberly Dark Energy Experiment (HETDEX; Hill et al. 2008b) is a forthcoming blind spectroscopic survey that offers the ability to calibrate accurately

the optical richness-mass relation for a significant number of galaxy clusters at both extremes of the mass scale. At present, because HETDEX is designed to measure the dark energy equation of state at $z \sim 0.2$, and the applicability to galaxy cluster science has not yet been investigated. We began this investigation in Chapter 2. The blind spectroscopic observations of HETDEX are capable of accurately estimating galaxy cluster masses over the range of redshifts and cluster masses covered by the study. Using a machine learning approach where several cluster observables are combined, we estimate cluster masses to a similar level of precision as a fully targeted survey. The ability of HETDEX to further constrain optically derived masses is of paramount importance to upcoming large photometric surveys. This study provides insight into how well a HETDEX type survey will constrain mass estimations and cosmological parameters in the future.

In this chapter, we present a pilot study of ten massive galaxy clusters using integral field spectroscopy with the Mitchell Spectrograph as a pilot program for HETDEX. The goal of this study is to obtain spectroscopic redshifts of the individual cluster galaxies, determine the velocity dispersion and to infer each cluster's dynamical mass. This allows us to compare the inferred mass with other mass estimators (e.g., the clusters in this sample have deep *Chandra* or *XMM-Newton* X-ray data, and richness measurements) with the aim of better characterizing the scatter in the richness-mass relation, $\sigma_{M|\lambda}$.

The layout of this chapter is the following. In Section 3.2 we discuss the target selection and the setup of the Mitchell Spectrograph used to conduct the observations. Section 3.3 describes the methods and tools used to reduce the observations. We present our redshift catalog, cluster members and cluster dynamical properties in Section 3.4. We discuss a machine learning based alternative to a traditional power law estimate of cluster mass in Section 3.5.2 In Section 3.6, we compare and discuss

the different mass estimations and remark on the applicability of these methods for the study of the optical richness-cluster mass relationship. Finally, we summarize this work in Section 4.1.

Throughout this chapter, we adopt the following cosmological model from the Buzzard simulations (see Section 3.5.2): $\Omega_\Lambda = 0.714$, $\Omega_M = 0.286$, and $H_0 = 70 \text{ km s}^{-1}\text{Mpc}^{-1}$, assume a Chabrier initial mass function (IMF; Chabrier 2003), and use AB magnitudes (Oke, 1974).

3.2 Design

3.2.1 Target Selection

We select clusters at $z = 0.2 - 0.3$ using two different methods and for two different purposes. We optically select eight of the ten clusters from Rykoff et al. (2012) using the *Sloan Digital Sky Survey* (SDSS; Blanton et al. 2001) Data Release 8. These clusters have high ($\lambda > 70$) observed richesses which corresponds to $M > 2.2 \times 10^{14} \text{ M}_\odot$, and are a combination of relaxed and unrelaxed systems. The last two clusters are selected from the *XMM Cluster Survey* (XCS; Mehrtens et al. 2012) and correspond to individually measured X-ray temperatures of $T_X < 2.5 \text{ keV}$. Such X-ray temperatures have inferred masses of $10^{14} \text{ M}_\odot > M_{DM} > 5 \times 10^{13} \text{ M}_\odot$.

The optically selected clusters have many more members, by up to a factor of 8, (see Table 3.1) than the X-ray selected clusters which allows us to investigate the accuracy of our mass recovery methods at both cluster and group scales. See Table 3.1 for individual cluster sky positions and associated parameters.

Table 3.1: Basic properties of the ten galaxy clusters targeted with the MS: Column 1: Our internal cluster name; Column 2: Abell Catalog ID; Column 3: The right ascension of the cluster; Column 4: The declination of the cluster; Column 5: the nominal (often photometric) cluster redshift; Column 6: The measured richness; Column 7: The date of our observations.

Cluster (1)	Abell ID (2)	RA (J2000) (3)	DEC (J2000) (4)	z (5)	λ (6)	Obs. Date (7)
MSJ010455.4+000336.3	...	01:04:55.369	+00:03:36.28	0.277	129.7 ± 4.9	August, 2012
MSJ133520.1+410004.1	Abell 1763	13:35:20.092	+41:00:04.12	0.223	191.0 ± 5.7	May, 2012
MSJ140102.0+025242.6	Abell 1835	14:01:01.965	+02:52:42.63	0.252	135.6 ± 5.2	May, 2012
MSJ153656.3+242431.6	...	15:36:56.253	+24:24:31.60	0.226	70.1 ± 4.4	May, 2012
MSJ164019.8+464241.5	Abell 2219	16:40:19.812	+46:42:41.51	0.225	202.6 ± 5.4	May, 2012
MSJ172227.2+320757.2	Abell 2261	17:22:27.182	+32:07:57.24	0.224	185.8 ± 7.4	May, 2012
MSJ211849.1+003337.3	...	21:18:49.069	+00:33:37.33	0.270	121.0 ± 4.6	August, 2012
MSJ215422.9+003723.5	Abell 2392	21:54:22.936	+00:37:23.48	0.223	87.2 ± 4.8	August, 2012
XMMXCSJ124425.9+164758.0	...	12:44:25.203	+16:47:48.00	0.235	11.4 ± 1.7	May, 2013
XMMXCSJ125650.2+254803.2	...	12:56:49.999	+25:48:02.99	0.280	8.2 ± 1.8	May, 2013

3.2.2 Observations

We use the Mitchell Spectrograph (MS; formerly known as VIRUS-P; [Hill et al. 2008a](#)) an integral field unit (IFU) in a square array of 246 $4''.24$ diameter optical fibers. This provides a $1'.7 \times 1'.7$ field-of-view (FOV) with a 1/3 filling factor. A Fairchild Instruments, $2k \times 2k$ charge couple device (CCD) images the spectra from each of the 246 fibers. The spectra have approximately a gaussian profile with a 5 pixel full width at half maximum (FWHM), and each are separated by 8 pixels to minimize the amount of cross-talk between the fibers.

There are two spectral configurations available on MS, a blue setup, $3600\text{--}5800 \text{ \AA}$ and a red setup, $4600\text{--}6800 \text{ \AA}$. In addition, there are four volume phase holographic gratings available to disperse the light. For the purpose of this work, the lowest resolution, $\sim 5 \text{ \AA}$, grating is used. At the native pixel scale, this translates into a spectral dispersion of $\sim 1.11 \text{ \AA pixel}^{-1}$.

We use MS to target the galaxy clusters using the 5 \AA grating covering a wavelength range of $4400 - 6600 \text{ \AA}$. With this instrumental setup and for galaxies $z = 0.2 - 0.3$, we will cover the Ca H&K, Fe I ($\lambda 4383$), H- δ , H- γ and H- β absorption features. Additionally, we cover emission of the [O II] ($\lambda\lambda 3727, 3729$) doublet, H- β , and [O III] ($\lambda\lambda 4960, 5008$), which allows for the identification of actively star-forming galaxies.

The FOV of the MS corresponds to an approximately 0.4 Mpc square region at $z = 0.2 - 0.3$. To ensure adequate coverage of the cluster out to a radius of 0.5 Mpc , we use four MS pointings per cluster. Figure 3.1 shows an example of the pointing pattern done on each cluster. The entire field is centered on the brightest cluster galaxy (BCG) and the individual tiles are shifted away. Furthermore, each of the four tiles are dithered at relative positions $(\Delta\alpha, \Delta\delta) = (0''.0, 0''.0)$, $(-3''.6, -2''.0)$, and

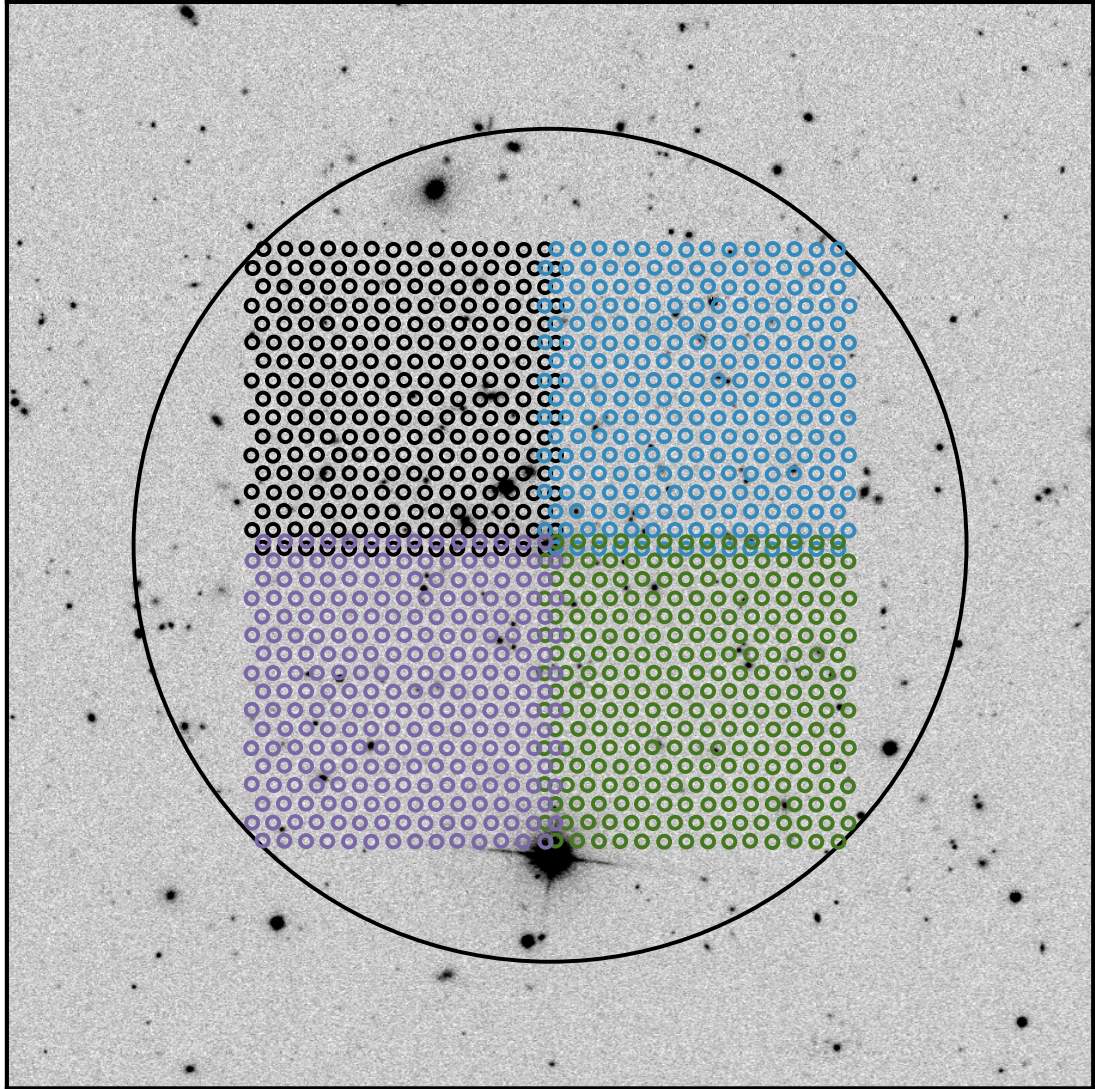


Figure 3.1: SDSS r-band image of an optically selected galaxy cluster Abell 2631 ($z = 0.273$) selected from the SDSS DR8 data, and centered on the BCG. The large black circle shows the region $R < 0.5$ Mpc ($r < 2/3$). The northeast (NE), northwest (NW), southwest (SW), and southeast (SE) fields with the fiber positions are shown in black, blue, green and purple respectively, illustrating how we survey each cluster. Nearly all galaxies within this region are associated with the cluster.

$(0''.0, -4''.0)$ from the origin to ensure full coverage of the FOV. Therefore, there are 736 individual spectra for each of the four fields or 2952 measurements for the cluster as a whole.

We have set exposure times to achieve spectra with signal-to-noise ratios (SNRs) ~ 3 per spectral element (averaged over 4.6 pixels) in the continuum for objects with $g = 21.3$ mag (which corresponds to approximately $0.2L^*$ for cluster galaxies at $z = 0.2$) in 3600 seconds per pointing.. We base the expected SNR on the experience of [Shetrone et al. \(2010\)](#), who achieves $\text{SNR} = 100$ per pixel in the continuum for point sources with $B = 16.5$ mag at 4000 \AA in 4800 seconds. Therefore, we require $1 \text{ hr/pointing} \times 4 \text{ pointings} = 4 \text{ hrs on sky per cluster}$. Even though the field is dense with galaxies, there is sufficient “blank” area to allow for enough “sky” fibers for background subtraction.

3.3 Data Reduction

All data are reduced using P3D* ([Sandin et al., 2010](#)) a general-use IFU reduction pipeline. The first step is to min/max-filtered average combine a minimum of 20 bias images from each night into a master-bias image, which is subtracted from each other image from the same night. Secondly, a trace mask is created from flat-fielding on the dusk or dawn sky. The fibers are fairly densely packed, so to determine the position of each spectrum in the dispersion direction each spectrum is extracted using a multi-profile deconvolution approach ([Sharp & Birchall, 2010](#)) to account for cross talk between fibers. Third, a dispersion mask for the wavelength calibration from images of Hg+Cd (for the May, 2012 observations) or Cd+Ne (for all other observations) arc lamps. The residuals between the derived wavelength solution and the known wavelengths of the emission lines is calculated from a fifth order polynomial and

*<http://p3d.sourceforge.net/>

lie between $0.02 - 0.06 \text{ \AA}$. Finally, a fiber flat is created from the sky flats by a min/max-filtered average combine as in step one.

We extracted the science spectra using several steps. First, we subtract the bias frames from each science frame. Next, we use PyCOSMIC ([Husemann et al., 2012](#)), integrated into P3D with the default parameters, to clean cosmic ray hits. Third, we use the previously created dispersion mask to wavelength calibrate the extracted spectra. Aligning the dispersion mask to bright telluric lines (namely [O I] at 5577 \AA) accounts for any flexure in the instrument between the images of the arc lamps and science frames. Finally, we normalize the extracted spectra using the transmission in the fiber flats from above.

The result of this process is row-stacked spectra and associated pipeline-propagated uncertainties, where each of the 246 fibers are stored individually. A table of fiber positions maps each spectrum onto the image plane. However, for many of our observations a precise astrometric solution for the fiber positions is unknown due to an offset between the software which calculates the fiber positions and the telescope telemetry. To reconstruct accurate fiber positions we first identify fibers which observe stars and identify which fibers the astrometric solution indicates should contain stars. In many cases the stars are located between fibers. To account for this we use a simple Gaussian centroid weighted by the observed flux $5000 \leq \lambda \leq 5010 \text{ \AA}$ to find the correct sky position of the star. We then shift the fiber grid to match the sky position of the stars as reported by the SDSS. Typical shifts are $0.5'' - 4''$, less than the width of a single fiber. For each observation we use as many stars as possible and combine the shifts to generate a mean offset. This offset is applied to all dithers of each observation. There is little need to obtain highly accurate fiber positions as the $4''.24$ fibers ensures that reasonably correct positions will identify which fibers contain galaxies.

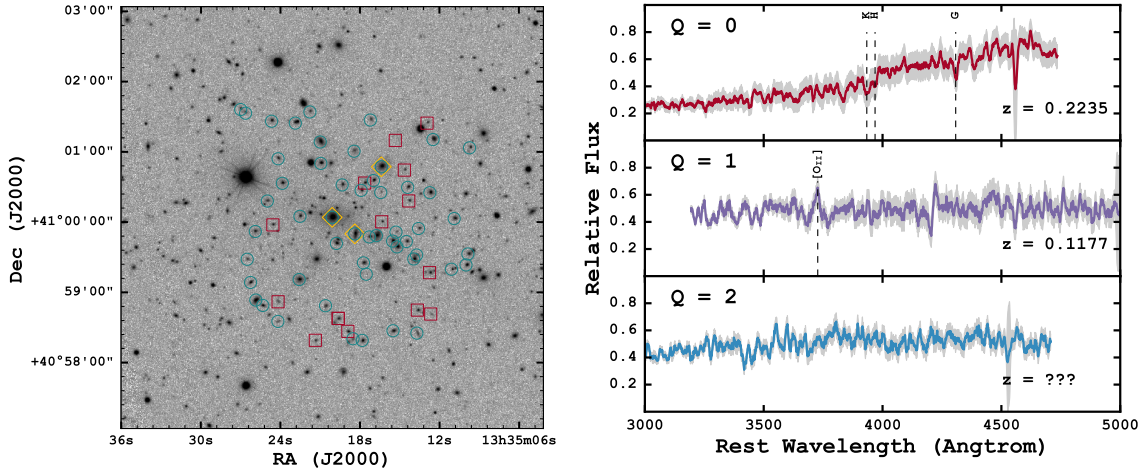


Figure 3.2: SDSS *r* image of cluster MSJ133520.1+410004.1. The symbols show the position of observed galaxies. Turquoise circles indicate galaxies with $Q = 0$ or $Q = 1$ spectroscopic redshifts, red squares indicate galaxies where a redshift could not be reliably determined, and the yellow diamond corresponds to galaxies with pre-existing redshifts from the SDSS. *Right:* Example spectra, with major features identified, showing the three quality flags. $Q = 0$ represents the best quality spectra and $Q = 2$ the poorest quality. Grey shaded regions show the P3D internally estimated, relative errors. We take galaxies with $Q = 0$ and $Q = 1$ for the analysis in this study.

We use a simple sky subtraction scheme to remove the majority of the sky contamination. Because the majority of fibers for any single pointing are empty, we use a 3σ clipped median of all spectra at each wavelength which removes fibers containing continua leaving only blank fibers. A simple mean combines the sky fibers into a single sky spectra. The result is then subtracted from every fiber. This adequately removes the bulk of sky emissions lines, but often fails to completely remove the [O I] line at 5577 Å. Our inspection of the sky subtracted spectra shows residual [O I] line flux approximately 10 – 15% of the un-sky subtracted level. We mask any emission line with a sky-subtraction residual $> 10\%$ to ensure they have minimal effect.

After reducing all spectra we find an average residual uncertainty in the wave-

length solution of $\sigma_\lambda \sim 0.4$ Å or 24 km s⁻¹ at 5000 Å, small compared to the instrumental resolution. We find an average instrumental resolution of ~ 144 km s⁻¹, by fitting Gaussians to the observed emission lines in the calibration lamp images. Combining the two in quadrature gives a total instrumental resolution of $\sigma_{inst} = 146$ km s⁻¹, similar to that of other studies using the MS (e.g., [Murphy et al. 2011](#); [Blanc et al. 2013](#)).

3.4 Analysis

The analysis of our reduced spectra occurs in two stages. First we derive individual redshifts using the observed spectra, and then utilize the redshifts collectively to identify which galaxies likely belong to the galaxy cluster.

Individual galaxy selection is done through cross matching the IFU fiber sky positions with galaxies selected from the SDSS. To collect the galaxies from the SDSS, we select all galaxies with $g < 22$ mag within 3' of the BCG in each cluster. For each cluster we create catalogs of photometry in all SDSS bands (*ugriz*), photometric redshift, and any spectroscopic redshift. The following SQL query accomplishes this task for MSJ010455.4+000336.3.

```
SELECT TOP 1000 G.objid ,
       G.ra ,
       G.dec ,
       G.u ,
       G.err_u ,
       G.g ,
       G.err_g ,
       G.r ,
       G.err_r ,
       G.i ,
       G.err_i ,
       G.z ,
       G.err_z ,
       Pz.z      AS Photoz ,
       Pz.zerr AS Photoz_err ,
```

```

        SO.specobjid ,
        SO.ra    AS Spec_ra ,
        SO.dec   AS Spec_dec ,
        SO.z     AS Specz ,
        SO.zerr  AS Specz_err
FROM   galaxy AS G
        JOIN dbo.Fgetnearbyobjeq(16.2307083,0.0600917,3) AS GN
            ON G.objid = GN.objid
        LEFT JOIN photoz AS Pz
            ON G.objid = Pz.objid
        LEFT JOIN specobj AS SO
            ON G.objid = SO.bestobjid
WHERE  G.g < 22
        AND clean = 1
        AND (calibstatus_r & 1) != 0

```

Because of the large number of fiber pointings, only fibers which overlap within $4''.16$ of an SDSS source are considered for redshift analysis. The left panel of Figure 3.2 shows cluster MSJ133520.1+410004.1 with the SDSS detections and measured redshifts overlaid. Orange diamonds are galaxies with SDSS available redshifts. The blue circles and red squares correspond to galaxies where a redshift was and was not determined from the observed spectra. See Figure A.1 for a similar representation of the remaining nine clusters.

3.4.1 Redshift Catalog

A redshift solution is determined for each galaxy by cross-correlating (Tonry & Davis, 1979) each of the spectra with six galaxy template spectra from the SDSS[†] using a custom, Python-based interface[‡] to the xcsao task in the IRAF RVSAO package (Kurtz et al., 1992; Kurtz & Mink, 1998). For each galaxy we select the spectral template with the highest cross-correlation coefficient and visually inspect the fit. During visual inspection a quality flag (Q) is assigned. High-confidence redshifts,

[†]<http://classic.sdss.org/dr7/algorithms/spectemplates/index.html>

[‡]<https://github.com/boada/redshiftCode>

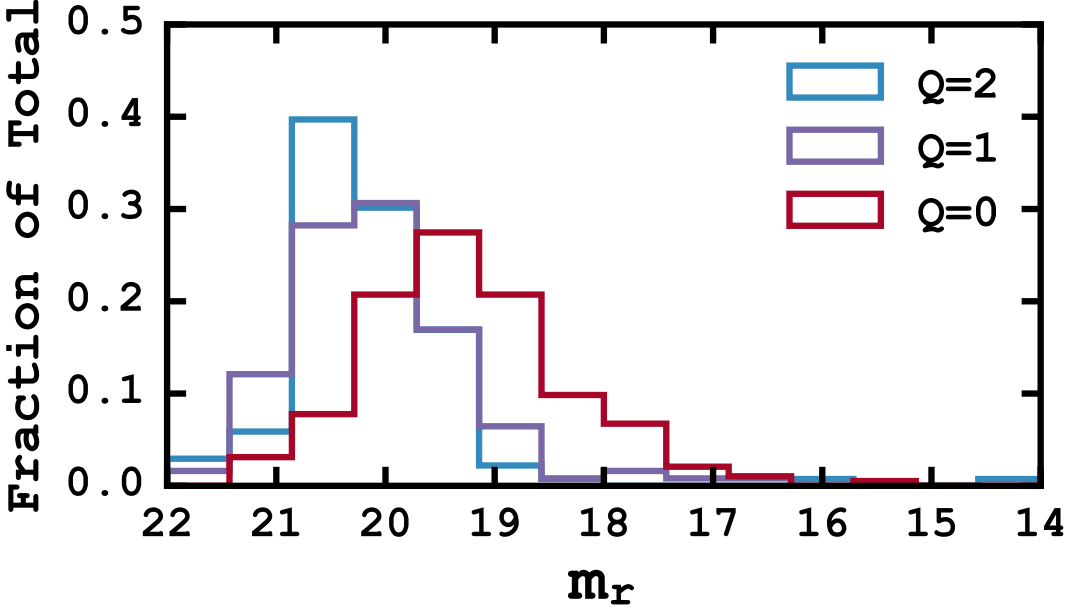


Figure 3.3: Redshift recovery fractions across all clusters. The bar heights represent the fraction of the total redshifts with the respective Q value at a particular magnitude. For example, $\sim 40\%$ of the $Q = 2$ redshifts have $m_r = 20.5 - 21$. We find a general decrease in redshift quality with increasing m_r .

clearly determined by at least two obvious features (such as the Ca⁺ H, K and Ca G absorption features), receive $Q = 0$. Spectra with only a single strong feature (e.g., [O II] emission) are assigned $Q = 1$. Redshifts resulting from dubious or no obvious features are assigned $Q = 2$. Figure 3.2 shows representative example spectra for each of the Q flags. For the determination of cluster properties we only consider galaxies with spectroscopic quality flags of $Q = 0$ and $Q = 1$.

Figure 3.3 shows the distribution of Q values for the redshifts across all clusters. We attempt to estimate spectroscopic redshifts for 447 galaxies, of which 44% have $Q = 0$, 27% have $Q = 1$ and 29% have $Q = 2$. We find a general decrease in Q flag

with increasing m_r . Approximately 30% of the $Q = 0$ redshifts correspond to galaxies with $19 < m_r < 20$ mag whereas about 40% $Q = 2$ galaxies have $m_r = 20.5 - 21$ mag.

While, xCSAO reports errors on the cross-correlation redshift, previous work (e.g., [Quintana et al. 2000](#); [Sifón et al. 2016](#)) shows the cross-correlation velocity uncertainties are underestimated by up to a factor of two. We report our redshift uncertainties as twice the uncertainty estimated by xCSAO.

Redshift information, with $Q = 0$ or $Q = 1$ spectra, for each galaxy are given in Table 3.2. The right panel of Figure 3.2 shows selected spectra from cluster MSJ133520.1+410004.1 with corresponding best fitting SDSS template. See the appendix for the remaining nine clusters.

Table 3.2: Spectroscopic redshifts for galaxies in MSJ133520.1+410004.1 measured with the MS: Column 1: The telescope pointing; Column 2: The dither position; Column 3: The fiber number; Column 4: The right ascension of the galaxy; Column 5: The declination of the galaxy; Column 6: The observed SDSS r magnitude; Column 7: The galaxy redshift; Column 8: The redshift Q flag; Column 9: The galaxy membership information; Column 10: The clustercentric radial distance; Column 11: The LOSV of the galaxy with respect to the cluster. See the appendix for similar tables for the remaining nine clusters.

tile	dither	fiber	RA (J2000)	DEC (J2000)	r (mag)	redshift	Q	Member	R (Mpc)	LOSV (km s $^{-1}$)	
(1)	(2)	(3)	(4)	(5)	(6)	(7)	(8)	(9)	(10)	(11)	
GL	NE	1	14	13:35:27.004	+41:01:36.20	20.47	0.2019±0.0003	1	...	0.40	-6945±146
	NE	1	111	13:35:24.177	+41:00:54.16	20.10	0.1178±0.0001	1	...	0.15	-27397±63
	NE	1	154	13:35:23.853	+41:00:33.19	19.28	0.2214±0.0002	0	...	0.18	-2214±83
	NE	2	6	13:35:21.777	+41:01:34.15	20.38	0.1691±0.0002	1	...	0.27	-14929±102
	NE	2	14	13:35:26.632	+41:01:33.06	20.95	0.0403±0.0003	0	...	0.09	-46214±131
	NE	2	63	13:35:20.998	+41:01:08.49	17.90	0.2381±0.0001	0	✓	0.25	1849±49
	NE	3	22	13:35:22.879	+41:01:24.60	19.76	0.2386±0.0003	0	✓	0.33	1961±131
	NE	3	25	13:35:24.669	+41:01:26.21	19.54	0.1444±0.0001	0	...	0.25	-20924±58
	NE	3	73	13:35:18.447	+41:01:00.60	19.63	0.0779±0.0001	0	...	0.09	-37080±29
	NE	3	106	13:35:20.957	+41:00:50.19	18.83	0.2235±0.0002	0	✓	0.17	-1691±78
	NE	3	147	13:35:19.341	+41:00:31.82	19.48	0.2380±0.0001	0	...	0.11	1822±73
	NE	3	185	13:35:24.990	+41:00:18.06	20.51	0.1887±0.0002	1	...	0.18	-10169±83
	NE	3	206	13:35:20.095	+41:00:04.12	16.39	0.2274±0.0001	1	✓	0.00	-763±34
	NE	3	210	13:35:22.528	+41:00:05.00	19.59	0.2242±0.0001	1	✓	0.10	-1543±49
	NW	1	127	13:35:16.384	+41:00:47.33	17.43	0.2377±0.0001	0	✓	0.23	1752±68
	NW	1	167	13:35:14.400	+41:00:29.73	19.69	0.2333±0.0002	0	✓	0.26	690±117
	NW	2	27	13:35:17.216	+41:01:27.25	20.21	0.1512±0.0002	0	...	0.24	-19279±117
	NW	2	63	13:35:12.486	+41:01:10.57	18.84	0.1638±0.0001	0	...	0.31	-16210±44
	NW	2	73	13:35:09.729	+41:01:03.49	20.00	0.2402±0.0001	1	...	0.50	2367±58
	NW	2	165	13:35:12.728	+41:00:25.16	18.74	0.2394±0.0001	0	✓	0.33	2155±58
	NW	2	171	13:35:16.434	+41:00:25.31	21.68	0.1617±0.0002	1	...	0.13	-16728±121

Table 3.2 Continued

tile	dither	fiber	RA (J2000)	DEC (J2000)	<i>r</i> (mag)	redshift	<i>Q</i>	Member	R (Mpc)	LOSV (km s ⁻¹)	
(1)	(2)	(3)	(4)	(5)	(6)	(7)	(8)	(9)	(10)	(11)	
NW	2	173	13:35:17.911	+41:00:27.16	19.49	0.1039±0.0002	0	...	0.06	-30763±107	
	2	220	13:35:10.891	+41:00:03.07	19.45	0.2994±0.0002	0	...	0.47	16739±102	
	2	239	13:35:13.582	+40:59:54.58	20.24	0.2316±0.0002	1	✓	0.28	265±92	
	3	142	13:35:16.981	+41:00:35.55	19.44	0.2233±0.0002	0	✓	0.17	-1745±78	
	SE	1	27	13:35:25.896	+40:59:52.05	19.35	0.2295±0.0004	1	✓	0.25	-238±170
	SE	1	46	13:35:19.779	+40:59:41.85	18.73	0.2293±0.0002	0	✓	0.08	-284±107
	SE	1	86	13:35:26.506	+40:59:28.30	20.59	0.2255±0.0002	1	✓	0.29	-1205±112
	SE	1	123	13:35:22.588	+40:59:11.02	18.17	0.2307±0.0002	0	✓	0.22	44±102
	SE	1	129	13:35:26.254	+40:59:08.50	19.42	0.1282±0.0002	0	...	0.20	-24863±107
	SE	2	164	13:35:20.600	+40:58:48.65	20.02	0.2938±0.0001	0	...	0.33	15369±53
	SE	3	157	13:35:25.857	+40:58:53.46	18.31	0.1701±0.0001	0	...	0.28	-14684±29
	SE	3	171	13:35:25.332	+40:58:48.88	19.49	0.2400±0.0003	0	...	0.36	2296±126
	SE	3	198	13:35:24.191	+40:58:35.23	20.83	0.1177±0.0002	1	...	0.21	-27419±87
	SW	1	41	13:35:17.295	+40:59:47.40	19.87	0.2231±0.0002	0	...	0.13	-1808±107
	SW	1	114	13:35:17.529	+40:59:15.55	20.60	0.2493±0.0003	1	...	0.22	4561±156
	SW	1	224	13:35:13.709	+40:58:25.25	20.03	0.1276±0.0003	0	...	0.28	-25006±126
	SW	1	227	13:35:15.509	+40:58:27.26	19.27	0.2328±0.0002	0	✓	0.41	559±83
	SW	1	245	13:35:17.832	+40:58:19.02	19.29	0.2211±0.0003	1	...	0.39	-2275±136
	SW	1	246	13:35:18.529	+40:58:20.43	21.31	0.1970±0.0002	1	...	0.34	-8140±117
	SW	2	24	13:35:15.282	+40:59:51.52	21.29	0.2225±0.0002	1	✓	0.20	-1934±97
	SW	2	29	13:35:18.391	+40:59:50.06	18.17	0.2405±0.0001	0	...	0.09	2440±44
	SW	2	39	13:35:15.539	+40:59:43.86	18.73	0.2263±0.0002	0	✓	0.20	-1023±107
	SW	2	53	13:35:15.211	+40:59:38.90	18.73	0.2412±0.0001	0	✓	0.23	2593±58
	SW	2	59	13:35:09.857	+40:59:32.82	19.83	0.2334±0.0002	1	✓	0.45	697±107
	SW	2	65	13:35:13.725	+40:59:31.94	20.58	0.3156±0.0003	0	...	0.37	20688±156
	SW	2	86	13:35:17.737	+40:59:25.25	19.71	0.2236±0.0002	0	✓	0.17	-1684±78

Table 3.2 Continued

tile	dither	fiber	RA (J2000)	DEC (J2000)	<i>r</i> (mag)	redshift	<i>Q</i>	Member	R (Mpc)	LOSV (km s ⁻¹)
(1)	(2)	(3)	(4)	(5)	(6)	(7)	(8)	(9)	(10)	(11)
SW	2	90	13:35:11.098	+40:59:19.79	20.41	0.2354±0.0002	0	✓	0.42	1195±97
SW	3	26	13:35:16.763	+40:59:48.52	17.94	0.2250±0.0001	0	✓	0.15	-1334±34
SW	3	37	13:35:14.503	+40:59:43.50	19.79	0.2428±0.0002	0	✓	0.26	2979±107
SW	3	65	13:35:13.944	+40:59:28.57	18.60	0.2362±0.0001	0	✓	0.29	1385±58
SW	3	73	13:35:10.002	+40:59:23.42	19.52	0.2307±0.0001	0	✓	0.45	39±73

3.4.2 Cluster Membership

We first determine the redshift of the cluster (z_c) as the average redshift of all cluster galaxies with $Q=0$ and $Q=1$. This serves as a zero-point from which all other galaxies will be compared. An incorrect cluster redshift introduces errors into the measured line of sight velocity (LOSV) and corresponding dispersion, which, in turn, contributes to errors associated with dynamical mass and radius.

In simple terms, the cluster redshift is the mean of the redshifts of all galaxies associated with the cluster. However, because the standard mean can be quite sensitive to outliers or otherwise contaminated data, we use the biweight location estimator (Beers et al., 1990) which provides improved performance. The biweight location provides protection against a small number of interlopers. Therefore, the process of determining z_c and the cluster membership are linked. We begin with the nominal z_c (see Table 3.1) and apply an initial velocity cut of 5000 km s^{-1} to remove any foreground or background galaxies. Then, using the membership determination techniques described below we determine the member galaxies from which a new z_c is calculated. The entire process is repeated until convergence, usually within a single iteration. The cluster central redshift and associated 68% uncertainties, derived from bootstrap resampling, are given in Table 3.3.

To reject the galaxies not associated with the targeted cluster, we employ two methods depending on the number of galaxies associated with each cluster. For clusters with 20 or more $Q = 0$ or $Q = 1$ redshifts we use the “shifting gapper” method of (e.g., Fadda et al. 1996; Crawford et al. 2014), which combines both the positional and velocity information. Galaxies are first sorted by their radial separation from the cluster center (See Table 3.1) and binned into radial bins of at

least 10 members. Once in the radial bins, the galaxies are sorted by the LOSV,

$$LOSV = c \frac{(z - z_c)}{(1 + z_c)} \quad (3.1)$$

where c is the speed of light in km s^{-1} , z is the redshift of the individual galaxy and z_c is the redshift of the cluster. Any galaxy with a LOSV greater than 1000 km s^{-1} of a neighboring galaxy (the velocity “gap”) is rejected as an interloper. The procedure repeats until the number of galaxies stabilizes in the bin. Once the members have been identified we recompute z_c , LOSVs, and begin the membership selection again. This entire process is repeated until the number of member galaxies remains constant. This is normally achieved within a single iteration.

For galaxy clusters with fewer than 20 $Q = 0$ or $Q = 1$ redshifts we employ the general of membership determination method outlined in [Wilman et al. \(2005\)](#); [Connelly et al. \(2012\)](#). We assume an initial velocity dispersion, $\sigma(v)$, of $500(1 + z)$ km s^{-1} and apply both redshift and spatial limits given by:

$$\delta(z)_{max} = 2\sigma(v)/c \quad (3.2)$$

and

$$\delta(r)_{max} = \frac{c \times \delta(z)_{max}}{bH(z)} \quad (3.3)$$

where $b = 9.5$ is the aspect ratio between the projected spatial and line-of-sight dimensions, $H(z) = H_0E(z)$ and $E(z) = \sqrt{\Omega_m(1 + z^3) + \Omega_\Lambda}$. We select all galaxies with $|z - z_c| < \delta(z)_{max}$ and radial separation, $R, < \delta(r)_{max}$. During each step, we update both the z_c and $\sigma(v)$ using the identified members and this process is repeated until the number of member galaxies converges, usually within three iterations.

To calculate the velocity dispersion in this membership determination method,

we use the gapper estimator (Beers et al., 1990) which provides accurate dispersions for groups as small as five members (Hou et al., 2009). It is given by

$$\sigma_g = \frac{\sqrt{\pi}}{N(N-1)} \sum_{i=1}^{N-1} w_i g_i \quad (3.4)$$

where N is the number galaxies, the weights are $w_i = i(N-i)$ and $g_i = LOSV_{i+1} - LOSV_i$ are the gaps between ordered pairs of radial LOSVs. The dispersion estimate is corrected by 1.135 to account for the 2σ redshift space cut applied during membership determination (Connelly et al., 2012). We follow this method for the calculation of the dispersion for consistency in member determination only. The final velocity dispersion of each cluster is determined in the following subsection.

Membership information for cluster MSJ133520.1+410004.1 is given in Column 9 of Table 3.2. See the appendix for the membership of the other observed clusters.

3.4.3 Line-of-Sight Velocity Dispersion

To compute the line-of-sight velocity dispersion (LOSVD) of each cluster we follow the maximum likelihood method of Walker et al. (2006). We assume that the each galaxy is drawn from a Gaussian distribution centered on the mean cluster velocity and we maximize the log of the product of each cluster member's individual Gaussian probabilities (their Eq. 8):

$$\ln(p) = -\frac{1}{2} \sum_{i=1}^N \ln(\sigma_i^2 + \sigma_p^2) - \frac{1}{2} \sum_{i=1}^N \frac{(v_i - \langle u \rangle)^2}{(\sigma_i^2 + \sigma_p^2)} - \frac{N}{2} \ln(2\pi). \quad (3.5)$$

where N is the number of member galaxies, σ_p , $\langle \mu \rangle$, and σ_i are the LOSVD, the average radial velocity and the error on the individual LOSVs respectively. To maximize the probability, we use EMCEE[§] (Foreman-Mackey et al., 2013), a Monte Carlo

[§]<http://dan.iel.fm/emcee/current/>

Markov Chain (MCMC) sampler, based on affine-invariant ensemble sampler (see [Goodman & Weare 2010](#) for details on affine-invariant samplers). We set priors on $\langle \mu \rangle$, and σ_p by requiring that $\langle \mu \rangle$ lies between the maximum and minimum LOSV and that σ_p be positive and less than 1400 km s^{-1} which corresponds approximately to a 10^{16} M_\odot cluster at $z = 0$, larger than any expected cluster mass in our sample. We draw twenty thousand samples from the posterior probability distribution and report a measured LOSVD as the median value of the posterior probability distribution with 68% error bars defined as the square root of the second moment of the same distribution.

3.5 Estimating Cluster Masses

The goal of this section is to describe the methods used to estimate (or predict) the total masses of the clusters in our sample. We test two distinct approaches. We begin the discussion with a traditional power law (PL) based approach where we estimate the cluster mass based on the LOSVD measurement. The second is a machine learning (ML) based approach where we use a combination of cluster observables to predict a cluster mass. The ML approach requires additional discussion about the creation of a suitable training set. We conclude with an examination of how this training set can potentially influence the results of the ML method.

3.5.1 PL Estimates of Cluster Mass

We adopt the scaling relation of [Munari et al. \(2013\)](#) to estimate cluster masses based solely on their LOSVD. The scaling relation is based on the work of [Evrard et al. \(2008\)](#) and has the form:

$$M_{200c} = \frac{10^{15}}{h(z)} \left(\frac{\sigma_{1D}}{A_{1D}} \right)^{1/\alpha} \text{M}_\odot \quad (3.6)$$

where $A_{1D} = 1177 \pm 4.2 \text{ km s}^{-1}$, $\alpha = 0.364 \pm 0.0021$, $h(z) = H(z)/100$, and σ_{1D} is the LOSVD. The relation is calibrated through a cosmological simulation using galaxies (instead of dark matter particles or subhalos) as the tracers of LOSVD. This choice of tracer results in dynamical masses which are 16 – 26% lower (e.g., Kirk et al. 2015; Sifón et al. 2016) than masses obtained through the scaling relation of Evrard et al. (2008), which has been calibrated using dark matter particles alone. This is due to dynamical effects which act upon the galaxies but not the dark matter particles.

We use the cluster redshift, given in Column 5, and the LOSVD values given in Column 6 of Table 3.3 along with Equation 3.6 to estimate the total mass of our ten clusters. The log of the predicted mass for each cluster is given in Column 7 of Table 3.3.

3.5.2 Supervised Machine Learning

Supervised ML provides an algorithm to infer the relationship between a set of known input variables (features) and a set of desired outputs (targets), through the use of a training set (see Chapter 2). The training set consists of both features and desired targets, which the ML algorithm uses to “learn” their relationship. The algorithm is then provided with a dataset consisting of only the features, and uses the inferred relationship to predict appropriate target values. Part of the training set is often reserved as a *testing* set (e.g., Ripley 2007; Xu et al. 2013; Ntampaka et al. 2015a,b; Acquaviva 2016) which is used to both select and train the specific ML algorithm.

Just as in Chapter 2, we rely on an ensemble ML method (e.g., Caruana & Niculescu-Mizil 2006) known as a forest of randomized decision trees (or random forest; RF; Tin Kam Ho 1995, 1998), which we prefer due to their straightforward design and easily accessible uncertainty estimates. A RF is a type of ensemble

method where the trees can be visualized as flow chart. The path through the flow chart (the trees) is decided by the values of the training features at each fork. RF use a random subset of the train data to decide which fork should be followed. The final prediction is the mean of each tree’s final value. We optimize the input parameters (often called hyper-parameters) of our RF by further splitting our testing set into a cross-validation (CV) set. We use 5-fold CV, where the testing set is split (folded) five times, throughout. The RF methods implemented in this work are part of the SCIKIT-LEARN ([Pedregosa et al., 2012](#)) Python library.

Building off the work in Chapter 2, we use the “Buzzard” semi-analytical model to provide both the observable features and desired targets in order to train our ML method. The Buzzard mock galaxy catalog contains 238 million galaxies with r mag < 29 and $z \leq 8.7$. The galaxies are located in a 398.49 degree² portion of the sky and their luminosities are derived from a combination of Sub-halo Abundance Matching (SHAM; [Reddick et al. 2013](#)) and Adding Density Dependent Spectral Energy Distributions (ADDSED). The galaxies are assigned to the dark matter halos identified by the ROCKSTAR halo finder ([Behroozi et al., 2013](#)). The catalogs assume the following cosmological parameters: $\Omega_\Lambda = 0.714$, $\Omega_M = 0.286$, $\sigma_8 = 0.82$ and $H_0 = 70 \text{ km s}^{-1}\text{Mpc}^{-1}$, which we have also adopted for general use in this work. See Chapter 2 for a more thorough description of the process used to create the catalogs.

3.5.3 ML Based Observations

In order to create a mock dataset which resembles our actual observations we first rely on the RF method as a classifier. The goal is to assign each galaxy in the Buzzard catalog a Q flag of either 0, 1 or 2 based on their observed magnitudes in the five SDSS filters, $ugriz$, the ten combinations of possible colors, and the square of

those colors. [Acquaviva \(2016\)](#) uses a similar feature set to predict the metallicity of SDSS galaxies with good effect.

The classifier is trained using the redshift catalog derived from our cluster observations (Section [3.4.1](#)), and the 447 observations are split into a training, CV and test sample. We use the training set to train the ML method, the CV set to tune the model hyper-parameters and the test sample to verify how well our model classifies each galaxy. We also perform recursive feature elimination to remove features which contribute very little to the classification.

We compute two statistics to evaluate how well our model classifies the galaxies, the recall and the precision. The recall is the number predicted compared to the true number of classifications, N_{pred}/N_{true} . The precision is the number of correct predictions compared to the total number of predictions for each class, N_{corr}/N_{pred} . In both cases the metrics range from zero to one, and higher numbers are better. For our optimized RF classifier we achieve overall recall and precision of $\sim 60\%$. For the individual classes (Q flags), the RF classifier performs significantly better when classifying $Q = 0$ and $Q = 2$ galaxies, with recall rates well above 70%. The $Q = 1$ training galaxies have significant overlap between $Q = 0$ and $Q = 2$ (see Figure [3.3](#)) which leads to a recall for $Q = 1$ galaxies of only $\sim 20\%$.

Figure [3.3](#) shows there is significant overlap between the Q flags. In our testing, we find no combination of features which wholly separates the Q flags, providing a high level of confusion for the RF. We find similar levels of recall and precision for other ML classification methods besides RF.

We assign each galaxy in the Buzzard catalog with $z < 0.5$ and $g < 22$ mag a Q flag using the optimized RF classifier trained with all 447 observations. Figure [3.4](#) shows the Q flag distribution as a function of r magnitude. The total distribution of the 2.7 million Q flags is 45.6% $Q = 0$, 24.7% $Q = 1$, and 29.6% $Q = 2$. This

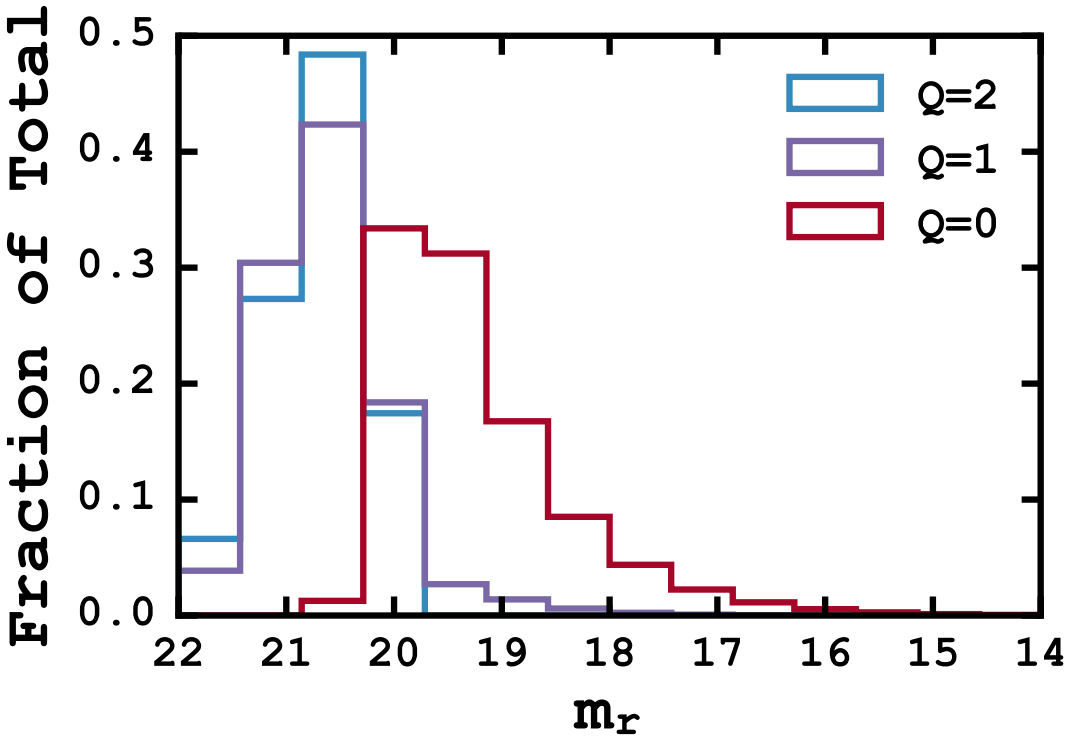


Figure 3.4: Quality flag (Q) assignments for the 2.7 million Buzzard catalog galaxies with $g < 22$ mag. The bar heights represent the fraction of the total redshifts with the respective Q value at a particular magnitude. The distributions resemble the actual observations in Figure 3.3. See the text for a detailed explanation of the classification process.

distribution closely resembles the fractions of the actual observations with some $Q = 1$ galaxies misclassified as $Q = 0$. Because we use galaxies with either $Q = 0$ or $Q = 1$ this does not significantly bias our analysis.

3.5.4 ML Based Cluster Masses

We use the galaxies with reliably measured spectroscopic redshifts ($Q = 0$ and $Q = 1$) created in the previous subsection to construct total mass distributions of the mock clusters. For this task we again use a RF, not as a classifier but as a regressor, which predicts a cluster mass given a set of input features, such as the

observed LOSVD and redshift. Similarly to our classification methods, we create an optimized ML method by splitting the Buzzard catalogs into a training, CV, and testing set.

Because the cluster masses presented with this method are predictions based on the feature data, any uncertainties quoted by this method are prediction intervals not confidence intervals. Prediction intervals are an estimate of the interval encompassing future observations, with a given probability. Confidence intervals, on the other hand, describe the different moments of a population. The prediction intervals are unique to each prediction, and are often based on the underlying assumption of normally distributed residuals. RF estimators do not assume normally distributed residuals, and thus, require special treatment.

The prediction intervals for our RF estimator are based on the method of quantile regression forests ([Meinshausen, 2006](#)). The basic principle is that we record all response variables (the predictions), not simply the mean. This allows us to give the prediction as the full conditional probability distribution of all possible predictions. For brevity, we quote predicted masses as the median prediction and the 68% prediction interval as the square root of the second moment of the full conditional probability distribution.

3.5.5 The Importance of Training Features

The data used to train our ML algorithm is critical to the success of the method. We require training data which is broad enough to expose the ML method to a wide enough range of cluster parameters as not to influence the final outcome. The features of our training sample can be selected such that it does not bias the final predictions in an expected way. Figure [3.5](#) shows the σ and z features of the training

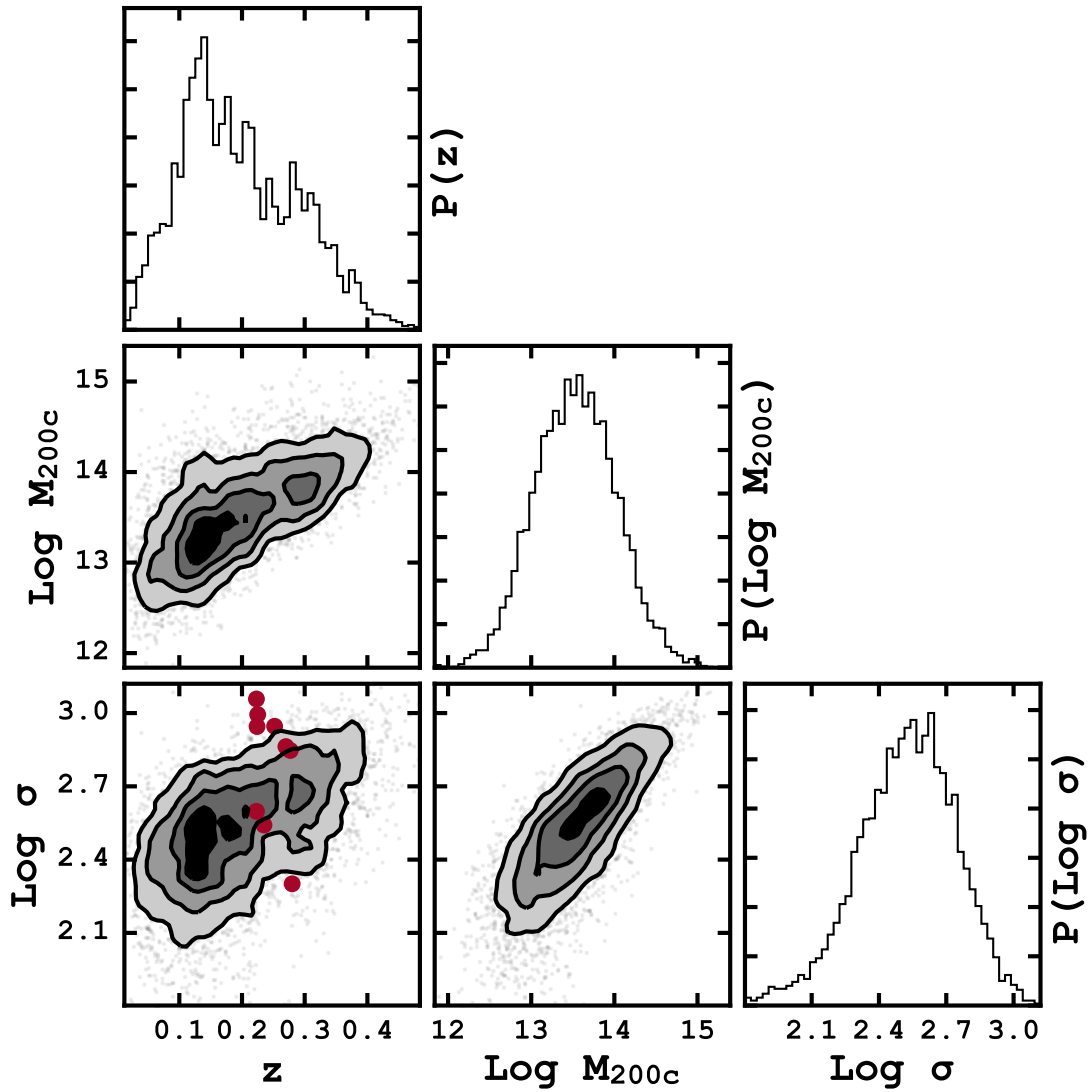


Figure 3.5: Contour plot of the *training* data with features σ and z . The corner plots shows all of the one and two dimensional posterior probability distributions used to determine the correct cluster mass. The colored circles show the position in the log σ -redshift plane of the ten clusters in this sample.

sample from the Buzzard catalogs.[¶] The large red circles indicate the observed positions of our ten clusters in relation to the training data. Immediately noticeable,

[¶]Contour plots based on Foreman-Mackey et al. (2016).

is that our observed clusters occupy a narrow redshift range ($0.2 < z < 0.3$). We also notice that seven of the ten clusters sit at the top edge of the training data in the z -log σ plane. Because the observed clusters are separate from the training data, the accuracy of the predictions of the cluster masses will be diminished. Below, we consider alternative training datasets which give improved cluster mass predictions when compared to the PL cluster mass estimates.

Because the of the difference in cosmological volume covered by the SDSS and simulated by Buzzard, there are too few clusters in Buzzard, at $z \sim 0.2$, and with σ as large as the clusters in our sample. Predictions based on the Buzzard catalogs give a higher likelihood that clusters at $z \sim 0.2$ will be of lower total mass, when the redshift is included as a feature. This becomes apparent by examining the z -log M_{200c} plane in Figure 3.5. The vast majority of clusters with $0.2 < z < 0.3$ have masses between $10^{13} - 10^{14} M_\odot$, whereas the observed LOSVD (σ) values of our clusters would place them above $10^{15} M_\odot$.

To combat the effect of cluster mass under-prediction, we make two critical changes from our method presented in Chapter 2. First, instead of using the membership information provided by the Buzzard catalogs we observe the clusters much in the same way we have with our actual observations. We select all galaxies within $2.3'$ around the center of each cluster (see Figure 3.1 for an illustration), and determine the cluster membership using the methods described in Section 3.4.2. This serves to broaden the LOSVD distribution of the training data as both true member galaxies will be excluded and interloping galaxies will be erroneously included. Second, we exclude the redshift information from the training features when predicting the cluster masses. This has the effect of flattening the halo mass function (HMF), allowing for high mass clusters to exist at all redshifts. However, the fewer training features also lowers the predictive power through an increase in both the bias and

scatter (see Figure 2.6 as an example).

Furthermore, we create an additional training dataset with a truly flat HMF. We flatten the HMF by selecting clusters in a range of true mass bins with uniform probability. In true cluster mass bins where there are too few clusters to randomly select the desired number of samples, we generate “new” clusters by rotating the viewing angle of each cluster and then re-observing the cluster in the new orientation. This creates a uniform true cluster mass distribution from which we train the ML algorithm.

3.6 Results and Discussion

The goal of this work to perform a practical test of some of the potential applications of a HETDEX-like survey to cluster science. Here, we present the predicted total masses of our ten clusters and estimate the absolute scale and scatter of a richness-mass relation based on those cluster masses. Because the accuracy of the predicted cluster masses is paramount to a well constrained richness-mass relation, we combine our results presentation with a discussion on their accuracy.

3.6.1 Cluster Masses

In Chapter 2, we find the ML based method with the LOSVD (σ), redshift (z) and number of galaxies observed (N_{gal}) showed both the smallest bias and scatter over the largest range of cluster masses. This worked well because the training data were selected from a volume of similar size to the survey in question. As discussed previously, we modify our analysis slightly and use the PL based approach (Eqn. 3.6) and the $ML_{\sigma, N_{gal}}$ method to estimate the masses of our ten clusters. This change in the ML method is the result of the differences in the cosmological volume of the SDSS and the Buzzard at $z \sim 0.2$.

The PL predicted masses versus the ML predicted masses are shown in Figure 2.6.

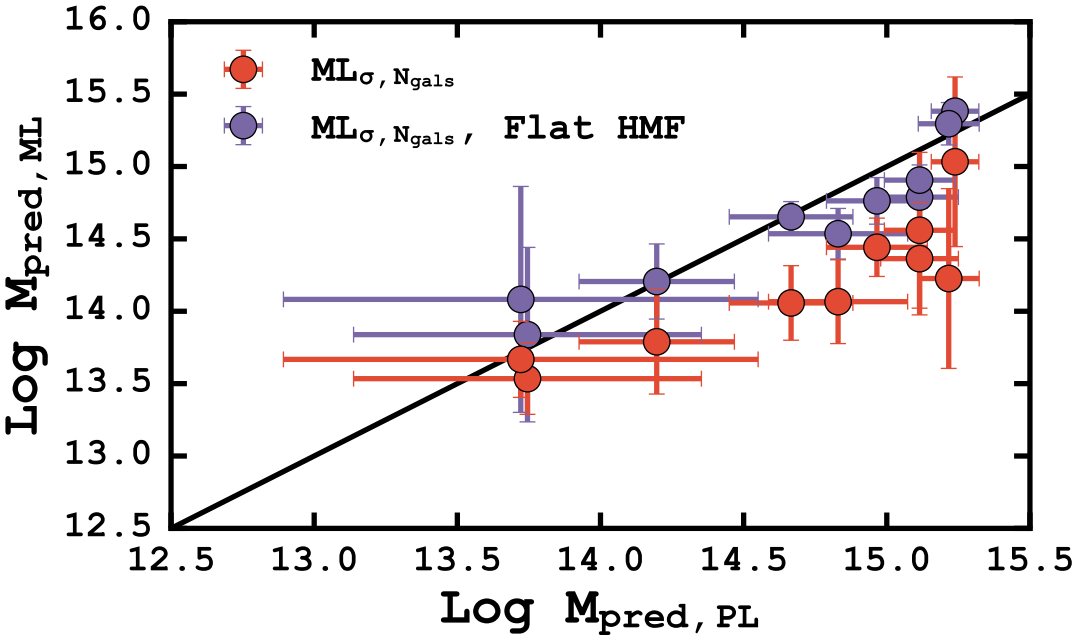


Figure 3.6: Comparison of the cluster mass estimates for the PL scaling relation (Equation 2.6) and the ML based mass predictions for the ten clusters in our observed sample. The orange points show the $\text{ML}_{\sigma, N_{gal}}$ predicted cluster masses using the Buzzard catalogs as a training set. The purple points represent $\text{ML}_{\sigma, N_{gal}}$ predictions based on a flattened Buzzard HMF which leads to an improved performance when compared to the PL cluster mass estimates. The solid black line shows the 1:1 relation. See text for a description of the process used to create the three estimates of cluster mass.

The orange points show our $\text{ML}_{\sigma, N_{gal}}$ predicted masses using the cluster abundances as given in the Buzzard catalog. The purple points are the $\text{ML}_{\sigma, N_{gal}}$ estimates when the Buzzard catalog HMF has been flattened.

The uniform true cluster mass distribution decreases the frequency that clusters of lower mass dominate (by number) at any individual velocity dispersion which reduces the likelihood the ML will underestimate the predicted cluster mass due to the underlying distribution of training clusters. If there are many more low and

intermediate mass clusters compared to high mass clusters, as is the case in the Buzzard catalogs, the ML algorithm is more likely to predict a low or intermediate cluster mass as those objects are much more frequent in the training sample. Because of this change, the $\text{ML}_{\sigma, N_{gal}}$ trained on a flatten HMF predicts cluster masses similar to those of the PL. However, the flattening of the HMF increases the scatter at fixed true cluster mass for training features. This leads to little or no reduction in the amount of scatter in the predicted cluster masses for a fixed true cluster mass when compared to the scatter in the PL estimates of cluster mass.

Therefore, we elect to use the PL estimated cluster masses for as the primary cluster mass estimates for the remainder of this study. The $\text{ML}_{\sigma, N_{gal}}$ with a default HMF cannot reliably predict cluster masses for the highest mass clusters, and flattening the HMF, while improving the cluster mass predictions when compared to the PL estimates, does not accurately represent the universe. This underscores the need for a set of training data which accurately represents the cosmological volume being studied.

Furthermore, in Chapter 2, the cluster mass prediction process uses two steps. Firstly the cluster mass is predicted, and then the cluster mass is corrected by considering the bias and scatter of the training data. Here, we choose not to correct the cluster masses predicted by either the PL or ML method due to the dissimilarity between the training data and our observations. During our testing, we find that there are too few training clusters with masses $> 10^{15} \text{ M}_\odot$, using an unmodified HMF, to place reliable constraints on the bias and scatter. As we discuss below, these high mass cluster constitute the bulk of our sample. Because we are unable to provide these clusters, with bias corrections, we choose to not correct any cluster mass estimate, to facilitate consistency throughout.

The lack of a bias correction does not strongly effect our analysis as we are

primarily interested in the scatter of our cluster masses. The scatter is unaffected as the individual mass estimates are scaled up or down by a common factor.

Table 3.3: Summary of derived cluster parameters: Column 1: The cluster name; Column 2: The number of SDSS sources observed; Column 3: The number of $Q = 0(1)$ sources; Column 4: The number of member galaxies; Column 5: The redshift of the cluster; Columns 6: The LOSVD; Column 7: The PL predicted cluster mass; Column 8: The ML predicted cluster mass.

Cluster (1)	Sources (2)	$Q=0$ (1) (3)	Member (4)	z_c (5)	σ (km s^{-1}) (6)	PL $\log M_{pred}$ (7)	ML $\log M_{pred}$ (8)
MSJ010455.4+000336.3	41	10 (10)	15	0.2727 ± 0.0029	1194 ± 135	15.11 ± 0.14	14.84 ± 0.18
MSJ133520.1+410004.1	67	35 (17)	25	0.2310 ± 0.0025	1314 ± 91	15.24 ± 0.08	14.71 ± 0.47
MSJ140102.0+025242.6	67	14 (30)	16	0.2543 ± 0.0035	1295 ± 115	15.22 ± 0.11	14.55 ± 0.45
MSJ153656.3+242431.6	37	14 (14)	11	0.2255 ± 0.0034	932 ± 189	14.83 ± 0.24	14.21 ± 0.16
MSJ164019.8+464241.5	61	36 (14)	32	0.2274 ± 0.0020	1183 ± 121	15.11 ± 0.12	14.96 ± 0.23
MSJ172227.2+320757.2	61	26 (18)	23	0.2260 ± 0.0022	1044 ± 154	14.97 ± 0.18	14.54 ± 0.14
MSJ211849.1+003337.3	45	21 (8)	18	0.2750 ± 0.0026	820 ± 148	14.67 ± 0.22	14.30 ± 0.12
MSJ215422.9+003723.5	28	19 (2)	16	0.2167 ± 0.0026	547 ± 124	14.20 ± 0.27	14.04 ± 0.09
XMMXCSJ124425.9+164758.0	25	11 (8)	6	0.2316 ± 0.0033	375 ± 191	13.75 ± 0.61	13.60 ± 0.14
XMMXCSJ125650.2+254803.2	15	8 (3)	3	0.2821 ± 0.0059	372 ± 258	13.72 ± 0.83	13.52 ± 0.13

Table 3.3 presents a summary of the derived parameters for each cluster. We include the LOSVD, the estimated cluster redshift, and the number of member galaxies observed. We provide two predicted cluster masses, the PL based cluster mass and the $ML_{\sigma, N_{gal}}$ predicted cluster mass. We discuss the accuracy of both of these predictions in the following subsections.

3.6.2 Notes for Individual Clusters

Here we compare our PL inferred masses for the clusters in our sample to the previously reported estimates from the literature. Sifón et al. (2015) report total cluster masses for four of our clusters based on LOSVD measured from targeted spectra obtained with the Canada-France-Hawaii Telescope. They convert the LOSVD into a dynamical cluster mass using the PL scaling relation of Evrard et al. (2008) (which is the basis of our Equation 3.6) and estimate the uncertainties using jackknife resampling. One of our clusters has a reported LOSVD measurement and two have X-ray temperature measurements. On the whole, our PL estimated cluster masses are consistent with those previously reported in the literature; this stresses the utility of measuring cluster masses with IFU spectroscopy. In the following section we will discuss the ML estimated masses.

3.6.2.1 $MSJ133520.1+410004.1$ (Abell 1763)

Sifón et al. (2015) observe 103 member galaxies within r_{200} . They compute a LOSVD of 1130 ± 81 km s $^{-1}$, compared to our 1314 ± 91 km s $^{-1}$ based on 25 member galaxies. They report a $M_{200c} = (14.6 \pm 3.1) \times 10^{14}$ M $_{\odot}$, compared to our value of $M_{200c} = (17.4 \pm 3.2) \times 10^{14}$ M $_{\odot}$. The two estimates are consistent within the given errors, and the difference is due to our higher measured LOSVD.

3.6.2.2 MSJ140102.0+025242.6 (Abell 1835)

Sifón et al. (2015) report a $M_{200c} = (4.5 \pm 1.9) \times 10^{14} M_\odot$, based on 41 member galaxies within r_{200c} . We estimate a significantly different mass of $M_{200c} = (16.6 \pm 4.2) \times 10^{14} M_\odot$. This discrepancy is due to the large difference in measured LOSVD, $762 \pm 106 \text{ km s}^{-1}$ versus our $1295 \pm 115 \text{ km s}^{-1}$. However, Hoekstra et al. (2012) report a LOSVD for MSJ140102.0+025242.6 of 1218 km s^{-1} . Geller et al. (2013) find $M_{200c} = (16.57 \pm 1.86) \times 10^{14} M_\odot$ from the best fitting caustic mass profiles, which is similar to our reported value. Using *Chandra* X-ray observations, Bonamente et al. (2012) report a $M_{200c} = (8.35_{-0.86}^{+0.81}) \times 10^{14} M_\odot$. While our cluster mass estimate is not consistent with Sifón et al. (2015), we find it is very similar to other reported mass estimates based on virial techniques.

3.6.2.3 MSJ164019.8+464241.5 (Abell 2219)

With the largest number of member galaxies observed (of our sample), Sifón et al. (2015) use 241 member galaxies within r_{200c} to estimate a mass of $M_{200c} = (17.0 \pm 2.8) \times 10^{14} M_\odot$. We estimate $M_{200c} = (12.9 \pm 3.6) \times 10^{14} M_\odot$. Using weak lensing techniques, Applegate et al. (2014) report a mass of $(12.0_{-1.5}^{+1.5}) \times 10^{14} M_\odot$ within 1.5 Mpc, similar to our reported mass estimate.

3.6.2.4 MSJ172227.2+320757.2 (Abell 2261)

For MSJ172227.2+320757.2 we estimate $M_{200c} = (9.3 \pm 3.9) \times 10^{14} M_\odot$ compared to $M_{200c} = (7.0 \pm 2.0) \times 10^{14} M_\odot$ from Sifón et al. (2015). They base their estimate on 76 member galaxies within r_{200c} . There is reasonable agreement between the two estimates.

3.6.2.5 MSJ215422.9+003723.5 (Abell 2392)

The predicted mass of this cluster is significantly lower than expected. Previous work (Wing & Blanton, 2013) find it has a LOSVD of 1485 km s^{-1} well outside the estimated value from our analysis of 547 ± 124 . Wing & Blanton (2013) report a LOSVD based on 32 member galaxies within 3 Mpc of the cluster center. One possible explanation for the deviation between our result and that of Wing & Blanton (2013) is that our observations probe only the cluster core ($< 0.4 \text{ Mpc}$), while their measurements include galaxies much farther away. Previous theoretical work (e.g., Old et al. 2013) has shown the LOSVD to be sensitive to the radius at which it is measured. In addition, there is evidence to suggest that the cores of some galaxy clusters exhibit a smaller velocity dispersion than the outskirts (e.g., Bahcall 1977; Muriel et al. 2002).

3.6.2.6 XMMXCSJ124425.9+164758.0

With only six member galaxies identified, XMMXCSJ124425.9+164758.0 is near the very limit of our ability to produce accurate cluster mass estimates. Fortunately, the cluster has an measured x-ray temperature which we can use to as another estimate of mass. Its XCS data release 1^{||} (Mehrtens et al., 2012) measured temperature is $1.3_{-0.3}^{+0.2} \text{ KeV}$ which equates to $M_{500c} \approx (0.41 \pm 0.08) \times 10^{14} \text{ M}_\odot$ using the T_x -M relationship for low-temperature systems of Finoguenov et al. (2001).

We convert this X-ray inferred mass from M_{500c} to M_{200c} using the general prescription in Hu & Kravtsov (2003) to arrive at a predicted mass of $M_{200c} \approx (0.53 \pm 0.11) \times 10^{14} \text{ M}_\odot$, in very good agreement with our LOSVD predicted value of $M_{200c} \approx (0.59 \pm 0.81) \times 10^{14} \text{ M}_\odot$.

^{||}<http://www.astro.ljmu.ac.uk/~xcs/DR1/XCSDataRelease.html>

3.6.2.7 XMMXCSJ125650.2+254803.2

The three member galaxies identified in XMMXCSJ125650.2+254803.2 do not place a statistically strong constraint on the LOSVD predicted cluster mass. It too has a X-ray temperature measurement as part of XCS. Using the same approach as with XMMXCSJ124425.9+164758.0, a measured X-ray temperature of $1.4_{-0.3}^{+0.2}$ KeV gives a X-ray inferred cluster mass of $M_{200c} \approx 0.61 \times 10^{14}$ M_⊙. This is about 26% higher than our LOSVD derived cluster masses.

3.6.3 On the Accuracy of ML based Cluster masses

Many of the cluster masses predicted using the ML approach are significantly different from both the PL based masses and the values found in the literature. Specifically, the largest differences are for the high mass clusters, and this can wholly be attributed to the training data used to inform the ML method (see the discussion in Subsection 3.5.5).

In Chapter 2 we found significantly reduced scatter in our mass predictions through the use of ML methods. We argue that the amount of scatter and cluster mass accuracy are reasonable estimates of those for a survey such as HETDEX. In large part, this is because the cosmic volume probed by HETDEX is of similar size to that simulated by Buzzard. However, the clusters observed for this work are selected from the SDSS which covers a much larger cosmological volume. The smaller simulated volume of Buzzard leads to the issue where the training data does not accurately represent the population of clusters in question.

Simply, Buzzard lacks the intermediate redshift, high-mass cluster, which influences the ML predictions of the cluster mass. Improvements in the accuracy of the ML method are possible by (re-)introducing the cluster redshift as a feature (see Chapter 2 as an example), but that would require a training dataset that has the

same area/depth as the dataset used for the observations, in this case, the SDSS.

The prediction intervals output by the ML method also show the effect of the mismatched training sample. The ML prediction intervals are narrower than the PL-inferred confidence intervals for all clusters with masses below $10^{15} M_{\odot}$. This is due to an abundance of training clusters in this range. Above this, there are too few clusters to give reliable predictions and the prediction interval widens to reflect that situation.

It is important to note, that the cluster mass predictions from the ML methods are not a failure of the method. Based on the training data the algorithm has been exposed to, it has predicted cluster masses which closely resemble the observed features. Supervised ML shows incredible promise as a tool for future astrophysical investigations, but a deep understanding of how the input training data effects the target output is also required.

3.6.4 Optical Richness-Mass Relation

In Chapter 2, we show that HETDEX will be able to accurately estimate the absolute calibration and intrinsic scatter, $\sigma_{M|\lambda}$, of the optical-richness-cluster-mass relationship for a small range of intrinsic scatters. Here we use the ten clusters observed to demonstrate the ability of IFU observations similar to HETDEX to make mass determinations and to use those masses to place constraints on the optical-richness-cluster-mass relation. For our cluster mass estimates we use the masses predicted by the PL relation given in Equation 3.6.

To find a best-fitting richness-mass relation for our data we are required to fit $y = mx + b$ where $y = \log$ predicted cluster mass and $x = \log$ optical richness, considering measurement errors in richness and predicted cluster mass along with intrinsic scatter of the relation. We assume the intrinsic scatter is constant from

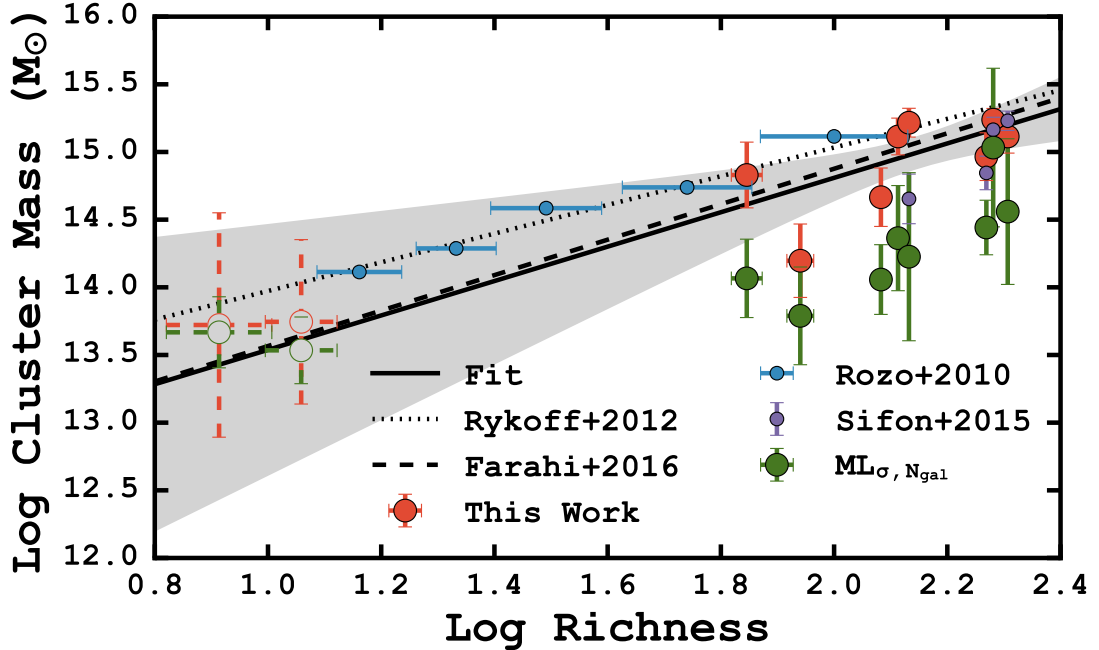


Figure 3.7: Richness, λ , versus total PL estimated cluster mass for the clusters in our sample, shown as orange points. The two dashed points are the X-ray selected clusters, and are excluded from the fit. The solid black line shows our best-fitting relation (Equation 3.13) based on the eight high mass clusters, the dashed line shows the relation from Farahi et al. (2016), and the dotted line shows the relation from Rykoff et al. (2012). The gray shaded region corresponds to the 68% confidence area on our best-fit. We include stacked WL masses from Rozo et al. (2010), the high-mass cluster mass estimates of Sifón et al. (2015) and our $ML_{\sigma, N_{gal}}$ predicted cluster masses for comparison.

point to point, and we assume (not necessarily correctly) that all measurement errors are Gaussian. With the assumption of all Gaussian scatters we have three quantities of interest: The probability of the predicted log cluster mass (y_i) given the observed log richness (x_i),

$$p(y_i|x_i) = \frac{1}{\sqrt{2\pi\sigma^2}} \exp\left(-\frac{[y_i - mx_i - b]^2}{2\sigma^2}\right) \quad (3.7)$$

which takes into consideration the intrinsic scatter in the relation, σ ; the probability of the true log richness value (\hat{x}_i) given an observed log richness (x_i),

$$p(\hat{x}_i|x_i) = \frac{1}{\sqrt{2\pi\sigma_{x,i}^2}} \exp\left(-\frac{[\hat{x}_i - x_i]^2}{2\sigma_{x,i}^2}\right) \quad (3.8)$$

which accounts for the uncertainty in the richness observation, $\sigma_{x,i}$; and the probability of the true log cluster mass (\hat{y}_i) given an observed log cluster mass (y_i),

$$p(\hat{y}_i|y_i) = \frac{1}{\sqrt{2\pi\sigma_{y,i}^2}} \exp\left(-\frac{[\hat{y}_i - y_i]^2}{2\sigma_{y,i}^2}\right) \quad (3.9)$$

which also considers the uncertainty associated with the log cluster mass prediction, $\sigma_{y,i}$. We combine these three probabilities into

$$p(\hat{y}_i|\hat{x}_i) = \int_{-\infty}^{\infty} dy_i p(\hat{y}_i|y_i) \int_{-\infty}^{\infty} dx_i p(y_i|x_i) p(x_i|\hat{x}_i). \quad (3.10)$$

We assume flat priors on x_i so that $p(x_i|\hat{x}_i) = p(\hat{x}_i|x_i)$ and substitute our probability equations from above. This gives

$$p(\hat{y}_i|\hat{x}_i) = \frac{1}{\sqrt{2\pi(\sigma^2 + \sigma_{y,i}^2 + m^2\sigma_{x,i}^2)}} \exp\left(-\frac{[y_i - mx_i - b]^2}{2(\sigma^2 + \sigma_{y,i}^2 + m^2\sigma_{x,i}^2)}\right) \quad (3.11)$$

which for $\sigma_{x,i} = 0$ (no uncertainty on the log richness measurement) reduces to the familiar form of a Gaussian with a combination of measurement error and intrinsic scatter. We convert this probability function into a likelihood by taking the product of all the individual probabilities,

$$\mathcal{L} = \prod_{i=1}^N p(\hat{y}_i|\hat{x}_i). \quad (3.12)$$

and maximize this likelihood by sampling from the posterior probability distribution using the MCMC methods described above. We quote the most probable slope and intercept as the mean value of the posterior probability distributions with uncertainties as the square root of the second moment of the same distribution.

To find our best-fitting relation we exclude the two *XMM* selected clusters due to the few number of observed member galaxies. After fitting to the remaining eight, high richness clusters, we find a best-fitting relation of

$$\text{Log } M_{200c}/\text{M}_\odot = 1.25 \pm 0.78 \text{ Log } \lambda + 12.29 \pm 1.68. \quad (3.13)$$

This best-fitting relation is shown in Figure 3.7 where the large filled, orange points are the PL estimated cluster masses from this work, and the dashed points are the excluded *XMM* selected clusters. We comment on the properties of our optical richness-mass relation and compare it to others from the literature in the following subsection.

We estimate the intrinsic scatter, $\sigma_{M|\lambda}$, in the relation two ways. The first is through our generative model, as it includes an intrinsic scatter term, which the MCMC samples directly. This gives $\sigma_{M|\lambda} = 0.23 \pm 0.16$ dex for the intrinsic scatter. We can also calculate the standard deviation of the residuals to the best-fitting line, which produces $\sigma_{M|\lambda} = 0.27 \pm 0.07$ dex. Both of these scatter estimates include the eight $\lambda > 60$ clusters. If we exclude MSJ215422.9+003723.5 where we significantly underestimate the mass when compared to literature values (see Subsection 3.6.2.5), the scatter for remaining seven clusters is $\sigma_{M|\lambda} = 0.24 \pm 0.09$ dex.

3.6.5 Calibration of the Richness-Mass Relation

Two recent studies (Farahi et al., 2016; Simet et al., 2016) use stacked cluster observations of velocity dispersions or WL, and in both cases report a PL index

of $\alpha \sim 1.3$. We find a similar (6% difference) PL index of $\alpha = 1.25$, albeit with significant uncertainty. Our absolute mass scale of $\log M_{200c}/M_\odot = 14.29 \pm 2.1$ dex at $\lambda = 40$ is in good agreement with the previously reported values of $\log M_{200c}/M_\odot = 14.34$ ([Simet et al., 2016](#)) dex and $\log M_{200c}/M_\odot = 14.35$ ([Farahi et al., 2016](#)) dex, although with much greater uncertainty. These large uncertainties are due to our sample have a low number of clusters; our fitting procedure cannot place tight constraints on the measured slope and intercept. With the many clusters expected to be observed with HETDEX these uncertainties should decrease significantly.

Our cluster masses estimates allow us to place promising constraints on the scatter in cluster mass at fixed richness, $\sigma_{M|\lambda}$. Using the SZE, [Saro et al. \(2015\)](#) find $\sigma_{M|\lambda} = 0.18^{+0.05}_{-0.08}$ at $\lambda = 70$. [Rykoff et al. \(2016\)](#) identify a similar scatter of 0.3 ± 0.15 using X-ray scaling relations and the DES science verification dataset. Many other studies (e.g., [Baxter et al. 2016](#); [Farahi et al. 2016](#); [Simet et al. 2016](#)) adopt a $\sigma_{M|\lambda} \sim 0.2 - 0.3$ dex ([Rozo & Rykoff, 2014](#); [Rozo et al., 2015](#)). These values correspond well to our value of $\sigma_{M|\lambda} = 0.24 \pm 0.09$ dex, and the $0.2 - 0.3$ range corresponds well to the region most sensitively probed in our simulated HETDEX survey (Chapter 2).

The ability of blind spectroscopy to constrain both the absolute cluster mass scale and, more importantly, the amount of scatter at fixed optical richness to values similar to other techniques is extremely positive for the potential of HETDEX. As cluster mass estimates become better constrained through the use of ML methods, we can expect to find even tighter constrains on the optical richness-cluster mass relation. This should lead to excellent calibration of other large-area sky surveys which produce optical photometry only. In addition, it will serve as an important, independent check on other observable-cluster mass relationships which are often noisy and subject to large systematic uncertainties (e.g., [Sereno & Ettori 2015](#)).

4. SUMMARY AND FUTURE WORK

This thesis represents the culmination of the work done over the past four years, and this final chapter summarizes the lessons learned. Over the coming years, the amount of multi-band imaging of the night sky will grow tremendously. The study of galaxy clusters will certainly benefit from the large array of data, but only if we are able to combine datasets in a meaningful way. This combination will push the boundaries of our knowledge of cluster physics, clusters in their role as cosmological probes, and the usefulness of advanced data analysis techniques. It is the author's hope that this thesis has contributed to this push forward.

We begin by a summary of the two studies presented here. We, then, present a small discuss of different projects possible with a survey like HETDEX, and close with a few questions which remain under active investigation.

4.1 Summary

In Chapter 2, we present detailed simulations of the upcoming HETDEX survey's applicability to the detection and total mass measurement of galaxy clusters. Using mock galaxy catalogs and HETDEX-like observational strategies and limits, we observe our simulated sky, estimate the number of clusters observed, and derive basic cluster parameters, redshift, line-of-sight velocity dispersion (LOSVD). Using a traditional power law-based, velocity dispersion, scaling relation along with more advanced probability and machine learning (ML) techniques, we estimate each cluster's total mass. We discuss each cluster mass estimate's precision, and discuss HETDEX's ability to constrain the cosmological parameter $\sigma_8 h^{-1}$ based on those predicted cluster masses. In addition, we comment on how HETDEX may improve current and future photometric large-area sky surveys' cluster mass estimates derived

from optical richness.

Our main conclusions are the following:

1. After considering HETDEX’s observational limits, we find 14,189 clusters with at least five cluster members in the HETDEX survey volume. Of those, 1,760 clusters are detected with HETDEX-like survey observations. The number of cluster members recovered with Survey observations is almost exactly 4.5 times fewer than a fully Targeted survey, across both a wide range of redshifts and cluster masses.
2. We find a traditional power law conversion from LOSVD to cluster mass predicts the true cluster mass with little bias or scatter for clusters $\text{Log } M/M_{\odot} = 14.5$ and above. Below this mass the bias and scatter rapidly increases. In contrast, the probability based and ML based cluster mass estimators are able to predict cluster mass with similar or smaller scatter across all cluster masses. The scatter further decreases when the probability based and ML estimators are combined with other cluster observables besides the LOSVD. For HETDEX-like observations and clusters with $13 < \text{Log } M/M_{\odot} < 14.5$, we find the $\text{ML}_{\sigma,z,N_{gal}}$ method results in the smallest scatter. Below $\text{Log } M/M_{\odot} = 13$ no method with Survey observations gives a bias of less than 50%. For the highest mass clusters the power law method gives the lowest bias and scatter. In short, no single method is superior in all regards. The technique should be chosen to minimize the desired systematic, but we find $\text{ML}_{\sigma,z,N_{gal}}$ provides the best performance across the large range of cluster masses, and observation strategies.
3. In general, we find that the measured scatter of cluster masses decreases when considering Targeted versus Survey observations. Clusters at all masses can

benefit from targeted follow-up observations, although the accuracy gain will be smaller than can be achieved from cluster mass prediction method changes. Targeted follow-up observations reduces the measured scatter by $\sim 10\%$ when comparing like recovery methods.

4. The $\sim 51\%$ cluster mass accuracy of Survey observations places approximately a 20% constraint on $\sigma_8 h^{-1}$. This can be tightened to approximately 12% with follow-up targeted observations. Most importantly, the observations from HETDEX will provide systematics checks on other studies, ultimately improving all future measurements of $\sigma_8 h^{-1}$
5. HETDEX will be able to place important, independent constraints on the amount of scatter in the optical richness-mass relationship. It will to a less extent constrain the overall normalization of the relation. This should provide an important tool in the calibration of large-area sky surveys which rely on photometric data only to estimate cluster masses.

In Chapter 3, we carry out a proof-of-concept study where we present integral field unit observations with the Mitchell Spectrograph of ten intermediate redshift ($z = 0.2 - 0.3$) galaxy clusters. We observe cluster member galaxies within $R \sim 0.5$ Mpc of each cluster, and determine each cluster's membership based on the line-of-sight velocity of each galaxy. The mass of each cluster is determined through a traditional PL and through a machine learning based approach. We use these estimates of cluster mass to measure the absolute mass scale and intrinsic scatter of the optical richness-cluster mass relationship. The goal of this study is to investigate how a blind spectroscopic survey, such as the forthcoming HETDEX, will be able to predict cluster masses, and then to use those masses to help calibrate other observable-cluster mass scaling relations. Our main results are as follows:

- Using a PL scaling relation between the measured line-of-sight velocity dispersion and cluster mass, our low richness ($\lambda < 15$) sample of galaxy clusters have total inferred masses $\sim 0.5 \times 10^{14} M_{\odot}$ (M_{200c}), and the high richness ($\lambda > 60$) cluster sample has total masses $(1.58 - 17.37) \times 10^{14} M_{\odot}$ (M_{200c}). The majority of these estimate are consistent with other published total mass estimates which use a variety of estimation techniques.
- The machine learning based approach of galaxy cluster mass estimation, while powerful, requires a deep understanding of both the machine learning algorithms available, training sets that accurately represent the properties of the data, and expert knowledge of the problem domain. To estimate the total masses of the galaxy clusters in our sample using machine learning methods, the native Buzzard catalogs do not provide a suitable training set due to the limited cosmological volume simulated at low redshift. For the redshift range of our cluster sample, the Buzzard catalogs lack similar high line-of-sight velocity dispersion and high mass clusters. This leads to a severe down-weighting of high mass galaxy clusters when the cluster redshift is included as a training feature. When this feature is removed, the machine learning estimated cluster masses improve but are still underestimated due to too few very high mass clusters being included in the simulated volume. A suite of training data drawn from a similarly sized cosmological volume is critical to the reliable prediction of cluster masses. When this is available, the machine learning predicted cluster masses show less bias and lower scatter compared to a traditional power law scaling relation based on velocity dispersion alone.
- We fit a optical richness-cluster mass relation to the eight high richness ($\lambda > 60$)

clusters. This gives:

$$\text{Log } M_{200c}/\text{M}_\odot = 1.25 \pm 0.78 \text{ Log } \lambda + 12.29 \pm 1.68. \quad (4.1)$$

We are unable to place tight constraints on the overall estimate of the normalization due to the relatively few clusters included. We do estimate the scatter in cluster mass at fixed richness, $\sigma_{M|\lambda} \sim 0.25$. This estimate of scatter compares well with other recent studies of the richness-mass relation. This suggests that a blind spectroscopic survey such as HETDEX will be able to provide a crucial, independent measurement of this scatter, to a much higher precision than is possible in this work. This bodes well for the success of HETDEX as not only a high redshift galaxy survey but as an important calibration tool for understanding the uncertainties associated with galaxy cluster mass estimates.

4.2 Other Potential Investigations

4.2.1 *Investigation of Cluster Miscentering*

Misidentification of the cluster center (due to the mass distribution not being directly observable) can add significant error to the estimate of its mass, and remain a significant challenge for optical mass estimates (e.g., [Duarte & Mamon 2015](#)). Fortunately, hierarchical growth suggests the brightest cluster galaxy (BCG) should be located at the center of the cluster's potential well. Unfortunately, this is not always the case (e.g., [Skibba et al. 2011](#)). When there is no clear central galaxy or the brightest (most massive) galaxy is difficult to identify, the centroid of the hot intracluster medium or a weighted centroid of the member galaxy positions (e.g., [George et al. 2012](#)) can be used.

Many optical, photometry-based cluster finding algorithms (e.g., redMaPPer)

assume a massive cD galaxy is present in each cluster, which gives a success rate of approximately 85% and is described as the “least bad” option for identifying the cluster center. The remaining 15% of clusters often lack a defined center because the cluster’s BCG does not match the expected color of a massive, elliptical galaxy. Specifically, cool-core clusters can have blue, star-forming central galaxies, confusing the cluster center determination.

Star-forming central galaxies are most common in clusters at the lowest end of the halo mass function, which coincide with the majority of clusters in the universe, or in clusters with increasing redshift (the Butcher-Oemler effect). To help correct this issue, targeted observations with HETDEX’s VIRUS instrument could potentially identify the center of motion through the observed dynamics of the member galaxies. This is insensitive to the type of central galaxy and could provide additional clues to optically select central galaxies which do not match the predicted color. Given a large enough sample, a statistical approach will be very powerful.

4.2.2 The Search for Clusters above $z \sim 1$

The identification of galaxy clusters in the low- z universe through optical imaging often relies on a well defined red sequence of cluster galaxies (e.g., redMaPPer). Beyond $z = 1$ the this becomes increasingly hard due to the depth required and the increasing lack of well defined red sequence. Therefore, new methods to search for and identify clusters in the early universe with optical/NIR imaging must be adopted.

The search for clusters in point data (e.g., RA, DEC, z) is not unique to astronomy and, as such, many methods (k-means, mixture models, etc.) have been developed to tackle the problem. [Dehghan & Johnston-Hollitt \(2014\)](#) used one such data agnostic machine learning algorithm, the Density-Based Spatial Clustering of Applications

with Noise (DBSCAN; [Ester et al. 1996](#)), to search for clusters, groups, and filaments in the Extended Chandra Deep Field South. They successfully identified structures at $z < 1$ using a ground based spectroscopic survey and the MUSYC photometric catalog. The HETDEX spectroscopic data could provide improved distance estimates for many potential galaxy clusters, and combined with modern clustering algorithms, such as Ordering Points To Identify the Clustering Structure (OPTICS; [Ankerst et al. 1999](#)) or a hierarchical version of DBSCAN (HDBSCAN; [Campello et al. 2013](#)), which are designed to address the weaknesses of DBSCAN, could provide important insights into the optimization of cluster finding at high redshift. Such advanced clustering searches can also be extended to the large sky-area of PanSTARRS to search for dwarf galaxies or other stellar associations and will eventually be useful to the large-area survey of WFIRST-AFTA. Ultimately, such a study could aid in the development and application of data agnostic machine learning to astronomy, provide improved cluster detection at all redshifts, and suggest potential followup targets requiring the *James Webb Space Telescope*.

4.2.3 Outstanding Questions

The work presented here is only a small piece in the effort to understand how a blind spectroscopic survey could impact the role of galaxy clusters as cosmological probes. As with any study, outstanding questions remain. Here are two potential followup investigations:

- A deep study and optimization of the machine learning methods used to predict cluster masses. There are many machine learning algorithms which are capable of combining many cluster observables to predict a cluster mass. In addition, each method has a series of hyper-parameters which can greatly impact the method’s performance from one data set to another, and from one

potential problem to another. A deep investigation of an appropriate way to combine observational parameters, which parameters to combine, could provide an enormous amount of insight into the best follow up observations, and greatly improve predicted cluster masses. [Acquaviva \(2016\)](#) conducted a similar study for the estimation of galaxy metallicity. A similar study for HETDEX applications would be extremely valuable.

- Impact of cluster contamination on the machine learning predicted masses.

In our simulated HETDEX survey, we assume that we have knowledge of a cluster’s member galaxies, and so this initial work is not effected by the presence of interloping galaxies. A study of how the sparse spatial sampling, and the presence of interloping galaxies (e.g., [Ntampaka et al. 2015b](#)) could be mitigated by machine learning, or another method, is extremely important. Such a study will be required to estimate the best possible cluster masses when HETDEX begins taking data.

Of course, there is also the deep study of the physics surrounding the clusters themselves, through the study of the ICM (e.g., [Mantz et al. 2015](#)), any active galactic nuclei discovered (e.g., [Kirk et al. 2015; Sobral et al. 2015](#)), correlations with other observations (e.g., [Pipino & Pierpaoli 2010](#)), tests for substructure (e.g., [Yu et al. 2015](#)), and many others.

We provide all of the code used to conduct this study at <https://github.com/boada>. Large file size prevents including the source data with the analysis routines. The authors are happy to provide them, if requested.

REFERENCES

- Abell, G. O. 1958, ApJS, 3, 211
- Acquaviva, V. 2016, MNRAS, 456, 1618
- Acquaviva, V., Gawiser, E., Leung, A. S., & Martin, M. R. 2014, Proc. IAU, 10, 365
- Alam, S., Albareti, F. D., Prieto, C. A., et al. 2015, ApJS, 219, 12
- Allen, S. W., Evrard, A. E., & Mantz, A. B. 2011, Annu. Rev. Astron. Astrophys., 49, 409
- Ankerst, M., Breunig, M. M., Kriegel, H.-P., & Sander, J. 1999, ACM Sigmod Rec., 49
- Applegate, D. E., von der Linden, A., Kelly, P. L., et al. 2014, MNRAS, 439, 48
- Bahcall, N. A. 1977, Annu. Rev. Astron. Astrophys., 15, 505
- Balogh, M. L., Navarro, J. F., & Morris, S. L. 2000, ApJ, 540, 113
- Baxter, E. J., Rozo, E., Jain, B., Rykoff, E., & Wechsler, R. H. 2016, eprint arXiv:1604.00048, 7
- Beers, T. C., Flynn, K., & Gebhardt, K. 1990, AJ, 100, 32
- Behroozi, P. S., Wechsler, R. H., & Wu, H.-Y. 2013, ApJ, 762, 109
- Blanc, G. a., Weinzierl, T., Song, M., et al. 2013, AJ, 145, 138
- Blanton, M. R., Dalcanton, J., Eisenstein, D., et al. 2001, AJ, 121, 2358
- Bocquet, S., Saro, A., Mohr, J. J., et al. 2015, ApJ, 799, 214
- Bonamente, M., Landry, D., Maughan, B., et al. 2012, MNRAS, 428, 2812
- Bond, J. R., Efstathiou, G., Lubin, P. M., & Meinholt, P. R. 1991, Phys. Rev. Lett., 66, 2179
- Campello, R. J. G. B., Moulavi, D., & Sander, J. 2013in , 160–172
- Carlstrom, J. E., Holder, G. P., & Reese, E. D. 2002, Annu. Rev. Astron. Astrophys.,

- 40, 643
- Carlstrom, J. E., Ade, P. A. R., Aird, K. A., et al. 2011, PASP, 123, 568
- Caruana, R., & Niculescu-Mizil, A. 2006, in Proc. 23rd Int. Conf. Mach. Learn. - ICML '06, ACM (New York, New York, USA: ACM Press), 161–168
- Chabrier, G. 2003, PASP, 115, 763
- Colless, M., Dalton, G., Maddox, S., et al. 2001, MNRAS, 328, 1039
- Connelly, J. L., Wilman, D. J., Finoguenov, A., et al. 2012, ApJ, 756, 139
- Crawford, S. M., Wirth, G. D., & Bershadsky, M. A. 2014, ApJ, 786, 30
- Crocce, M., Pueblas, S., & Scoccimarro, R. 2006, MNRAS, 373, 369
- Dark Energy Survey Collaboration, D. E. S., Abbott, T., Abdalla, F. B., et al. 2016, MNRAS, 460, 1270
- de Haan, T., Benson, B. A., Bleem, L. E., et al. 2016, eprint arXiv:1603.06522, arXiv:1603.06522
- Dehghan, S., & Johnston-Hollitt, M. 2014, AJ, 147, 52
- Duarte, M., & Mamon, G. A. 2015, MNRAS, 453, 3849
- Eisenhardt, P. R. M., Brodwin, M., Gonzalez, A. H., et al. 2008, ApJ, 684, 905
- Eisenstein, D. J., Zehavi, I., Hogg, D. W., et al. 2005, ApJ, 633, 560
- Ester, M., Kriegel, H. P., Sander, J., & Xu, X. 1996, in Second Int. Conf. Knowl. Discov. Data Min. (AAAI Press), 226–231
- Ettori, S., Tozzi, P., Borgani, S., & Rosati, P. 2003, Astron. Astrophys., 417, 13
- Evrard, A. E., Bialek, J., Busha, M., et al. 2008, ApJ, 672, 122
- Fadda, D., Girardi, M., Iuricin, G., Mardirossian, F., & Mezzetti, M. 1996, ApJ, 473, 670
- Farahi, A., Evrard, A. E., Rozo, E., Rykoff, E. S., & Wechsler, R. H. 2016, eprint arXiv:1601.05773, arXiv:1601.05773
- Finoguenov, A., Reiprich, T. H., & Böhringer, H. 2001, Astron. Astrophys., 368, 749

- Foreman-Mackey, D., Hogg, D. W., Lang, D., & Goodman, J. 2013, PASP, 125, 306
- Foreman-Mackey, D., Ryan, G., Barbary, K., et al. 2016, doi:10.5281/zenodo.45906
- Geller, M. J., Diaferio, A., Rines, K. J., & Serra, A. L. 2013, ApJ, 764, 58
- George, M. R., Leauthaud, A., Bundy, K., et al. 2012, ApJ, 757, 2
- Gonzalez, A. H., Zaritsky, D., & Zabludoff, A. I. 2007, ApJ, 666, 147
- Goodman, J., & Weare, J. 2010, Commun. Appl. Math. Comput. Sci., 5, 65
- Gott, J. R. I., & Rees, M. J. 1975, A&A, 45, 365
- Gunn, J. E., & Gott, J. Richard, I. 1972, ApJ, 176, 1
- Hill, G. J., MacQueen, P. J., Smith, M. P., et al. 2008a, in Ground-based Airborne Instrum. Astron. II. Ed. by McLean, ed. I. S. McLean & M. M. Casali, Vol. 7014, 701470–701470–15
- Hill, G. J., Gebhardt, K., Komatsu, E., et al. 2008b, Panor. Views Galaxy Form. Evol. ASP Conf. Ser., 399
- Hill, G. J., Tuttle, S. E., Lee, H., et al. 2012, in Ground-based Airborne Instrum. Astron. IV. Proc. SPIE, ed. I. S. McLean, S. K. Ramsay, & H. Takami, Vol. 8446, 84460N
- Hoekstra, H., Mahdavi, A., Babul, A., & Bildfell, C. 2012, MNRAS, 427, 1298
- Hogg, D. 1999, Arxiv Prepr. astro-ph/9905116, 1, 1
- Hogg, D. W., Bovy, J., & Lang, D. 2010, eprint arXiv:1008.4686, arXiv:1008.4686
- Hou, A., Parker, L. C., Harris, W. E., & Wilman, D. J. 2009, ApJ, 702, 1199
- Hu, W., & Kravtsov, A. V. 2003, ApJ, 584, 702
- Hubble, E., & Humason, M. L. 1931, ApJ, 74, 43
- Hubble, E. P. 1926, ApJ, 64, 321
- Husemann, B., Kamann, S., Sandin, C., et al. 2012, A&A, 545, A137
- Kelz, A., Jahn, T., Haynes, D., et al. 2014, in Proc. SPIE, ed. S. K. Ramsay, I. S. McLean, & H. Takami, Vol. 9147, 914775

- Kirk, B., Hilton, M., Cress, C., et al. 2015, MNRAS, 449, 4010
- Kravtsov, A. V., & Borgani, S. 2012, Annu. Rev. Astron. Astrophys., 50, 353
- Kurtz, M. J., & Mink, D. J. 1998, PASP, 110, 934
- Kurtz, M. J., Mink, D. J., Wyatt, W. F., et al. 1992, Astron. Data Anal. Softw. Syst. I, 25
- Lemson, G., & The Virgo Consortium. 2006, eprint arXiv:astro-ph/0608019, arXiv:0608019
- Li, R., Shan, H., Kneib, J.-P., et al. 2016, MNRAS, 458, 2573
- LSST Dark Energy Science Collaboration. 2012, arXiv Prepr. arXiv1211.0310, 133
- Mantz, A., Allen, S. W., Rapetti, D., & Ebeling, H. 2010, MNRAS, 406, no
- Mantz, A. B., Allen, S. W., Morris, R. G., et al. 2015, MNRAS, 449, 199
- Mehrten, N., Romer, A. K., Hilton, M., et al. 2012, MNRAS, 423, 1024
- Meinshausen, N. 2006, J. Mach. Learn. Res., 7, 983
- Merloni, A., Predehl, P., Becker, W., et al. 2012, eprint arXiv:1209.3114, 84
- Milvang-Jensen, B., Noll, S., Halliday, C., et al. 2008, A&A, 482, 419
- Mohri, M., Rostamizadeh, A., & Talwalkar, A. 2012, Foundations of Machine Learning (MIT Press), 412
- Munari, E., Biviano, A., Borgani, S., Murante, G., & Fabjan, D. 2013, MNRAS, 430, 2638
- Muriel, H., Quintana, H., Infante, L., Lambas, D. G., & Way, M. J. 2002, AJ, 124, 1934
- Murphy, J. D., Gebhardt, K., & Adams, J. J. 2011, ApJ, 729, 129
- Murray, S., Power, C., & Robotham, A. 2013, Astron. Comput., 3-4, 23
- Neal, R. M. 1997, Markov Chain Monte Carlo Methods Based on ‘Slicing’ the Density Function, Tech. Rep. 9722, Department of Statistics, University of Toronto, Toronto, doi:10.1.1.48.886

- Ntampaka, M., Trac, H., Sutherland, D. J., et al. 2015a, ApJ, 803, 50
- . 2015b, eprint arXiv:1509.05409, arXiv:1509.05409
- Oke, J. B. 1974, ApJS, 27, 21
- Old, L., Gray, M. E., & Pearce, F. R. 2013, MNRAS, 434, 2606
- Papovich, C. 2008, ApJ, 676, 206
- Papovich, C., Finkelstein, S. L., Ferguson, H. C., Lotz, J. M., & Giavalisco, M. 2011, MNRAS, 412, 1123
- Pedregosa, F., Varoquaux, G., Gramfort, A., et al. 2012, J. Mach. Learn. Res., 12, 2825
- Pillepich, A., Porciani, C., & Reiprich, T. H. 2012, MNRAS, 422, 44
- Pipino, A., & Pierpaoli, E. 2010, MNRAS, 404, 16
- Planck Collaboration. 2013, A&A, 571, 19
- Press, W. H., & Schechter, P. 1974, ApJ, 187, 425
- Quintana, H., Carrasco, E. R., & Reisenegger, A. 2000, AJ, 120, 511
- Reddick, R. M., Wechsler, R. H., Tinker, J. L., & Behroozi, P. S. 2013, ApJ, 771, 30
- Ripley, B. D. 2007, Pattern recognition and neural networks (Cambridge university press)
- Robotham, A. S. G., Norberg, P., Driver, S. P., et al. 2011, MNRAS, 416, 2640
- Rozo, E., & Rykoff, E. S. 2014, ApJ, 783, 80
- Rozo, E., Rykoff, E. S., Bartlett, J. G., & Evrard, A. 2013, MNRAS, 438, 49
- Rozo, E., Rykoff, E. S., Bartlett, J. G., & Melin, J.-B. 2015, MNRAS, 450, 592
- Rozo, E., Wu, H.-Y., & Schmidt, F. 2011, ApJ, 735, 118
- Rozo, E., Wechsler, R. H., Rykoff, E. S., et al. 2010, ApJ, 708, 645
- Ruel, J., Bazin, G., Bayliss, M., et al. 2014, ApJ, 792, 45
- Rykoff, E. S., Koester, B. P., Rozo, E., et al. 2012, ApJ, 746, 178
- Rykoff, E. S., Rozo, E., Busha, M. T., et al. 2014, ApJ, 785, 104

- Rykoff, E. S., Rozo, E., Hollowood, D., et al. 2016, ApJS, 224, 1
- Sandin, C., Becker, T., Roth, M. M., et al. 2010, A&A, 515, A35
- Saro, A., Mohr, J. J., Bazin, G., & Dolag, K. 2013, ApJ, 772, 47
- Saro, A., Bocquet, S., Rozo, E., et al. 2015, MNRAS, 454, 2305
- Sehgal, N., Trac, H., Acquaviva, V., et al. 2011, ApJ, 732, 44
- Sereno, M., & Ettori, S. 2015, MNRAS, 450, 3633
- Sharp, R., & Birchall, M. N. 2010, Publ. Astron. Soc. Aust., 27, 91
- Shetrone, M., Martell, S. L., Wilkerson, R., et al. 2010, AJ, 140, 1119
- Sifón, C., Hoekstra, H., Cacciato, M., et al. 2015, A&A, 575, A48
- Sifón, C., Menanteau, F., Hasselfield, M., et al. 2013, ApJ, 772, 25
- Sifón, C., Battaglia, N., Hasselfield, M., et al. 2016, MNRAS, stw1284
- Simet, M., McClintock, T., Mandelbaum, R., et al. 2016, eprint arXiv:1603.06953, arXiv:1603.06953
- Simon, P. 2013, Too Big to Ignore: The Business Case for Big Data, Wiley and SAS Business Series (Wiley)
- Skibba, R. A., van den Bosch, F. C., Yang, X., et al. 2011, MNRAS, 410, 417
- Smith, S. 1936, ApJ, 83, 23
- Sobral, D., Stroe, A., Dawson, W. A., et al. 2015, MNRAS, 450, 630
- Spergel, D. N., Verde, L., Peiris, H. V., et al. 2003, ApJS, 148, 175
- Springel, V. 2005, MNRAS, 364, 1105
- Springel, V., White, S. D. M., Jenkins, A., et al. 2005, Nature, 435, 629
- Stanford, S. A., Eisenhardt, P. R., & Dickinson, M. 1998, ApJ, 492, 461
- Sunyaev, R. A., & Zeldovich, Y. B. 1972, Comments Astrophys. Sp. Phys., 4
- Swetz, D. S., Ade, P. A. R., Amiri, M., et al. 2011, ApJS, 194, 41
- The Dark Energy Survey Collaboration. 2005, eprint arXiv:astro-ph/0510346, 42
- Tin Kam Ho. 1995, in Proc. 3rd Int. Conf. Doc. Anal. Recognit., Vol. 1, IEEE (IEEE

- Comput. Soc. Press), 278–282
- Tin Kam Ho. 1998, IEEE Trans. Pattern Anal. Mach. Intell., 20, 832
- Tinker, J., Kravtsov, A. V., Klypin, A., et al. 2008, ApJ, 688, 709
- Tonry, J., & Davis, M. 1979, AJ, 84, 1511
- van Albada, G. B. 1960, Bull. Astron. Institutes Netherlands, 15, 165
- . 1961, AJ, 66, 590
- van der Burg, R. F. J., Muzzin, A., Hoekstra, H., et al. 2014, A&A, 561, A79
- Vanderlinde, K., Crawford, T. M., de Haan, T., et al. 2010, ApJ, 722, 1180
- Vikhlinin, A., Burenin, R. A., Ebeling, H., et al. 2009, ApJ, 692, 1033
- Voit, G. M. 2005, Rev. Mod. Phys., 77, 207
- Walker, M. G., Mateo, M., Olszewski, E. W., et al. 2006, AJ, 131, 2114
- Weinberg, D. H., Mortonson, M. J., Eisenstein, D. J., et al. 2013, Phys. Rep., 530, 87
- White, M., Cohn, J. D., & Smit, R. 2010, MNRAS, 408, 1818
- White, S. D. M., & Rees, M. J. 1978, MNRAS, 183, 341
- Wilman, D. J., Balogh, M. L., Bower, R. G., et al. 2005, MNRAS, 358, 71
- Wing, J. D., & Blanton, E. L. 2013, ApJ, 767, 102
- Xu, X., Ho, S., Trac, H., et al. 2013, ApJ, 772, 147
- Yu, H., Serra, A. L., Diaferio, A., & Baldi, M. 2015, ApJ, 810, 37
- Zwicky, F. 1933, Helv. Phys. Acta, 6, 110

APPENDIX A

MS OBSERVATIONS

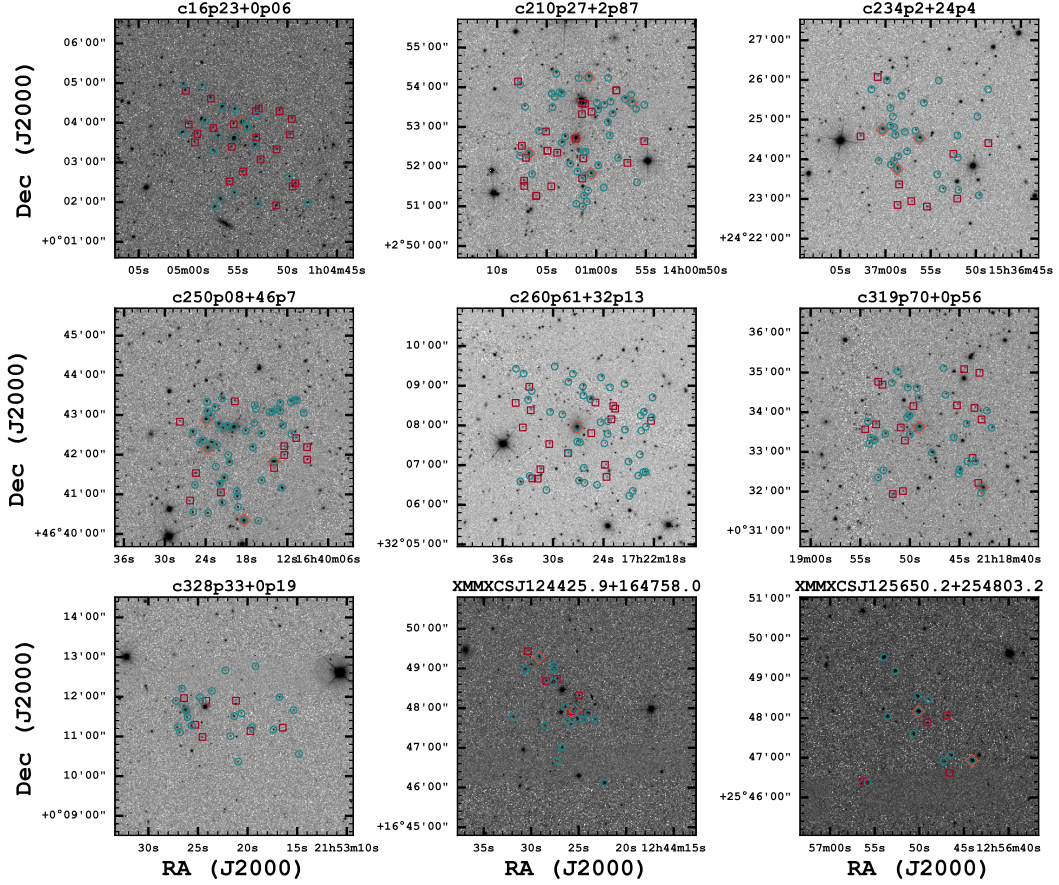


Figure A.1: SDSS r image of cluster c203p83+41p0. The symbols show the position of observed galaxies. Blue circles indicate galaxies with $Q = 0$ or $Q = 1$ spectroscopic redshifts, red squares indicate galaxies where a redshift could not be reliably determined, and the orange diamond corresponds to galaxies with pre-existing redshifts from the SDSS. *Right:* Example spectrum of an emission-line cluster galaxy (black line) and template fit (red line) from VIRUS-P on the McDonald 2.7m telescope. The spectrum shows the wavelength range and data quality expected from HETDEX-like spectroscopy, which are sufficient to measure galaxy redshifts.

Table A.1: Spectroscopic redshifts for galaxies in MSJ010455.4+000336.3 measured with the MS: Columns as in Table 3.2.

tile (1)	dither (2)	fiber (3)	ra (4)	dec (5)	r (mag) (6)	redshift (7)	Q (8)	Member (9)	R (Mpc) (10)	LOSV (km s ⁻¹) (11)
NE	1	223	01:04:56.937	+00:03:39.60	19.38	0.2691±0.0002	0	✓	0.10	-748±89
NE	2	42	01:05:00.449	+00:04:57.41	19.80	0.2766±0.0001	1	✓	0.47	1005±52
NE	2	168	01:04:58.247	+00:04:02.62	19.75	0.3054±0.0003	1	...	0.23	7783±122
NE	2	216	01:05:00.487	+00:03:44.70	18.85	0.0826±0.0004	1	...	0.12	-44576±193
NE	2	220	01:04:55.367	+00:03:36.34	17.27	0.2715±0.0001	0	✓	0.00	-193±61
NE	3	38	01:04:58.559	+00:04:55.13	19.95	0.3510±0.0001	1	...	0.46	18494±56
NE	3	106	01:04:56.545	+00:04:23.15	18.36	0.2788±0.0001	0	✓	0.21	1517±47
NE	3	118	01:04:55.276	+00:04:19.53	19.49	0.2747±0.0001	0	✓	0.18	566±71
NE	3	160	01:04:54.563	+00:04:00.66	18.19	0.2747±0.0001	0	✓	0.11	559±52
NW	1	156	01:04:53.064	+00:04:10.99	20.22	0.2234±0.0001	1	...	0.18	-11495±52
NW	2	173	01:04:54.217	+00:04:02.78	19.62	0.2629±0.0002	0	✓	0.13	-2205±80
NW	3	187	01:04:54.051	+00:03:52.42	19.35	0.3290±0.0001	1	...	0.12	13319±52
SE	1	50	01:04:57.440	+00:03:17.71	19.51	0.2718±0.0002	1	✓	0.15	-123±75
SE	2	191	01:04:55.332	+00:02:14.18	19.79	0.2794±0.0001	0	✓	0.35	1658±66
SE	3	208	01:04:56.734	+00:02:05.07	18.75	0.2781±0.0001	0	✓	0.40	1358±42
SE	3	238	01:04:57.284	+00:01:53.04	19.58	0.2705±0.0001	0	✓	0.45	-421±66
SW	2	26	01:04:53.268	+00:03:26.04	18.99	0.2666±0.0002	0	✓	0.14	-1352±85
SW	2	135	01:04:49.814	+00:02:38.18	20.10	0.2697±0.0002	1	✓	0.42	-619±85
SW	2	218	01:04:47.988	+00:01:59.05	19.55	0.2627±0.0001	1	✓	0.60	-2259±42
SW	3	228	01:04:52.934	+00:01:56.95	20.37	0.2763±0.0001	1	✓	0.45	928±47

Table A.2: Spectroscopic redshifts for galaxies in MSJ153656.3+242431.6 measured with the MS: Columns as in Table 3.2

tile (1)	dither (2)	fiber (3)	ra (4)	dec (5)	r (mag) (6)	redshift (7)	Q (8)	Member (9)	R (Mpc) (10)	LOSV (km s ⁻¹) (11)
NE	1	78	15:36:58.192	+24:25:36.14	19.81	0.3228±0.0001	0	...	0.33	23652±44
NE	1	124	15:36:59.468	+24:25:17.76	19.83	0.2324±0.0004	1	✓	0.24	1609±195
NE	1	208	15:36:57.848	+24:24:41.47	20.35	0.1881±0.0001	0	...	0.08	-9197±34
NE	2	11	15:37:00.861	+24:26:04.40	20.48	0.0947±0.0001	1	...	0.20	-31965±54
NE	2	153	15:36:59.174	+24:25:04.55	20.37	0.1036±0.0002	1	...	0.10	-29809±98
NE	2	232	15:37:02.759	+24:24:34.63	19.98	0.3017±0.0001	1	...	0.40	18513±49
NE	3	23	15:36:59.839	+24:25:59.51	18.05	0.1275±0.0000	0	...	0.23	-23979±20
NE	3	55	15:37:01.554	+24:25:45.67	19.79	0.2115±0.0001	1	...	0.36	-3477±49
NE	3	181	15:36:59.035	+24:24:48.56	20.11	0.1874±0.0001	1	...	0.13	-9363±39
NE	3	182	15:36:59.498	+24:24:50.78	19.62	0.1231±0.0003	1	...	0.11	-25050±151
NE	3	191	15:36:56.681	+24:24:43.40	19.54	0.1808±0.0000	0	...	0.04	-10980±24
NE	3	198	15:37:00.334	+24:24:44.60	17.27	0.2274±0.0002	0	✓	0.21	387±112
NE	3	210	15:36:58.911	+24:24:37.07	19.67	0.4813±0.0000	1	...	0.22	62324±24
NE	3	219	15:36:56.253	+24:24:31.59	17.36	0.2262±0.0001	0	✓	0.00	94±63
NW	1	116	15:36:55.756	+24:25:25.38	18.90	0.2706±0.0001	1	...	0.23	10924±49
NW	1	148	15:36:49.817	+24:25:04.96	20.02	0.2224±0.0001	0	✓	0.34	-813±63
NW	2	26	15:36:54.106	+24:25:59.10	20.79	0.2298±0.0000	0	✓	0.34	972±24
NW	3	44	15:36:48.628	+24:25:45.78	21.29	0.3341±0.0001	1	...	0.62	26416±59
NW	3	210	15:36:52.024	+24:24:36.09	19.78	0.2281±0.0001	0	✓	0.21	570±63
SE	1	48	15:36:57.612	+24:24:12.18	19.43	0.2215±0.0002	0	✓	0.10	-1038±78
SE	1	64	15:36:58.605	+24:24:04.80	20.06	0.2124±0.0001	1	...	0.15	-3277±59
SE	2	80	15:36:59.058	+24:23:57.63	19.24	0.2280±0.0002	0	✓	0.19	528±93
SE	2	95	15:36:59.393	+24:23:51.85	19.35	0.1244±0.0002	1	...	0.13	-24730±98
SE	3	108	15:36:58.708	+24:23:45.47	17.70	0.2235±0.0002	0	✓	0.21	-565±83
SW	1	66	15:36:52.487	+24:24:08.35	20.29	0.1248±0.0001	1	...	0.13	-24633±63
SW	1	142	15:36:54.270	+24:23:37.37	20.15	0.2546±0.0001	0	...	0.24	7019±54

Table A.2 Continued

tile (1)	dither (2)	fiber (3)	ra (4)	dec (5)	r (mag) (6)	redshift (7)	Q (8)	Member (9)	R (Mpc) (10)	LOSV (km s ⁻¹) (11)
SW	2	185	15:36:53.657	+24:23:15.33	19.58	0.2239±0.0002	0	✓	0.30	-450±98
SW	3	65	15:36:51.996	+24:24:02.62	20.31	0.2201±0.0001	1	✓	0.23	-1382±34

123

Table A.3: Spectroscopic redshifts for galaxies in MSJ164019.8+464241.5 measured with the MS: Columns as in Table 3.2.

tile	dither	fiber	ra	dec	r (mag)	redshift	Q	Member	R (Mpc)	LOSV (km s ⁻¹)	
(1)	(2)	(3)	(4)	(5)	(6)	(7)	(8)	(9)	(10)	(11)	
NE	1	34	16:40:21.617	+46:43:25.07	20.12	0.1014±0.0003	0	...	0.09	-30528±141	
	1	110	16:40:23.879	+46:42:52.76	17.81	0.2333±0.0000	0	✓	0.16	1617±24	
	1	133	16:40:19.812	+46:42:41.30	16.61	0.2238±0.0001	0	✓	0.00	-699±39	
	1	156	16:40:25.818	+46:42:33.87	18.36	0.2099±0.0001	0	...	0.21	-4092±54	
	1	183	16:40:24.352	+46:42:21.79	19.33	0.2248±0.0002	0	✓	0.18	-462±93	
	1	211	16:40:23.651	+46:42:10.01	17.62	0.2287±0.0001	0	✓	0.19	483±39	
	2	65	16:40:22.597	+46:43:10.93	19.73	0.1813±0.0002	1	...	0.13	-11053±88	
	2	81	16:40:23.696	+46:43:04.86	18.62	0.2324±0.0001	0	✓	0.17	1400±68	
	2	95	16:40:23.219	+46:42:58.04	19.32	0.2264±0.0001	0	✓	0.14	-75±39	
	2	122	16:40:22.018	+46:42:46.03	18.84	0.2079±0.0001	0	...	0.08	-4574±73	
	2	136	16:40:21.428	+46:42:39.59	19.11	0.2180±0.0002	0	✓	0.06	-2120±93	
	2	195	16:40:22.346	+46:42:14.63	19.21	0.2289±0.0002	0	✓	0.14	542±93	
	3	37	16:40:23.777	+46:43:19.71	19.22	0.2229±0.0002	0	✓	0.20	-933±102	
	3	120	16:40:20.755	+46:42:43.96	17.82	0.2216±0.0002	0	✓	0.04	-1240±83	
	3	181	16:40:23.067	+46:42:18.32	18.39	0.2191±0.0001	0	✓	0.14	-1852±39	
	3	184	16:40:24.861	+46:42:18.39	19.09	0.2110±0.0002	0	...	0.20	-3816±78	
	NW	1	50	16:40:13.038	+46:43:18.14	19.37	0.2289±0.0002	0	✓	0.29	539±78
	NW	1	79	16:40:13.042	+46:43:06.31	19.12	0.2297±0.0001	0	✓	0.27	730±34
	NW	1	81	16:40:14.572	+46:43:04.50	20.49	0.2249±0.0002	1	✓	0.21	-443±102
	NW	1	128	16:40:16.854	+46:42:48.04	20.31	0.2281±0.0001	1	✓	0.11	342±68
	NW	1	215	16:40:17.060	+46:42:11.27	19.21	0.2580±0.0002	1	...	0.17	7632±122
	NW	2	33	16:40:10.991	+46:43:22.18	19.33	0.2228±0.0001	1	✓	0.36	-940±49
	NW	2	56	16:40:16.794	+46:43:15.13	20.91	0.2350±0.0001	1	✓	0.17	2021±73
	NW	2	70	16:40:16.608	+46:43:09.56	20.70	0.2167±0.0002	1	✓	0.15	-2427±88
	NW	2	81	16:40:14.180	+46:43:05.00	19.20	0.2252±0.0001	0	✓	0.23	-375±68
	NW	2	156	16:40:15.807	+46:42:31.47	18.88	0.2281±0.0002	0	✓	0.16	344±83

Table A.3 Continued

tile	dither	fiber	ra	dec	r (mag)	redshift	Q	Member	R (Mpc)	LOSV (km s ⁻¹)	
(1)	(2)	(3)	(4)	(5)	(6)	(7)	(8)	(9)	(10)	(11)	
NW	3	33	16:40:11.463	+46:43:19.95	19.11	0.2249±0.0002	0	✓	0.34	-426±97	
	3	65	16:40:13.553	+46:43:08.81	20.49	0.1319±0.0001	1	...	0.16	-23097±29	
	3	74	16:40:09.583	+46:43:03.29	20.34	0.1735±0.0001	1	...	0.32	-12967±58	
	3	122	16:40:12.635	+46:42:44.68	19.66	0.2270±0.0001	0	✓	0.27	79±63	
	3	144	16:40:18.116	+46:42:35.97	19.27	0.2080±0.0002	1	...	0.06	-4567±102	
	3	149	16:40:11.390	+46:42:31.31	20.02	0.0844±0.0002	1	...	0.14	-34675±88	
	SE	1	4	16:40:20.674	+46:41:59.40	20.48	0.2341±0.0001	0	✓	0.16	1797±54
	SE	1	50	16:40:22.486	+46:41:42.33	20.51	0.2376±0.0002	1	...	0.25	2670±78
	SE	1	107	16:40:21.903	+46:41:15.96	18.82	0.1866±0.0001	0	...	0.28	-9766±58
	SE	1	147	16:40:19.343	+46:40:57.31	18.39	0.1864±0.0001	0	...	0.33	-9815±34
	SE	1	211	16:40:23.625	+46:40:32.22	19.06	0.2325±0.0001	0	✓	0.50	1410±54
	SE	1	214	16:40:25.819	+46:40:33.21	19.03	0.2272±0.0002	0	✓	0.52	113±93
	SE	2	113	16:40:25.565	+46:41:14.28	20.51	0.2221±0.0002	0	✓	0.38	-1116±83
	SE	2	165	16:40:21.553	+46:40:47.83	18.59	0.2110±0.0001	1	...	0.40	-3819±68
	SE	3	18	16:40:20.484	+46:41:48.57	18.80	0.2347±0.0001	0	✓	0.20	1960±58
	SE	3	77	16:40:21.250	+46:41:25.01	18.21	0.1892±0.0001	0	...	0.25	-9128±29
	SE	3	118	16:40:19.417	+46:41:05.03	19.40	0.2238±0.0002	0	✓	0.35	-701±102
	SE	3	176	16:40:19.231	+46:40:41.13	19.36	0.2167±0.0001	0	...	0.42	-2444±39
	SW	1	122	16:40:12.787	+46:41:09.93	18.22	0.2340±0.0001	0	✓	0.44	1785±34
	SW	1	243	16:40:16.232	+46:40:20.20	20.28	0.2278±0.0002	1	✓	0.53	274±88
	SW	1	246	16:40:18.377	+46:40:20.93	17.51	0.1874±0.0002	0	...	0.44	-9576±107
	SW	2	98	16:40:15.754	+46:41:21.37	20.03	0.2243±0.0001	0	✓	0.33	-572±63
	SW	3	22	16:40:13.962	+46:41:49.44	17.63	0.1107±0.0001	0	...	0.16	-28264±54

Table A.4: Spectroscopic redshifts for galaxies in MSJ140102.0+025242.6 measured with the MS: Columns as in Table 3.2

tile (1)	dither (2)	fiber (3)	ra (4)	dec (5)	r (mag) (6)	redshift (7)	Q (8)	Member (9)	R (Mpc) (10)	LOSV (km s ⁻¹) (11)	
NE	1	6	14:01:04.022	+02:54:20.65	19.01	0.2478±0.0002	0	✓	0.40	-1626±81	
	1	16	14:01:01.771	+02:54:13.80	20.37	0.3158±0.0002	1	...	0.42	14574±81	
	1	123	14:01:04.410	+02:53:29.95	19.70	0.2325±0.0002	1	...	0.22	-5275±119	
	2	43	14:01:07.682	+02:54:03.80	20.20	0.2039±0.0001	1	...	0.40	-12093±33	
	2	64	14:01:03.691	+02:53:52.63	20.48	0.2876±0.0002	1	...	0.32	7854±110	
	2	222	14:01:03.134	+02:52:45.00	18.66	0.2517±0.0002	0	✓	0.07	-699±91	
	3	63	14:01:03.475	+02:53:50.51	18.68	0.2598±0.0002	0	✓	0.29	1217±110	
	3	65	14:01:04.494	+02:53:50.70	20.31	0.2540±0.0002	0	✓	0.31	-149±86	
	3	79	14:01:04.203	+02:53:45.54	20.26	0.2192±0.0001	1	...	0.25	-8444±67	
	3	114	14:01:07.185	+02:53:30.54	20.11	0.2606±0.0002	1	✓	0.37	1405±81	
	3	198	14:01:05.757	+02:52:54.15	19.70	0.2516±0.0002	0	✓	0.23	-737±114	
	3	237	14:01:03.483	+02:52:35.96	18.94	0.3110±0.0001	1	...	0.11	13416±52	
	NW	1	23	14:00:58.786	+02:54:14.18	20.07	0.2318±0.0001	1	...	0.38	-5458±71
	NW	1	92	14:00:57.098	+02:53:42.10	18.42	0.2108±0.0002	0	...	0.32	-10444±119
	NW	1	105	14:00:56.404	+02:53:36.25	18.55	0.2504±0.0002	0	✓	0.39	-1030±91
	NW	1	111	14:00:59.191	+02:53:33.62	19.78	0.2458±0.0002	0	✓	0.25	-2108±105
	NW	2	103	14:00:55.146	+02:53:33.41	21.44	0.1642±0.0003	1	...	0.32	-21563±143
	NW	2	119	14:00:55.968	+02:53:27.36	20.34	0.3084±0.0003	1	...	0.46	12808±129
	NW	2	127	14:00:59.815	+02:53:26.69	19.29	0.2723±0.0001	1	...	0.23	4205±38
	NW	3	13	14:01:00.752	+02:54:14.53	17.96	0.2492±0.0002	1	✓	0.37	-1312±81
	NW	3	62	14:00:56.466	+02:53:49.12	20.53	0.3932±0.0001	1	...	0.57	33012±67
	NW	3	95	14:00:58.558	+02:53:38.37	20.03	0.2363±0.0001	1	...	0.28	-4369±48
	NW	3	98	14:00:59.942	+02:53:37.00	20.63	0.4784±0.0000	1	...	0.37	53304±24
	NW	3	138	14:00:58.352	+02:53:20.29	18.69	0.2557±0.0002	0	✓	0.26	245±100
	NW	3	168	14:00:58.824	+02:53:07.37	18.61	0.2321±0.0001	0	...	0.20	-5375±67
	NW	3	211	14:00:58.625	+02:52:47.07	20.02	0.1463±0.0002	1	...	0.13	-25817±86

Table A.4 Continued

tile	dither	fiber	ra	dec	r (mag)	redshift	Q	Member	R (Mpc)	LOSV (km s ⁻¹)	
(1)	(2)	(3)	(4)	(5)	(6)	(7)	(8)	(9)	(10)	(11)	
126	SE	1	90	14:01:02.616	+02:52:04.19	19.19	0.2639±0.0002	1	✓	0.16	2201±91
	SE	1	234	14:01:02.016	+02:51:03.83	21.20	0.2830±0.0002	1	...	0.42	6738±86
	SE	2	56	14:01:06.778	+02:52:19.68	17.90	0.2249±0.0002	1	...	0.27	-7098±76
	SE	2	72	14:01:07.685	+02:52:16.24	20.08	0.3193±0.0002	0	...	0.42	15401±81
	SE	3	103	14:01:01.894	+02:51:52.53	19.80	0.2437±0.0001	1	✓	0.19	-2625±67
	SE	3	127	14:01:06.471	+02:51:48.78	19.58	0.2726±0.0001	1	...	0.36	4284±71
	SW	1	57	14:01:01.072	+02:52:22.71	20.15	0.1615±0.0002	0	...	0.07	-22207±91
	SW	1	144	14:01:01.183	+02:51:45.62	20.01	0.2670±0.0002	0	✓	0.24	2930±119
	SW	2	58	14:01:01.278	+02:52:21.62	20.96	0.2581±0.0001	1	✓	0.09	821±57
	SW	2	65	14:00:57.802	+02:52:13.21	20.18	0.4127±0.0002	1	...	0.38	37664±86
	SW	2	98	14:00:59.802	+02:52:01.88	19.31	0.2549±0.0002	1	✓	0.21	49±105
	SW	2	148	14:00:55.880	+02:51:36.29	21.24	0.1548±0.0002	1	...	0.30	-23794±119
	SW	2	231	14:01:00.954	+02:51:06.98	20.55	0.3329±0.0001	1	...	0.46	18635±62
	SW	3	128	14:01:00.529	+02:51:49.71	18.25	0.2628±0.0003	1	✓	0.23	1934±153
	SW	3	169	14:00:59.240	+02:51:28.42	21.07	0.4035±0.0001	1	...	0.46	35457±57
	SW	3	187	14:01:00.832	+02:51:23.59	20.68	0.1628±0.0001	1	...	0.23	-21887±52
	SW	3	202	14:01:01.230	+02:51:16.08	19.95	0.2355±0.0002	0	...	0.33	-4560±76
	SW	3	246	14:01:01.370	+02:50:59.59	20.01	0.2207±0.0001	1	...	0.37	-8106±62

Table A.5: Spectroscopic redshifts for galaxies in MSJ172227.2+320757.2 measured with the MS: Columns as in Table 3.2

tile (1)	dither (2)	fiber (3)	ra (4)	dec (5)	r (mag) (6)	redshift (7)	Q (8)	Member (9)	R (Mpc) (10)	LOSV (km s ⁻¹) (11)	
NE	1	21	17:22:29.818	+32:09:29.21	20.20	0.1014±0.0004	0	...	0.18	-30318±200	
	1	29	17:22:34.413	+32:09:25.72	19.68	0.2321±0.0001	0	✓	0.47	1553±34	
	2	32	17:22:27.631	+32:09:18.17	19.76	0.2200±0.0002	0	...	0.29	-1396±78	
	2	62	17:22:28.177	+32:09:05.94	19.38	0.2246±0.0001	1	✓	0.25	-282±34	
	2	179	17:22:28.895	+32:08:16.78	19.86	0.2332±0.0002	1	✓	0.11	1819±93	
	3	42	17:22:33.506	+32:09:18.50	20.35	0.2318±0.0001	1	✓	0.42	1492±44	
	3	73	17:22:26.441	+32:08:58.70	19.12	0.2084±0.0001	0	...	0.21	-4221±34	
	3	98	17:22:32.542	+32:08:52.14	20.50	0.2100±0.0003	1	...	0.30	-3831±161	
	3	102	17:22:26.378	+32:08:45.31	19.76	0.1683±0.0001	0	...	0.14	-14010±44	
	3	128	17:22:32.971	+32:08:38.74	19.34	0.2315±0.0001	1	...	0.31	1419±44	
	3	167	17:22:30.347	+32:08:20.40	19.86	0.2909±0.0002	1	...	0.20	15894±117	
	3	219	17:22:27.184	+32:07:57.25	15.38	0.2226±0.0002	0	✓	0.00	-762±78	
	NW	1	102	17:22:18.160	+32:08:42.50	18.84	0.2228±0.0001	0	✓	0.44	-716±63
	NW	1	200	17:22:24.352	+32:08:04.74	20.42	0.2744±0.0001	1	...	0.15	11881±44
	NW	1	205	17:22:18.953	+32:07:57.82	19.67	0.2275±0.0001	0	✓	0.38	433±44
	NW	2	68	17:22:23.220	+32:08:57.64	21.00	0.2798±0.0002	1	...	0.33	13189±88
	NW	2	116	17:22:25.574	+32:08:39.54	17.80	0.1685±0.0001	0	...	0.14	-13964±54
	NW	2	148	17:22:19.197	+32:08:20.80	18.98	0.2245±0.0001	0	✓	0.38	-304±44
	NW	2	161	17:22:18.289	+32:08:12.33	19.59	0.2203±0.0002	0	✓	0.41	-1318±98
	NW	2	163	17:22:19.559	+32:08:15.27	19.47	0.2143±0.0001	0	...	0.34	-2782±63
	NW	3	26	17:22:24.290	+32:09:12.65	19.16	0.1680±0.0003	0	...	0.24	-14079±137
	NW	3	50	17:22:21.475	+32:09:02.84	19.02	0.2260±0.0002	0	✓	0.36	55±98
	NW	3	184	17:22:23.454	+32:08:06.50	19.96	0.2628±0.0001	1	...	0.20	9047±68
	NW	3	206	17:22:19.500	+32:07:52.06	20.94	0.2185±0.0001	1	✓	0.35	-1753±39
SE	1	202	17:22:33.893	+32:06:35.34	18.68	0.2203±0.0001	1	✓	0.42	-1333±59	
SE	2	91	17:22:28.227	+32:07:18.12	20.29	0.2135±0.0001	0	...	0.14	-2982±63	

Table A.5 Continued

tile	dither	fiber	ra	dec	r (mag)	redshift	Q	Member	R (Mpc)	LOSV (km s ⁻¹)
(1)	(2)	(3)	(4)	(5)	(6)	(7)	(8)	(9)	(10)	(11)
SE	2	189	17:22:26.261	+32:06:33.18	20.64	0.2897±0.0002	1	...	0.37	15599±122
SE	2	226	17:22:30.791	+32:06:22.27	20.60	0.2482±0.0001	1	...	0.41	5478±39
SE	3	45	17:22:27.117	+32:07:35.51	19.77	0.2210±0.0003	0	✓	0.08	-1157±151
SE	3	171	17:22:32.779	+32:06:43.69	20.61	0.2261±0.0000	0	✓	0.37	92±24
SW	1	160	17:22:18.982	+32:06:49.70	19.60	0.2262±0.0001	0	✓	0.45	121±44
SW	1	203	17:22:26.919	+32:06:36.74	18.29	0.2256±0.0002	0	✓	0.29	-30±78
SW	1	214	17:22:24.770	+32:06:30.20	20.93	0.2334±0.0001	1	✓	0.34	1880±68
SW	2	121	17:22:21.021	+32:07:05.24	19.59	0.2293±0.0002	0	✓	0.35	882±78
SW	3	5	17:22:21.443	+32:07:53.68	19.98	0.1781±0.0002	0	...	0.22	-11617±117
SW	3	23	17:22:23.499	+32:07:47.19	19.62	0.1771±0.0001	0	...	0.14	-11852±29
SW	3	53	17:22:23.894	+32:07:32.82	20.45	0.3593±0.0001	1	...	0.24	32587±29
SW	3	58	17:22:26.813	+32:07:34.55	19.46	0.2238±0.0001	0	✓	0.08	-474±68
SW	3	89	17:22:19.677	+32:07:15.96	19.83	0.2258±0.0001	0	✓	0.38	21±63
SW	3	144	17:22:26.332	+32:06:55.93	20.24	0.2292±0.0001	1	✓	0.23	845±73
SW	3	146	17:22:19.254	+32:06:49.42	19.04	0.2258±0.0001	0	✓	0.44	18±59
SW	3	162	17:22:19.860	+32:06:44.09	19.95	0.3840±0.0001	1	...	0.62	38622±73
SW	3	221	17:22:20.506	+32:06:21.01	19.35	0.2242±0.0002	0	✓	0.46	-372±78
SW	3	236	17:22:20.911	+32:06:13.52	20.04	0.1851±0.0001	1	...	0.41	-9900±39

Table A.6: Spectroscopic redshifts for galaxies in MSJ211849.1+003337.3 measured with the MS: Columns as in Table 3.2

tile (1)	dither (2)	fiber (3)	ra (4)	dec (5)	r (mag) (6)	redshift (7)	Q (8)	Member (9)	R (Mpc) (10)	LOSV (km s ⁻¹) (11)	
NE	1	193	21:18:50.285	+00:33:52.08	20.09	0.2785±0.0002	0	✓	0.10	633±112	
	1	216	21:18:54.243	+00:33:45.76	19.71	0.2765±0.0001	0	✓	0.33	169±66	
	2	220	21:18:49.071	+00:33:37.32	17.42	0.2756±0.0001	0	✓	0.00	-37±47	
	3	21	21:18:51.226	+00:35:01.96	19.56	0.2740±0.0002	1	✓	0.38	-424±103	
	3	66	21:18:51.814	+00:34:44.38	20.20	0.3058±0.0004	1	...	0.36	7022±169	
	3	75	21:18:49.304	+00:34:36.62	19.15	0.1346±0.0001	0	...	0.14	-33096±66	
	3	77	21:18:50.210	+00:34:37.07	20.14	0.2195±0.0003	1	...	0.22	-13192±127	
	3	118	21:18:49.121	+00:34:20.26	18.85	0.2610±0.0003	1	...	0.17	-3470±127	
	3	178	21:18:50.051	+00:33:55.37	19.01	0.3132±0.0004	1	...	0.11	8768±192	
	NW	1	25	21:18:46.617	+00:35:06.97	20.60	0.2727±0.0001	0	✓	0.41	-724±70
	NW	2	112	21:18:46.414	+00:34:26.28	20.33	0.2621±0.0001	0	...	0.26	-3217±70
	NW	2	209	21:18:44.289	+00:33:42.58	19.24	0.2688±0.0001	0	✓	0.30	-1645±61
	NW	3	161	21:18:42.244	+00:34:02.14	20.31	0.2735±0.0002	0	✓	0.44	-531±84
	NW	3	218	21:18:41.776	+00:33:36.44	19.08	0.1644±0.0001	0	...	0.31	-26114±66
	SE	1	55	21:18:53.543	+00:33:18.15	18.90	0.2717±0.0001	0	✓	0.29	-953±61
	SE	1	185	21:18:53.214	+00:32:21.39	20.36	0.2774±0.0002	1	✓	0.42	369±80
	SE	2	19	21:18:50.005	+00:33:26.22	19.07	0.2794±0.0002	0	✓	0.08	842±80
	SE	2	24	21:18:52.466	+00:33:27.23	19.30	0.2786±0.0001	0	✓	0.22	652±61
	SE	2	42	21:18:53.957	+00:33:21.27	19.97	0.2754±0.0001	0	✓	0.32	-105±61
	SE	2	155	21:18:52.670	+00:32:32.22	20.33	0.2132±0.0003	1	...	0.29	-14680±131
	SE	3	56	21:18:54.097	+00:33:12.36	19.86	0.2284±0.0000	0	...	0.29	-11096±9
	SW	1	100	21:18:47.781	+00:32:58.96	18.20	0.2276±0.0000	0	...	0.16	-11305±23
	SW	1	120	21:18:43.405	+00:32:45.55	19.22	0.2811±0.0002	0	✓	0.42	1236±89
	SW	1	152	21:18:45.023	+00:32:33.46	18.62	0.2770±0.0001	0	✓	0.37	291±42
	SW	1	167	21:18:45.081	+00:32:27.08	19.91	0.2786±0.0002	0	✓	0.39	669±80
	SW	2	38	21:18:45.564	+00:33:22.07	20.54	0.3010±0.0001	1	...	0.24	5907±28

Table A.6 Continued

tile (1)	dither (2)	fiber (3)	ra (4)	dec (5)	r (mag) (6)	redshift (7)	Q (8)	Member (9)	R (Mpc) (10)	LOSV (km s ⁻¹) (11)
SW	2	122	21:18:44.203	+00:32:45.66	20.29	0.2775±0.0001	0	✓	0.38	404±66
SW	2	206	21:18:42.699	+00:32:06.10	17.62	0.2700±0.0001	0	✓	0.55	-1356±33
SW	3	220	21:18:42.834	+00:31:57.86	21.05	0.2739±0.0000	0	✓	0.57	-440±19

Table A.7: Spectroscopic redshifts for galaxies in MSJ215422.9+003723.5 measured with the MS: Columns as in Table 3.2

tile (1)	dither (2)	fiber (3)	ra (4)	dec (5)	r (mag) (6)	redshift (7)	Q (8)	Member (9)	R (Mpc) (10)	LOSV (km s ⁻¹) (11)
NE	1	62	21:53:22.219	+00:12:39.81	20.97	0.0766±0.0001	1	...	0.10	-34369±34
NE	1	215	21:53:26.220	+00:11:40.21	16.71	0.2159±0.0001	0	✓	0.26	-146±44
NE	2	138	21:53:23.595	+00:12:08.78	20.12	0.2737±0.0002	0	...	0.21	14070±88
NE	2	220	21:53:21.347	+00:11:30.70	19.12	0.2192±0.0002	0	✓	0.00	667±79
NE	3	129	21:53:26.616	+00:12:12.42	19.97	0.2172±0.0002	0	✓	0.32	178±84
NE	3	154	21:53:24.770	+00:11:59.52	20.86	0.2809±0.0000	0	...	0.25	15838±25
NE	3	168	21:53:24.545	+00:11:53.74	21.00	0.2210±0.0001	0	✓	0.19	1119±44
NE	3	174	21:53:27.197	+00:11:53.68	19.85	0.2161±0.0001	0	✓	0.32	-92±69
NW	1	206	21:53:15.345	+00:11:39.78	19.96	0.2170±0.0001	0	✓	0.32	131±44
NW	2	55	21:53:19.205	+00:12:46.30	20.20	0.2134±0.0002	0	✓	0.29	-751±108
NW	3	151	21:53:16.776	+00:11:59.52	19.20	0.2166±0.0001	0	✓	0.26	45±39
NW	3	217	21:53:20.606	+00:11:34.95	20.71	0.2188±0.0002	1	✓	0.04	586±98
SE	1	12	21:53:26.058	+00:11:29.27	19.79	0.2164±0.0001	0	✓	0.25	-19±59
SE	1	40	21:53:25.627	+00:11:16.34	18.96	0.2164±0.0001	0	✓	0.23	-9±49
SE	3	43	21:53:27.012	+00:11:14.01	19.55	0.2159±0.0002	0	✓	0.30	-127±88
SE	3	57	21:53:26.805	+00:11:06.27	19.54	0.2143±0.0001	0	✓	0.30	-537±54
SE	3	61	21:53:21.720	+00:11:00.41	20.37	0.2144±0.0001	0	✓	0.11	-510±59
SW	1	51	21:53:17.384	+00:11:10.44	19.13	0.2189±0.0001	0	✓	0.22	608±34
SW	1	174	21:53:20.933	+00:10:22.05	19.86	0.3719±0.0001	0	...	0.36	38208±34
SW	2	133	21:53:14.825	+00:10:33.36	20.80	0.2085±0.0002	0	...	0.39	-1958±84
SW	3	41	21:53:19.548	+00:11:13.96	19.84	0.2138±0.0001	0	✓	0.11	-658±39

Table A.8: Spectroscopic redshifts for galaxies in XMMXCSJ124425.9+164758.0: Columns as in Table 3.2

tile	dither	fiber	ra	dec	r (mag)	redshift	Q	Member	R (Mpc)	LOSV (km s ⁻¹)	
(1)	(2)	(3)	(4)	(5)	(6)	(7)	(8)	(9)	(10)	(11)	
NE	1	39	12:44:29.179	+16:49:17.17	19.38	0.4514±0.0001	0	...	0.61	53398±44	
	1	79	12:44:27.588	+16:48:59.30	20.00	0.2235±0.0001	1	...	0.29	-1943±44	
	1	85	12:44:30.641	+16:48:58.51	19.65	0.2376±0.0001	0	...	0.40	1475±39	
	1	207	12:44:26.458	+16:48:01.70	20.04	0.2372±0.0002	1	...	0.09	1398±92	
	2	65	12:44:27.576	+16:49:04.52	20.86	0.2529±0.0001	1	...	0.33	5207±39	
	2	123	12:44:27.689	+16:48:39.78	18.94	0.1079±0.0001	1	...	0.12	-29994±63	
	3	205	12:44:25.438	+16:48:00.39	18.15	0.2313±0.0002	0	✓	0.05	-52±78	
	NW	1	17	12:44:23.999	+16:47:52.05	19.70	0.3377±0.0001	0	...	0.09	25789±58
	NW	1	70	12:44:28.565	+16:47:33.65	20.71	0.2372±0.0002	1	...	0.19	1402±97
	NW	2	6	12:44:25.438	+16:47:56.96	17.43	0.2340±0.0001	0	✓	0.04	606±34
	NW	3	50	12:44:25.866	+16:47:35.40	20.14	0.2324±0.0002	0	✓	0.06	222±83
	SE	1	164	12:44:27.304	+16:46:39.99	20.92	0.2302±0.0001	0	✓	0.27	-317±39
	SE	3	14	12:44:31.911	+16:47:47.15	19.72	0.4523±0.0001	0	...	0.56	53626±49
	SE	3	17	12:44:26.252	+16:47:41.10	20.39	0.2312±0.0000	0	✓	0.06	-71±15
	SE	3	105	12:44:26.799	+16:47:00.82	19.89	0.1361±0.0001	1	...	0.13	-23149±49
	SW	1	25	12:44:23.322	+16:47:43.10	21.16	0.2192±0.0002	1	...	0.10	-2975±92
	SW	1	29	12:44:25.243	+16:47:44.50	19.12	0.2316±0.0000	0	✓	0.01	23±24
	SW	2	28	12:44:24.524	+16:47:42.65	17.24	0.0253±0.0001	1	...	0.01	-50068±53
	SW	2	241	12:44:22.332	+16:46:07.60	18.90	0.2372±0.0001	0	...	0.41	1381±29

Table A.9: Spectroscopic redshifts for galaxies in XMMXCSJ125650+254803.2: Columns as in Table 3.2

tile (1)	dither (2)	fiber (3)	ra (4)	dec (5)	r (mag) (6)	redshift (7)	Q (8)	Member (9)	R (Mpc) (10)	LOSV (km s ⁻¹) (11)	
NE	1	223	12:56:53.588	+25:48:02.73	19.64	0.3931±0.0001	1	...	0.26	25900±70	
	3	6	12:56:53.977	+25:49:31.89	18.33	0.1720±0.0001	0	...	0.30	-25656±33	
	3	47	12:56:52.732	+25:49:10.94	18.32	0.1728±0.0001	0	...	0.23	-25472±61	
	NW	1	158	12:56:50.241	+25:48:32.88	19.07	0.2819±0.0001	0	✓	0.13	-34±56
	NW	1	170	12:56:49.017	+25:48:27.68	21.28	0.1665±0.0002	1	...	0.08	-26948±93
	NW	3	201	12:56:50.112	+25:48:10.26	17.68	0.2810±0.0001	0	✓	0.03	-237±47
	SE	1	227	12:56:55.806	+25:46:22.69	19.95	0.3972±0.0001	1	...	0.68	26859±47
	SW	1	122	12:56:46.504	+25:47:04.28	19.49	0.3287±0.0001	0	...	0.36	10880±51
	SW	2	58	12:56:50.691	+25:47:36.32	19.90	0.2580±0.0001	0	...	0.11	-5604±70
	SW	3	132	12:56:44.117	+25:46:56.15	18.06	0.2833±0.0001	0	✓	0.45	304±47
	SW	3	138	12:56:47.249	+25:46:54.73	21.12	0.3280±0.0001	0	...	0.37	10722±28